HOKKAIDO UNIVERSITY

Title	Study on Stimuli-Responsive Quinodimethane Derivatives with Controllable Photophysical Properties
Author(s)	菅原, 一真; SUGAWARA, Kazuma
Degree Grantor	北海道大学
Degree Name	博士(理学)
Dissertation Number	甲第15194号
Issue Date	2022-09-26
DOI	https://doi.org/10.14943/doctoral.k15194
Doc URL	https://hdl.handle.net/2115/90507
Type	doctoral thesis
File Information	SUGAWARA_Kazuma.pdf

Hokkaido University Collection of Scholarly and Academic Papers : HUSCAP

Doctoral Dissertation

Study on Stimuli-Responsive Quinodimethane Derivatives with Controllable Photophysical Properties

（光物理的特性の制御が可能な
刺激応答性キノジメタン誘導体に関する研究)

Kazuma SUGAWARA

Laboratory of Organic Chemistry I

Graduate School of Chemical Sciences and Engineering

Hokkaido University

2022

Table of Contents

Chapter 0

General Introduction

0-1. Stimuli-Responsive Molecules

Conversions from a chemical species to another generally occur at the chemical reactions in a flask, and those involved with the formation of a molecular skeleton or the introduction of substituents are usually irreversible processes. In contrast, there are some compounds that can be reversibly converted to another state by physical and/or chemical stimuli such as light, heat, stress, vapor and/or pH, which are called stimuli-responsive molecules. As shown in Figure 0-1, when they undergo a macroscopic external stimulation, their microscopic properties can be drastically changed via various reactions and structural changes such as isomerization, bond formation/scission, protonation/deprotonation, redox reaction, and conformational change.[1–5] Thus, they have been widely studied for applications in molecular switches, memory devices, and sensor materials.[6–11]

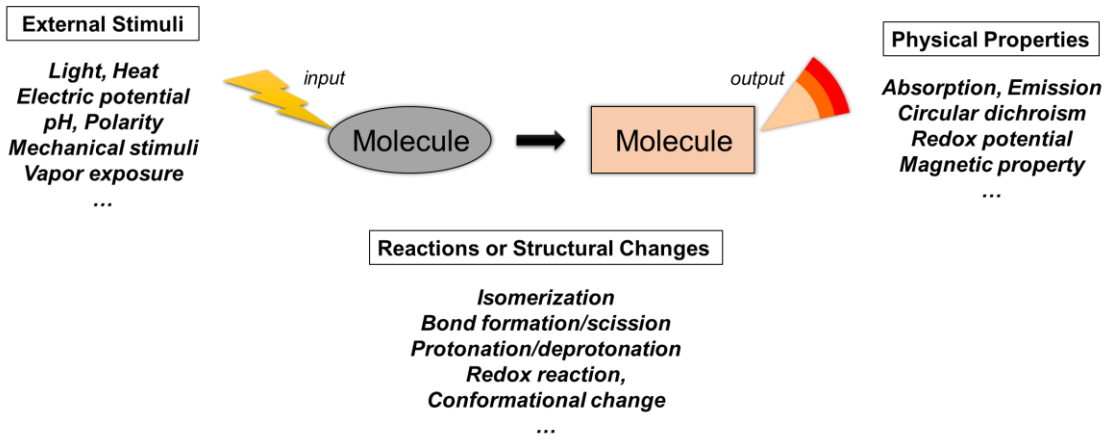

Figure 0-1. Schematic illustration of stimuli-responsive molecules

0-2. Chromic Systems

Chromic materials are one of the typical examples of utilizing stimuli-responsive molecules. Chromism is a phenomenon in which a color of compound changes reversibly by an external stimulus, and chromic-responsive molecules are expected to be applied for molecular devices.[8,9] For azobenzene, which is one of the most famous photochromic systems, a thermodynamically stable *trans*-form (colorless) undergoes *trans-cis* isomerization upon irradiation with light and is converted to a metastable *cis*-form (orange) (Figure 0-2a).[1] In contrast to azobenzene, which is a thermally reversible (T-type) photochromic system, diarylethene is classified as P-type due to its thermal irreversibility (Figure 0-2b). Indeed, for diarylethene, the switching between open- and closed-ring isomers depends solely on light in both processes, and thus, the switching can be performed more easily. Furthermore, extending the π-electron system of the thiophene ring is useful way to achieve a variety of color tones in a closed ring isomer.[3]

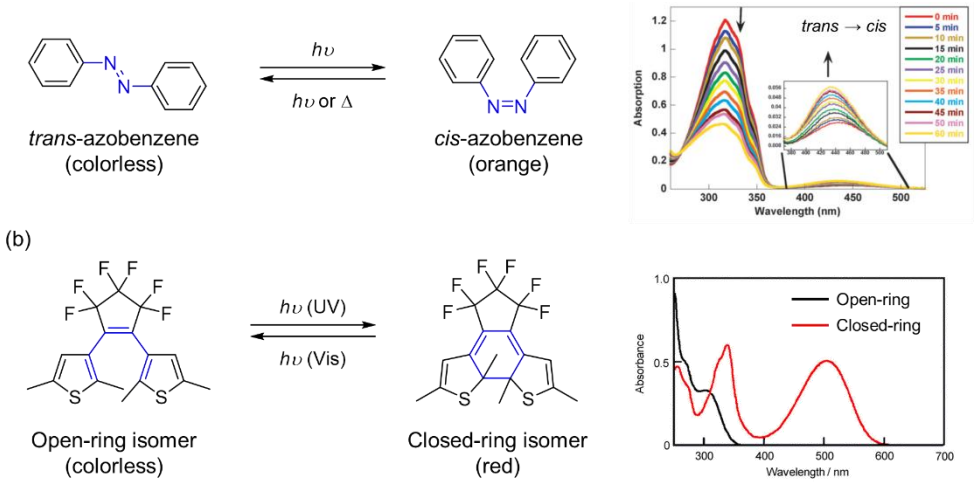

Figure 0-2. Representative examples of chromic molecules [(a) azobenzene and (b) diarylethene].

While various chromic response systems have been reported depending on a type of the external stimuli in addition to light, the author's group has focused on electrochromism in which a change in color is induced by applying an electric potential as an input. Particularly, dynamic redox (*dyrex*) systems, which show a large change in structure accompanied by C-C bond cleavage and formation upon electron transfer, are well studied for their characteristic features, i.e., they exhibit one-wave two-electron redox waves with a large separation between the oxidation and reduction peaks due to the structural change upon redox reactions. By incorporating a dye skeleton that exhibits vivid color in the charged state into such *dyrex* molecules, the author's group has reported plenty of electrochromic molecules with *dyrex* behavior.[12–15] For instance, a clean chromic response with a drastic color change upon electrochemical oxidation and reduction was demonstrated by *o*-quinodimethane-type compound with 4-methoxyphenyl groups (Figure 0-3).[16,17]

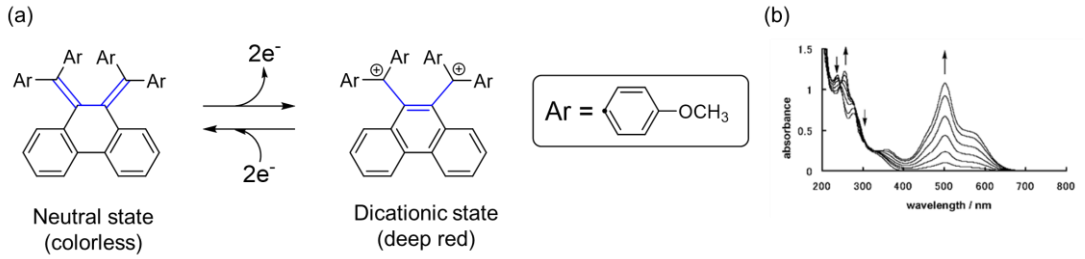

Figure 0-3. (a) Dynamic structural change upon electron transfer. (b) Change in UV/Vis spectrum of *o*-quinodimethane-type compound upon electrochemical oxidation in CH_3CN.

Electrochromic response systems have been investigated for their potential application as display materials and smart windows (Figure 0-4).[18] These materials have attracted much attention, however, their uses are mostly limited to non-crystalline materials, because the electron-conducting properties are necessary to exhibit electrochromic behavior in devices.

Figure 0-4. Switching sequence of a laminated electrochromic glass manufactured by Gesimat GmbH, Berlin, Germany. This electrochromic device uses tungsten oxide and Prussian blue as complementary electrochromic layers and ion-conducting poly(vinylbutyral) as the polymer electrolyte.

On the other hand, there is an increasing interest in mechanochromic response systems that exhibit a color change and/or a luminescent color change in a crystalline state when mechanical forces (e.g., grinding or external stress) are applied to crystalline or polymeric materials.[19] For molecules with mechanochromic properties, the original color or luminescent color can be recovered by treatment with dissolving, heating, and sonicating, etc. Such mechanochromic response is often triggered by a change in conformation (Figure 0-5)[20] and in crystal packing of the molecule,[21] and by a crystal-to-amorphous phase transition (Figure 0-6).[22] In particular, when it originates from a change in molecular conformation, there is an intriguing possibility that a change in luminescent color may simultaneously be manifested in addition to a change in color by mechanical stimuli.

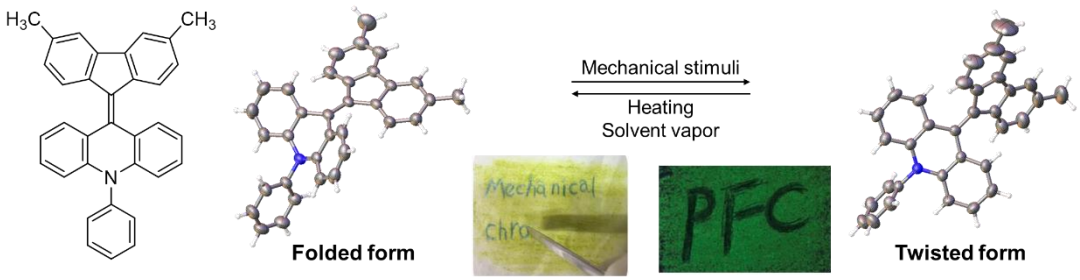

Figure 0-5. Mechanochromic behavior of fluorenyridene acridane type molecule triggered by a change in conformation of the molecule.

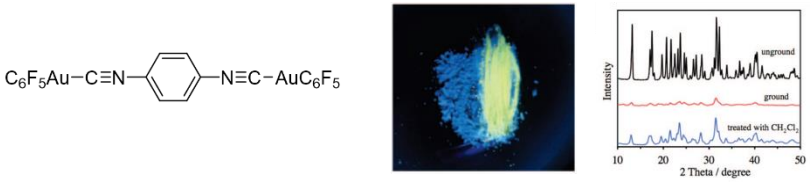

Figure 0-6. Mechanofluorochromism of the gold isocyanide complex induced by crystal-to-amorphous phase transition.

Additionally, some mechanochromic molecules also have aggregation-induced emission (AIE) properties.[23] While ordinary organic molecules exhibit concentration quenching of the luminescence, the molecules with AIE properties do not emit in diluted solution, but strongly emit in a solid or aggregated state, as represented by tetraarylethylenes (Figure 0-7).[24,25]

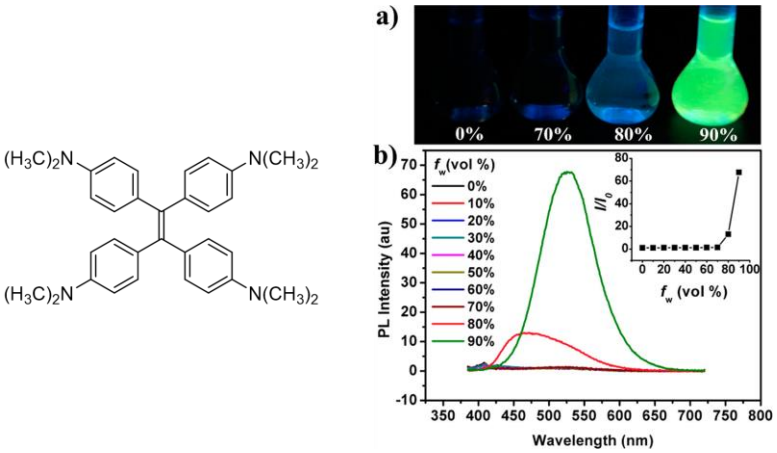

Figure 0-7. (a) Fluorescent images of tetrakis[4-(dimethylamino)phenyl]ethylene (TDMAPE) in different water fraction mixtures under 365-nm UV irradiation. (b) Fluorescence spectra of TDMAPE (1×10^{-5} M) in THF and water mixtures with different water fractions (f_w). Inset: plot of I/I_0 versus water fraction, where I and I_0 represent the fluorescence intensities in a THF/water mixture with a specific f_w and in pure THF, respectively.

As described above, a variety of molecules have been reported to change their color tone or luminescent color due to a change in molecular geometry or environment in response to certain stimuli. However, these stimuli-responsive molecules are often evaluated in either solution phase or solid phase. Thus, there is still room to develop the molecule that exhibits diverse chromic behavior in different phases in response to respective external stimuli.

0-3. Overcrowded Ethylenes

With regard to the response systems related to a change in the molecular geometry, overcrowded ethylenes (OCEs), in which the C=C double bond is surrounded by bulky substituents, have been widely investigated for conformational aspects (Figure 0-8). For example, the conformations of OCEs can be switched between two or more conformers by external stimuli,[14,26–28] especially for use in molecular motors.[5,29–32]

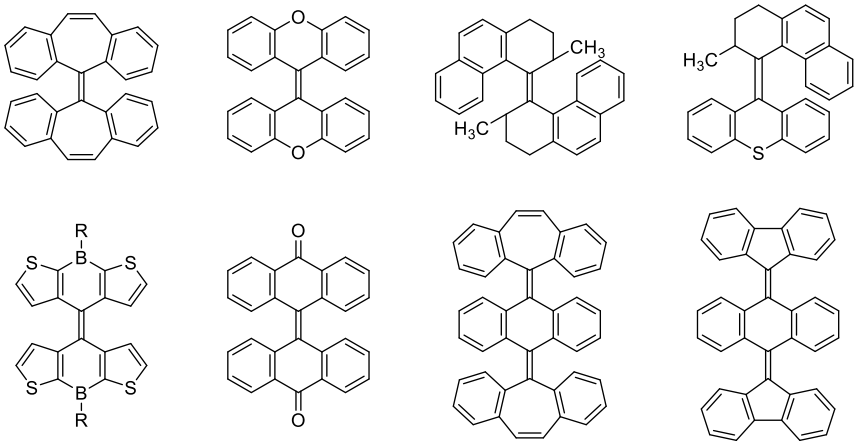

Figure 0-8. Examples of OCEs.

While normal alkenes have a planar geometry, sterically hindered alkenes such as OCEs can adopt a nonplanar structure, such as folded (**F**) and twisted (**T**) forms (Figure 0-9). Generally, the **T**-form has a narrower HOMO-LUMO gap (in other words, a higher HOMO and lower LUMO) than the **F**-form, resulting in a significant difference in absorption and emission wavelength between conformers (Figure 0-10). However, despite the attractive properties applicable to molecular switches, investigations on the **T**-form remain insufficient due to its potential instability or shorter lifetime.

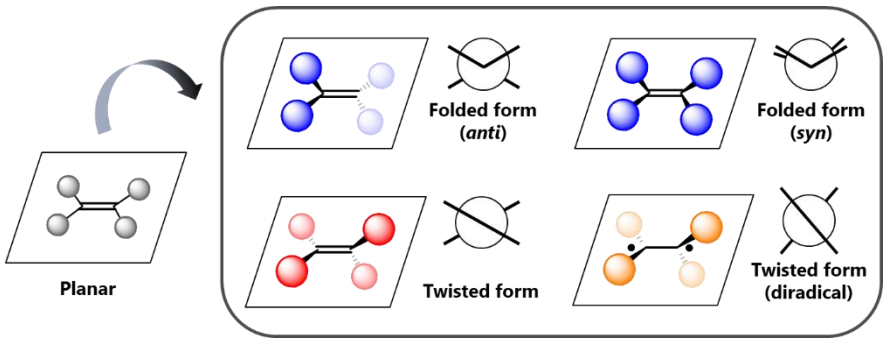

Figure 0-9. Schematic illustration of various conformations that OCEs can adopt.

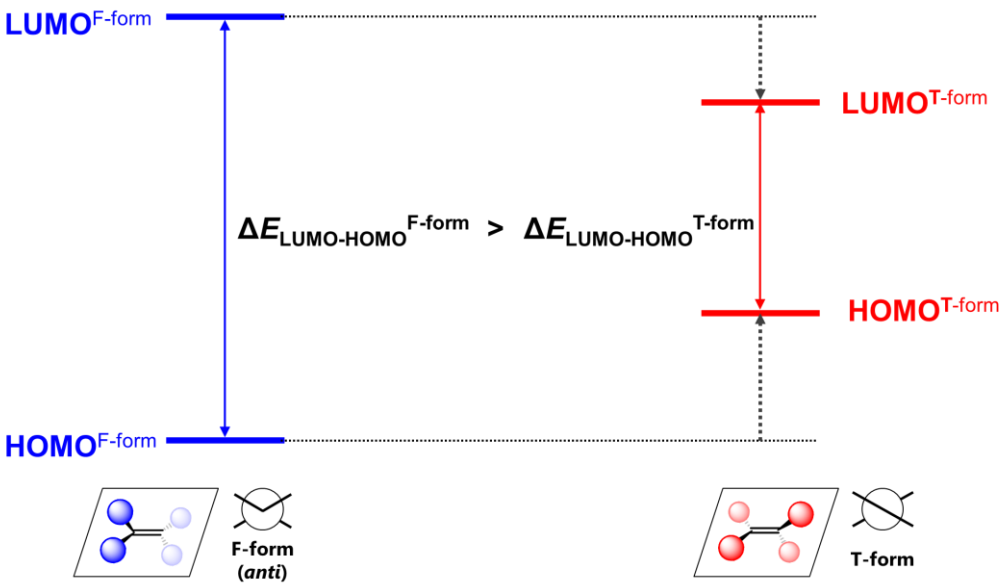

Figure 0-10. Estimated energy profiles of HOMO and LUMO levels for **F**-form and **T**-form.

0-4. Bistricyclic Aromatic Enes

Among OCEs, bistricyclic aromatic enes (BAEs) have thus far been used as a common way to obtain the **T**-form in addition to the **F**-form. Such BAEs have been broadly investigated for their potential application as stimuli-responsive molecules.[33–40] Since it is difficult to isolate more than two structures for the same molecule, there are very few examples, e.g., fluorenylidene xanthene derivative (Figure 0-11a), fluorenylidene acridan derivative (Figure 0-5), and biphenoquinodimethane derivative (Figure 0-11b), where the existence of both **F**- and **T**-forms was confirmed by X-ray analyses even for BAEs.[41–43] As exemplified by these molecules, dramatic chromic behavior based on the difference in the electronic configuration between **F**- and **T**-forms is expected.

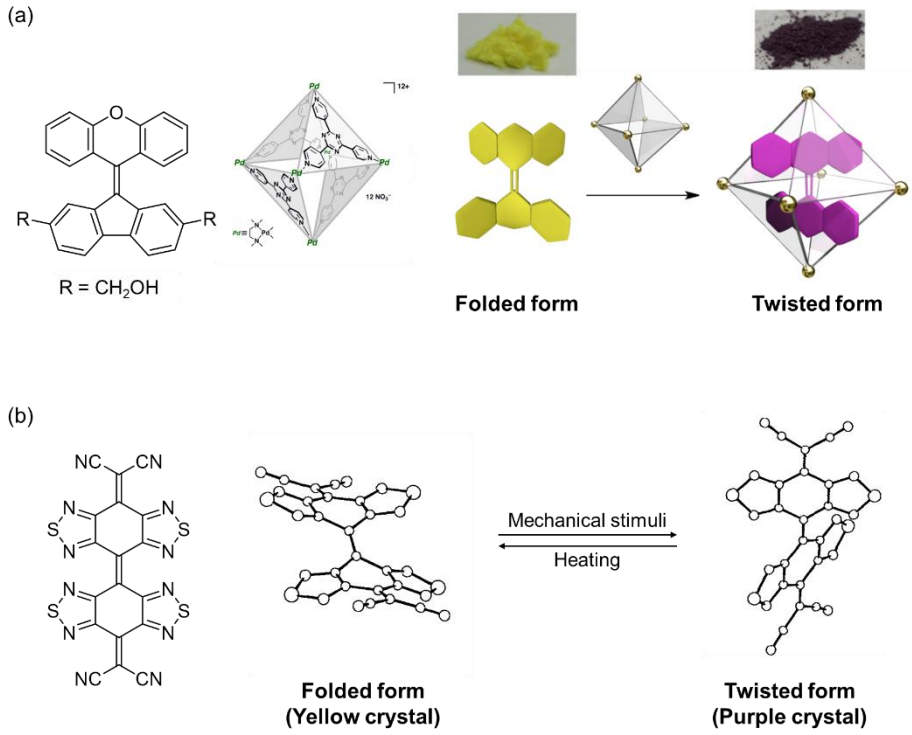

Figure 0-11. Examples of BAEs in which both **F**- and **T**-form can be confirmed by X-ray analyses.

As exemplified by these molecules, distinct chromic behavior based on the difference in the electronic configuration between **F**- and **T**-forms is expected, however, the molecular design strategy is limited to BAEs with rigid and planar tricyclic aromatic groups among OCEs. In addition, such stimuli-responsive behavior is also limited to that derived from the conformational change between two states in almost all systems.

0-5. Contents of This Dissertation

Based on such background, the author reports the study on stimuli-responsive quinodimethane derivatives with controllable photophysical properties in this dissertation.

In chapter 1, the author realized to create two-way chromic systems based on tetraarylanthraquinodimethanes (Ar_4AQDs, Figure 0-12). Considering that most chromic systems are limited to a solution- or solid-phase response, the development of molecules that exhibit different chromism in different phases is of great significance. Therefore, the author focused on Ar_4AQDs **1** which has both a redox-active unit and AIE-active tetraarylethylene structure. As a result, AQD derivatives **1** with a butterfly-shaped **F**-form and the corresponding dications $\mathbf{1}^{2+}$ with a twisted structure can undergo interconversion upon two-electron transfer, which is accompanied by a drastic color change. While reversible electrochromic behavior occurs in solution, electron donors **1** exhibit fluorescence only in a solid state. The emission color changed upon grinding as-synthesized samples of **1**, and the original emission color was recovered by a dissolving-drying process.

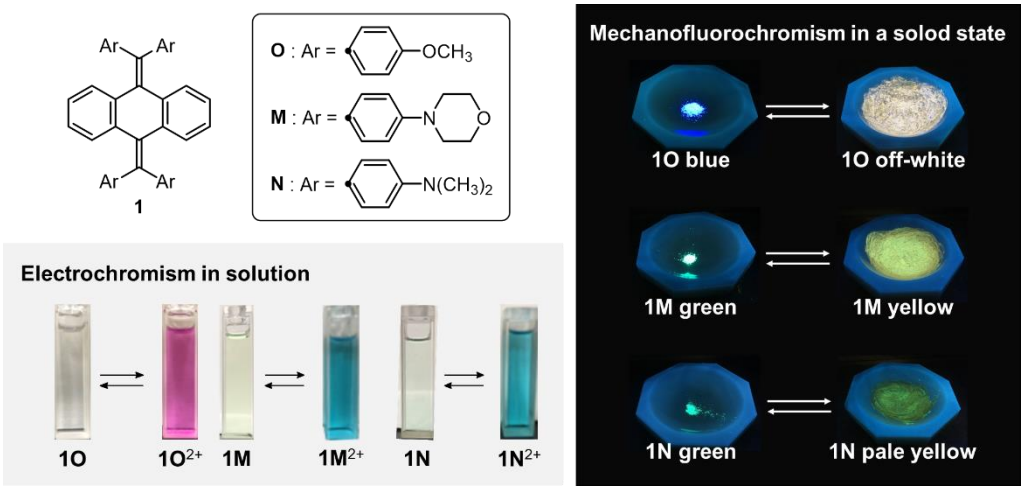

Figure 0-12. Two-way chromic systems based on Ar_4AQDs **1**.

In chapter 2, the author succeeded in the modulation of photophysical properties (color tone and emission color) based on multiple conformations in the crystal (Figure 0-13). Although some dramatic chromic systems due to switching between different structures such as **F**- and **T**-forms have been reported in OCEs, the approach to construct such response systems has been limited to using BAE-type molecules. Furthermore, only two structures are involved in the switching behavior in almost all systems. To develop a response system involving more than two structures for novel molecules other than BAEs, the author newly designed flexible polyaryl-substituted tetraazaanthraquinodimethanes (N_4AQDs) **2**, in which a steric hindrance in the overcrowded fjord region was moderately reduced. As a result, X-ray analyses revealed that N_4AQDs can adopt not only **F**- and **T**- forms but also

intermediate structures, e.g., planar (**P**) and twisted-folded forms (**TF**), in pseudopolymorphs. Since there is a large difference in electronic configuration among conformers, the color tone of crystals varied from yellow to red depending on the conformation of overcrowded N_4AQDs. Notably, red to near-infrared emission was observed for twisted conformers.

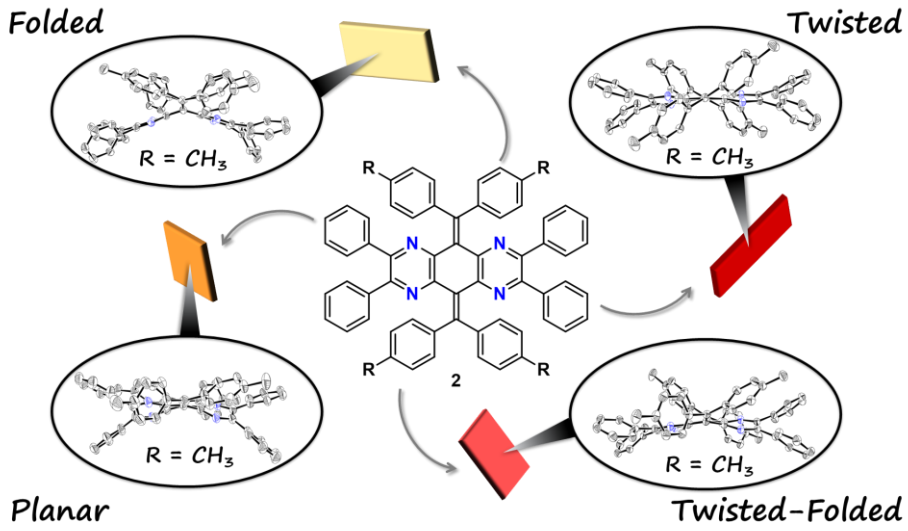

Figure 0-13. Modulation of photophysical properties based on multiple conformations of N_4AQDs **2**.

Based on the findings of Chapters 1 and 2, the author explored new possibilities of N_4AQD derivatives. In chapter 3, the author demonstrates that the N_4AQD derivatives have potential applications in the study of nitrogen-doped nanographenes on noble surfaces. The author envisaged that N_4AQDs can be applied to on-surface chemistry on metal substrates, which has been actively studied and where a variety of reactions that cannot occur in a flask can proceed. With bond-resolved scanning tunneling microscopy, a novel reaction by which two nitrogen atoms in one aromatic ring are divided into two azaaromatic units ("heterocyclic segregation") was discovered on a metal surface. Furthermore, in the course of this investigation, the author succeeded in developing an efficient and versatile synthetic method of tetraazaanthraquinones, which are precursors of tetraazaanthraquinodimethane derivatives with arbitrary substituents on the central skeleton (Scheme 0-1).

Scheme 0-1. Synthetic method of tetraazaanthraquinone derivatives, which allows substituents to be introduced on the central quinodimethane skeleton.

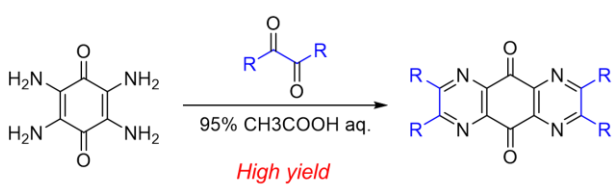

Chapter 1

Development of Multiple Response Systems: Electrochromism in Solution and Mechanofluorochromism in a Solid State

1-1. Introduction

The aim of more advanced chromic materials requires the development of molecules that exhibit diverse responses to multiple stimuli. Furthermore, if these responses take place in different phases (e.g., in solution and in a solid state), it will be a stepping stone toward the further development of smart materials. In this study, the author considered to develop molecules that also exhibit mechanochromic behavior in the solid state, in addition to electrochromic behavior in solution, which has been actively studied in the author's group.

However, molecules with these two chromic properties have some problems to be solved for their application. For electrochromic materials, it is difficult to control an operating potential with maintaining the color of the molecule. For mechanochromic materials, molecular design guidelines are still unclear. Therefore, the author considered that it is necessary to investigate molecules with chromic properties systematically by screening approach. Moreover, there is no example exhibiting different chromism in different phases for the same molecule, and thus, this is a challenging subject toward further development of smart materials.

To solve this issue, the author focused on *dyrex* systems,[44,45] in which a unique feature is that there is a large difference between oxidation potential of electron donors and reduction potential of corresponding oxidized species due to a large structural change upon electron transfer. While *o*-quinodimethane-type compounds have reported as mentioned in chapter 0, 11,11,12,12-tetraaryl-9,10-anthraquinodimethane (Ar_4AQD) was also reported as one of the *p*-quinodimethane-type *dyrex* systems, and **1O** with four 4-methoxy groups exhibits electrochromism in solution.[46] The electron donor **1O** with a butterfly-shaped folded structure undergoes two-electron oxidation to produce a twisted dication $\mathbf{1O}^{2+}$ accompanied by a drastic color change from colorless to deep red (Scheme 1-1 and Figure 1-1).

Scheme 1-1. Electrochromic behavior of **1O**.

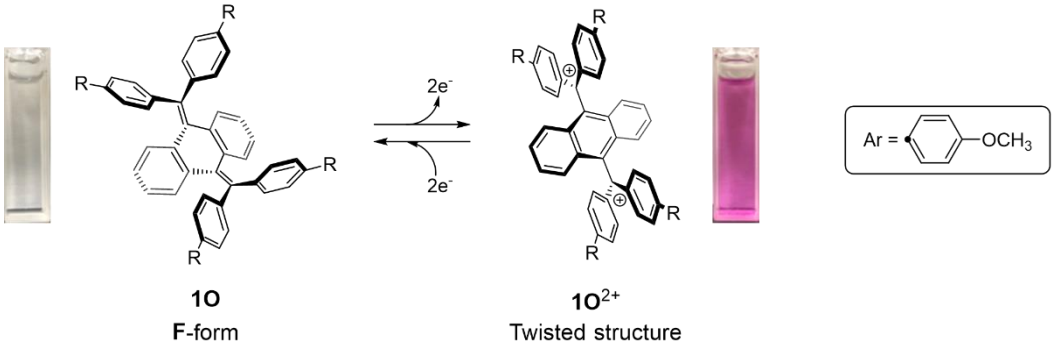

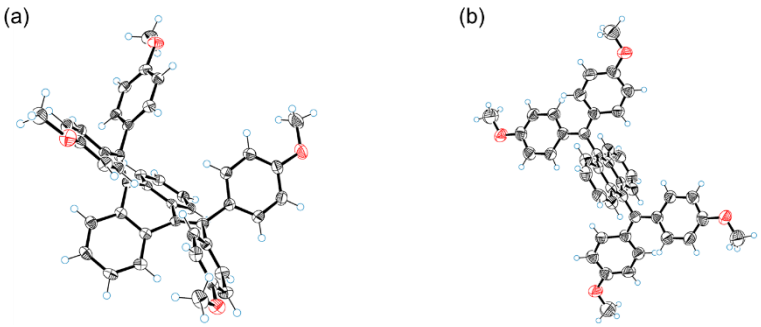

Figure 1-1. ORTEP drawings of (a) **1O** and (b) $\mathbf{1O}^{2+}(PF_6^-)_2$ at 150 K. Solvent molecules and counterions are omitted for clarity.

In this chapter, the author designed and synthesized novel Ar_4AQDs **1M** and **1N** (Figure 1-2), in which 4-morpholino- and 4-dimethylamino-phenyl groups on the aryl groups were chosen for their higher electron-donating ability, with the expectation that the difference between electronic characters could modulate their response behaviors. Notably, the author found that **1O**, **1M**, and **1N** are fluorescent in a solid state, but not in solution. Such behavior can be explained by considering the free rotation of aryl groups in solution, as in the case of tetraarylethylenes with AIE properties.[24] Since it was revealed that the emission color changed upon grinding of Ar_4AQDs **1**, the author reports here the redox behaviors of **1M** and **1N** as demonstrated by electrochemical analyses in solution and the mechanochromic behaviors of **1O**, **1M**, and **1N** as characterized by powder X-ray diffraction (PXRD) and emission and Raman spectroscopies in the solid state.

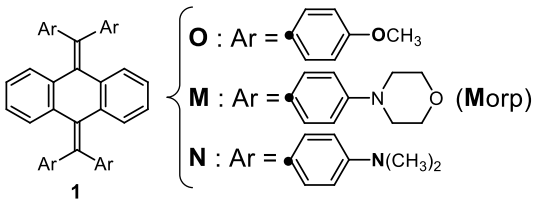

Figure 1-2. Tetraarylanthraquinodimethane derivatives **1O**, **1M**, and **1N**.

1-2. Results and Discussion

1-2-1. Preparation

Newly designed electron donors **1M** and **1N** were prepared on the basis of previously reported synthetic procedures.[46] Firstly, 11,11,12,12-tetrabromo-9,10-anthraquinodimethane **4**[47] was synthesized from 9,10-anthraquinone by the double dibromoolefination with CBr_4/PPh_3 in CH_2Cl_2. Subsequently, the Suzuki-Miyaura cross-coupling reaction of **4** with the corresponding aryl boronic acids[48,49] gave morpholino derivative **1M** and dimethylamino derivative **1N** in 89% and 85% yields, respectively, both as greenish yellow solids (Scheme 1-2).

Scheme 1-2. Preparation of **1M** and **1N**.

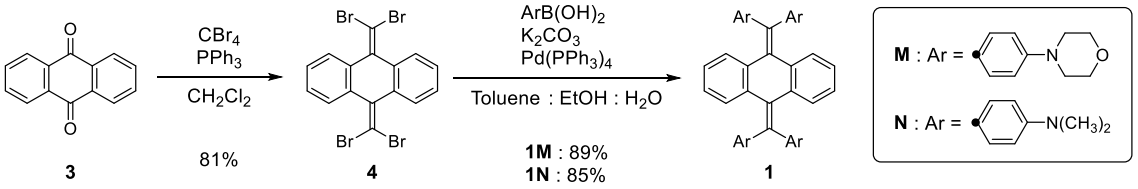

Upon oxidation of **1M** and **1N** with 2 equivalents of oxidant, deeply blue-colored dications $\mathbf{1M}^{2+}$ and $\mathbf{1N}^{2+}$ were obtained in 97% and 96% yields, respectively (Scheme 1-3). Since **1M** and **1N** were regenerated in 100% and 98% yields by treatment with activated Zn powder, their interconversions between electron donors and dications proceeded quantitatively (Scheme 1-3).

Scheme 1-3. Quantitative interconversion of $\mathbf{1M}/\mathbf{1M}^{2+}$ and $\mathbf{1N}/\mathbf{1N}^{2+}$.

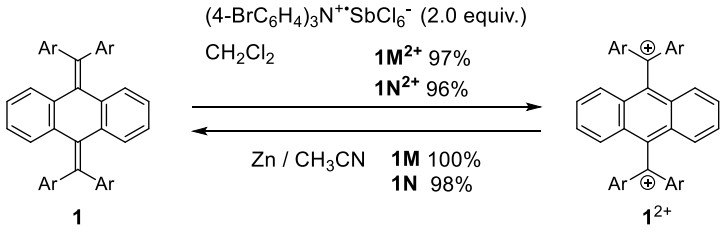

1-2-2. X-ray Analyses

According to X-ray analyses of single crystals recrystallized by vapor diffusion, both **1M** and **1N** adopt butterfly-shaped folded structures as in the case of **1O** (Figure 1-3). The bent angles θ between the central plane and diarylethenyl group are 39.1(1), 40.2(2)° for **1O**, 35.7(2), 36.5(2)° for **1M**, and 44.6(2)° for **1N**, respectively (Table 1-1). Density functional theory (DFT) calculations, which were conducted using the B3LYP/6-31G* level, showed similar values [41.5° for **1O**, 41.3° for **1M**, and 41.0° for **1N**] to those observed (Table 1-1).

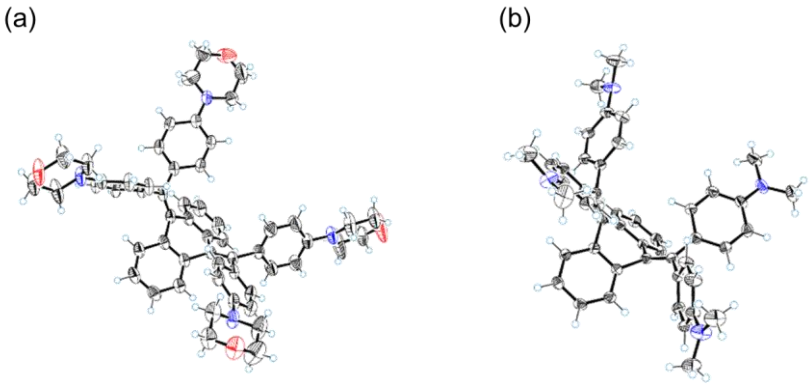

Figure 1-3. ORTEP drawings of (a) **1M** in $0.5(C_6H_{14})\cdot CH_2Cl_2$ solvate and (b) **1N** at 150 K. Solvent molecules are omitted for clarity.

For dications, they have almost orthogonally twisted conformations (Figure 1-4), while **1M** and **1N** adopt butterfly-shaped structures. Their average torsion angles α are 72.4° for $\mathbf{1M}^{2+}$ and 72.9° for $\mathbf{1N}^{2+}$, respectively, which are similar to that for $\mathbf{1O}^{2+}$ (71.4°) as shown in Table 1-1. These results are also supported by DFT calculations at the B3LYP/6-31G* level [71.4° for $\mathbf{1O}^{2+}$, 72.4° for $\mathbf{1M}^{2+}$, and 73.7° for $\mathbf{1N}^{2+}$, respectively] (Table 1-1).

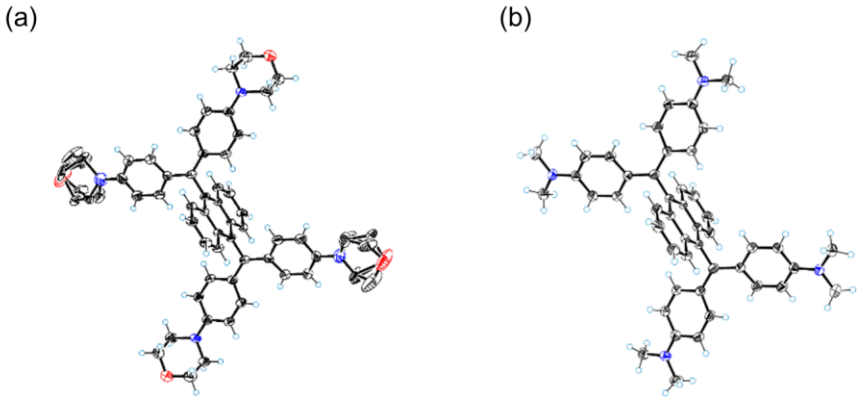

Figure 1-4. ORTEP drawings of (a) $\mathbf{1M}^{2+}(SbCl_6^-)_2$ in $2(CH_3NO_2)$ solvate and (b) $\mathbf{1N}^{2+}(SbCl_6^-)_2$ in 3(1,4-dioxane) solvate at 150 K. Solvent molecules and counterions are omitted for clarity.

Table 1-1. Structural parameters of **1O**, **1M**, and **1N** obtained from X-ray structures and from optimized structures calculated by the DFT method (B3LYP/6-31G*).

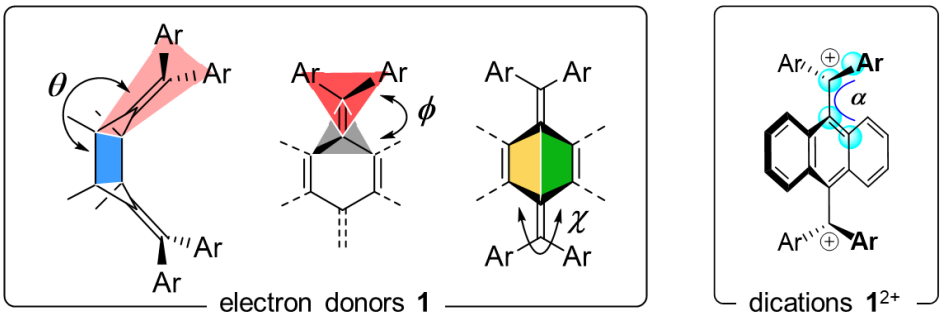

		θ [°]	ϕ [°]	χ [°]	α [°]
1O	Expt.	38.98(7)	7.28(5)	46.98(8)	–
		40.23(11)	9.55(6)		
	Calcd.	*41.5*	*9.26*	*44.48*	–
1M	Expt.	35.7(2)	10.68(15)	42.5(3)	–
		36.5(2)	6.42(2)		
	Calcd.	*41.3*	*10.45*	*44.11*	–
			9.90		
1N	Expt.	44.6(2)	14.66(8)	48.73(13)	–
		44.6(2)	13.98(9)		
	Calcd.	*41.0*	*10.55*	*44.13*	–
			10.36		
1O^{2+}	Expt.	–	–	–	71.4
	Calcd.	–	–	–	*71.4*
1M^{2+}	Expt.	–	–	–	72.4
	Calcd.	–	–	–	*72.4*
1N^{2+}	Expt.	–	–	–	72.9
	Calcd.	–	–	–	*73.7*

1-2-3. Redox Behavior

Cyclic voltammograms of **1M** and **1N** in CH_2Cl_2 showed two-electron oxidation peaks at +0.71 V vs. SCE and +0.50 V, respectively, for which a two-electron process was confirmed by using ferrocene as an external standard. As a result of changes in their structures, return peaks, at which twisted dications undergo two-electron reduction to give folded neutral species, appeared in the far cathodic region (-0.11 V for $\mathbf{1M}^{2+}$ and -0.27 V for $\mathbf{1N}^{2+}$). Such peak separation is a characteristic feature of *dyrex* systems, in which the steady-state concentration of an intermediate radical species is negligible.[50] Furthermore, the structural change is so fast that the author could not observe any change in the voltammograms at different scan rates. These details are summarized in Figure 1-5 and Table 1-2.

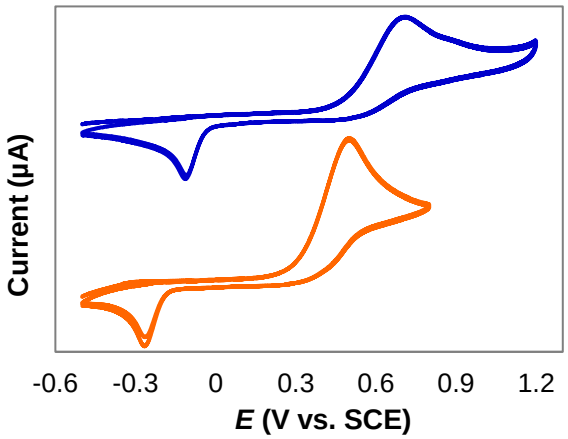

Figure 1-5. Cyclic voltammograms of (a) **1M** (blue, 1.0 mM) and (b) **1N** (orange, 1.0 mM) in CH_2Cl_2 containing 0.1 M Bu_4NBF_4 as a supporting electrolyte (scan rate 100 mV・s^{-1}, Pt electrode).

Table 1-2. Peak potentials are shown as E^{ox} and E^{red}.

		E^{ox} [V]		E^{red} [V]
cf.	**1O**	+1.00	$\mathbf{1O}^{2+}$	+0.42
	1M	+0.71	$\mathbf{1M}^{2+}$	-0.11
	1N	+0.50	$\mathbf{1N}^{2+}$	-0.27

Compared to the oxidation potential (E^{ox}) of **1O**, much less positive E^{ox}, indicating higher HOMO levels, were observed for **1M** and **1N** due to the stronger electron-donating ability of amino groups, and thus the reduction potentials of the corresponding dications also shifted to the cathode. Among them, **1N** with the highest HOMO level, as predicted by a study of substituted benzenes,[51,52] is most susceptible to oxidation. This means that the oxidation potential can be adjusted by changing the substituent on the aryl group, which provides the applicability to a donor-acceptor study.

1-2-4. Photophysical Properties and Theoretical Study

In the series of Ar_4AQDs, there are some notable features about photophysical and redox properties. For example, the color of the dications $\mathbf{1}^{2+}$ can be modified by replacing the substituent on the aryl group. The amino derivatives exhibit strong absorption at longer wavelength regions (λ_{max} = 634 nm and log ε = 5.21 for $\mathbf{1M}^{2+}$, λ_{max} = 628 nm and log ε = 5.27 for $\mathbf{1N}^{2+}$, respectively) than the methoxy derivative $\mathbf{1O}^{2+}$ as shown in Figure 1-6.

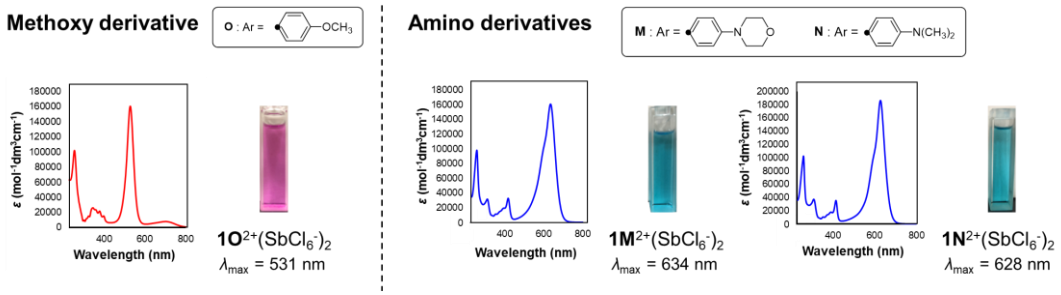

Figure 1-6. UV/Vis spectra of dications $\mathbf{1O}^{2+}(SbCl_6^-)_2$, $\mathbf{1M}^{2+}(SbCl_6^-)_2$, and $\mathbf{1N}^{2+}(SbCl_6^-)_2$ in CH_2Cl_2.

In addition, UV/Vis spectra of **1M**/**1N** and $\mathbf{1M}^{2+}$/$\mathbf{1N}^{2+}$ were quite similar to each other, probably due to a nearly identical band gap. Actually, similar band gaps of **1M**/**1N** and $\mathbf{1M}^{2+}$/$\mathbf{1N}^{2+}$ were estimated by DFT calculations (3.70 eV for **1M**, 3.60 eV for **1N**, 2.28 eV for $\mathbf{1M}^{2+}$, and 2.33 eV for $\mathbf{1N}^{2+}$, respectively) as shown in Table 1-3 and Figures 1-7 and 1-8. According to theoretical study, **1N** with the highest HOMO level (-5.03 eV for **1O**, -4.81 eV for **1M** and -4.42 eV for **1N**, respectively) is most susceptible to oxidation as demonstrated by voltammetric analyses. Furthermore, there is a difference of ca. 0.2 eV in their oxidation potentials between **1M** and **1N** despite the nearly the same absorptions were observed. This means that operating potential can be switched with maintaining the blue color. Thus, the redox behavior of Ar_4AQDs can be fine-tuned by varying the substituents on the aryl groups.

Table 1-3. The calculated energy levels and HOMO-LUMO gaps for the electron donors **1** and the corresponding dications $\mathbf{1}^{2+}$.

	HOMO [eV]	HOMO-1 [eV]	HOMO-2 [eV]	LUMO [eV]	HOMO-LUMO gap [eV]
1O	-5.03	-5.35	-5.80	-1.12	3.91
1M	-4.81	-5.03	-5.19	-1.11	3.70
1N	-4.42	-4.66	-4.95	-0.82	3.60
$\mathbf{1O}^{2+}$	-10.16	-10.81	-10.84	-8.11	2.05
$\mathbf{1M}^{2+}$	-9.50	-9.55	-9.56	-7.22	2.28
$\mathbf{1N}^{2+}$	-9.53	-9.57	-9.59	-7.20	2.33

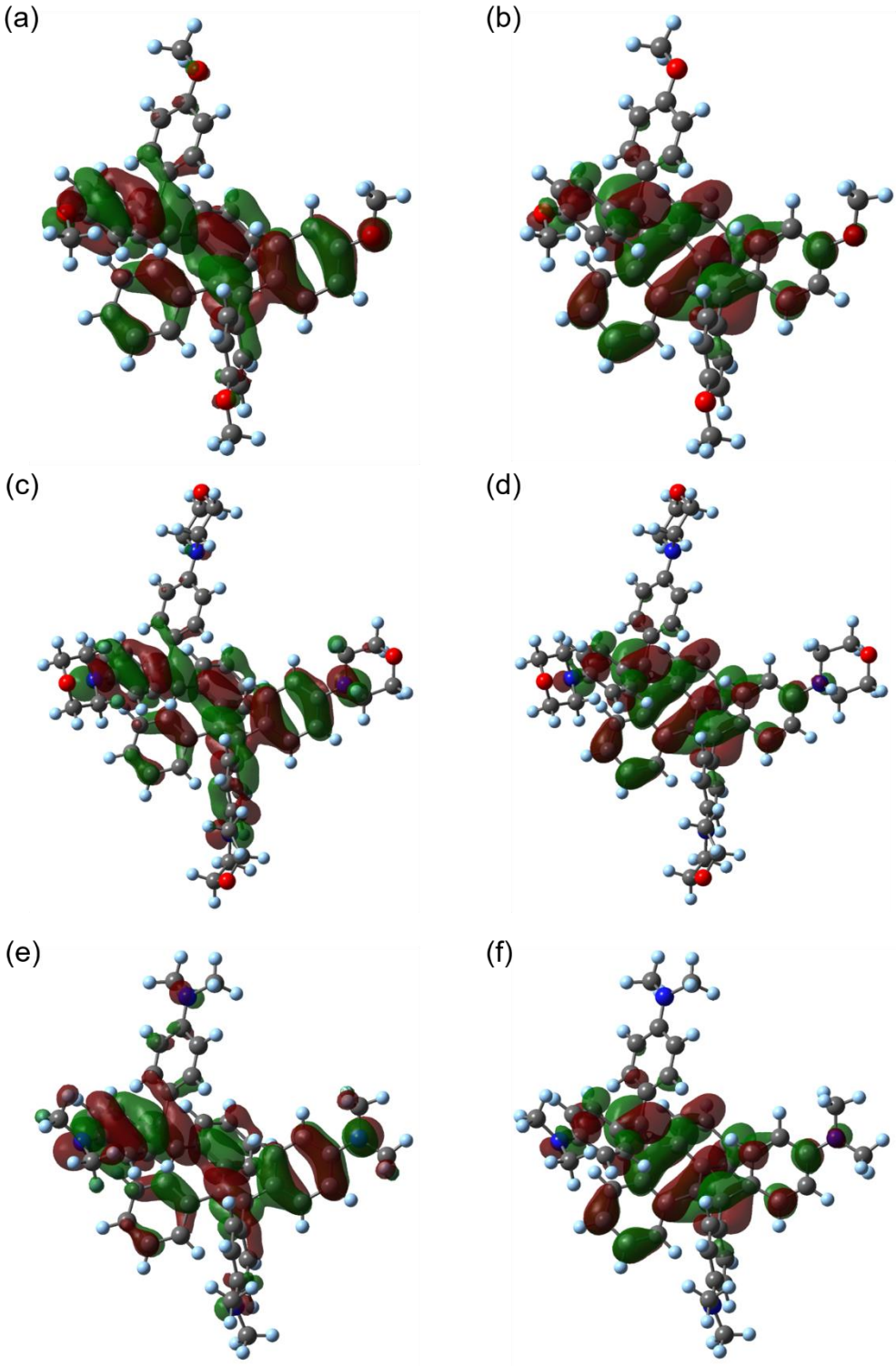

Figure 1-7. Optimized structures: HOMOs of (a) **1O**, (c) **1M**, and (e) **1N**, and LUMOs of (b) **1O**, (d)**1M**, and (f) **1N** based on DFT calculations (B3LYP/6-31G*).

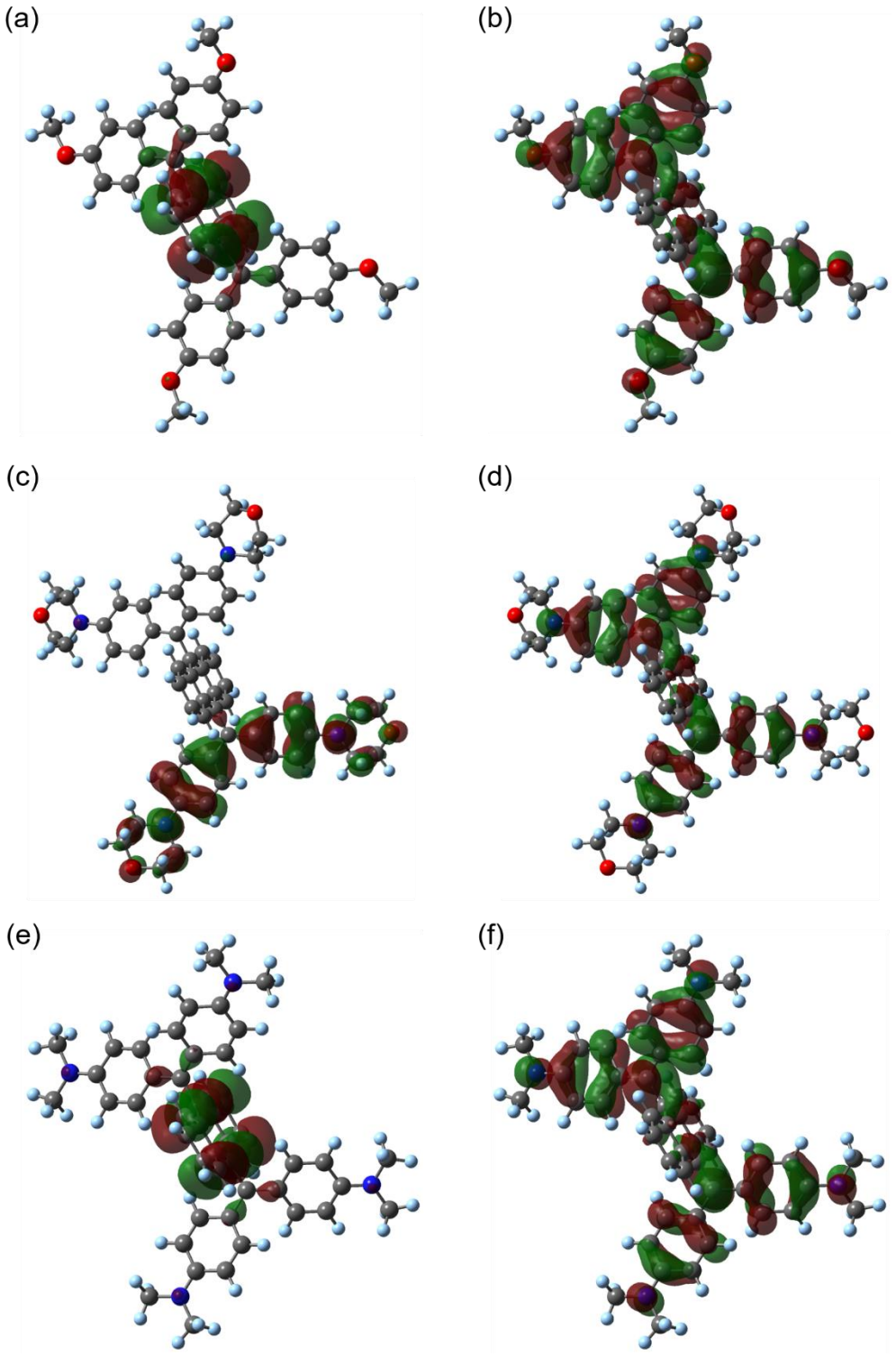

Figure 1-8. Optimized structures: HOMOs of (a) $\mathbf{1O}^{2+}$, (c) $\mathbf{1M}^{2+}$, and (e) $\mathbf{1N}^{2+}$, and LUMOs of (b) $\mathbf{1O}^{2+}$, (d) $\mathbf{1M}^{2+}$, and (f) $\mathbf{1N}^{2+}$ based on DFT calculations (B3LYP/6-31G*).

In order to gain further insight into the absorption properties of **1O**, **1M**, and **1N**, time-dependent (TD)-DFT calculations were performed at B3LYP/6-31G* level (Figure 1-9). As a result, simulated absorption spectra for **1O**, **1M**, and **1N** are in good agreement with the experimental results. For example, the most intense band (λ_{max} = 531 nm for $\mathbf{1O}^{2+}$, λ_{max} = 634 nm for $\mathbf{1M}^{2+}$, and λ_{max} = 628 nm for $\mathbf{1N}^{2+}$, respectively) is estimated to be the π-π* transition of the diarylmethylium units, which was supported by the color of the solution depending on the substituents on the aryl groups. On the other hand, the weak absorption in the long-wavelength region at $\mathbf{1O}^{2+}$ was inferred to be due to an intramolecular charge-transfer (CT), whereas those are not observed in $\mathbf{1M}^{2+}$ and $\mathbf{1N}^{2+}$, which is accounted for by high-lying LUMO level due to the higher donating ability of amino groups for $\mathbf{1M}^{2+}$ and $\mathbf{1N}^{2+}$, and thus, these CT bands are overlapped with the π-π* bands.

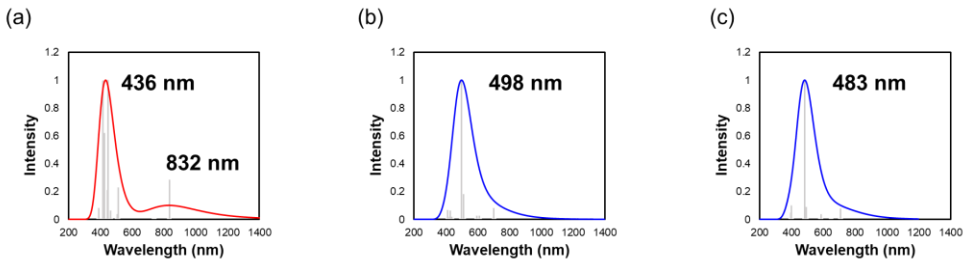

Figure 1-9. Simulated UV/Vis spectra of (a) $\mathbf{1O}^{2+}$, (b) $\mathbf{1M}^{2+}$, and (c) $\mathbf{1N}^{2+}$ obtained by TD-DFT calculations (B3LYP/6-31G*) based on the optimized structures.

1-2-5. Electrochromic Behavior in Solution

As shown in Figure 1-10, clean electrochromic behavior was observed upon constant-current electrochemical oxidation of the folded electron donor **1M** to generate twisted dication $\mathbf{1M}^{2+}$ in CH_2Cl_2. The yellow solution gradually turned deep blue with several isosbestic points, demonstrating that an intermediate radical species is short-lived in this process. Complete regeneration of **1M** accompanied by a color change from deep blue to the original yellow was confirmed by reduction of as-prepared $\mathbf{1M}^{2+}$ when the polarity of the electrodes was reversed (Figures 1-10a,b). Similar electrochromic behavior was observed for $\mathbf{1N}/\mathbf{1N}^{2+}$ as shown in Figures 1-10c,d. Notably, the electrochromic behaviors in UV/Vis spectra of $\mathbf{1M}/\mathbf{1M}^{2+}$ and $\mathbf{1N}/\mathbf{1N}^{2+}$ are quite similar to each other, due to the nearly identical band gap revealed by DFT study.

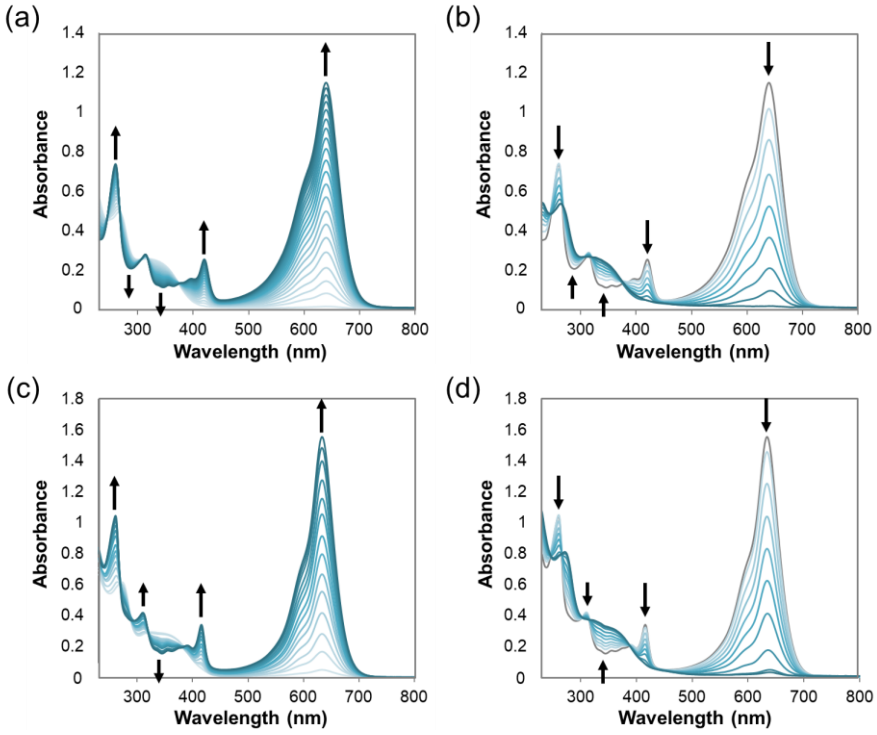

Figure 1-10. Change in the UV/Vis spectra of (a) **1M** (9.9 μM) and (c) **1N** (11 μM) upon constant-current electrochemical oxidation (20 μA, every 1 min) and (b) as-prepared $\mathbf{1M}^{2+}$ and (d) as-prepared $\mathbf{1N}^{2+}$ upon constant-current electrochemical reduction (20 μA, every 4 min) in CH_2Cl_2 containing 0.05 M Bu_4NBF_4 as a supporting electrolyte.

1-2-6. Mechanochromic Luminescence Behavior in a Solid State

The luminescence properties of the Ar_4AQDs **1O**, **1M**, and **1N** in the solid state are summarized in Table 1-4. As mentioned above, they are non-luminescent in solution, which can be accounted for by an AIE-type property as found in tetraarylethylenes. An as-synthesized powder of 4-methoxyphenyl derivative **1O** exhibits blue emission (λ_{em} 423 nm, Φ_{em} 44%). Green emissions for **1M** (λ_{em} 487 nm, Φ_{em} 29%) and **1N** (λ_{em} 502 nm, Φ_{em} 15%) were observed by using as-synthesized samples. By considering the structural flexibility of the folded configurations of **1O**, **1M**, and **1N**, these luminescence colors can be changed by an external stimulus such as grinding. These solid-state emissions were investigated in detail, since the author considered that mechanochromic luminescence could be realized.

Table 1-4. Luminescence properties of **1O**, **1M**, and **1N** in the solid state at 298K.

	λ_{em} [nm]	τ_1 [nm][c]	τ_2 [nm][c]	τ_{av} [nm][c]	Φ_{em}
$\mathbf{1O_B}$[a]	423	1.25	−	1.25	0.44
$\mathbf{1O_W}$[a]	568, 468	0.708	2.62	1.93	0.08
$\mathbf{1M_G}$[b]	487	0.570	1.63	1.49	0.29
$\mathbf{1M_Y}$[b]	703, 508	0.418	1.31	0.934	0.03
$\mathbf{1N_G}$[b]	502	0.672	1.63	1.33	0.15
$\mathbf{1N_Y}$[b]	690, 529	0.299	1.37	0.631	0.01

Excitation at [a]360 nm and at [b]300 nm. [c]Detection at the longer emission maximum.

Upon grinding the as-synthesized powder of **1O** with blue luminescence, which is referred to as $\mathbf{1O_B}$, the emission color changed to off-white ($\mathbf{1O_W}$: λ_{em} 568 and 468 nm, Φ_{em} 7.9%) as shown in Figures 1-11a, b and d. The ground $\mathbf{1O_W}$ emits over almost the entire visible region (400-700 nm). The PXRD pattern of $\mathbf{1O_W}$ indicates that the sample was transformed into an amorphous state (Figure 1-11f), whereas that of $\mathbf{1O_B}$ was assigned to a crystalline phase (Figure 1-11e). As shown in Figures 1-11c, g, the original PXRD pattern and emission color were recovered by treatment of $\mathbf{1O_W}$ with a small amount of ethyl acetate (EtOAc) followed by drying to regenerate $\mathbf{1O_B}$, demonstrating that **1O** exhibits mechanochromic luminescence behavior in the solid state based on the crystal-to-amorphous phase transition.

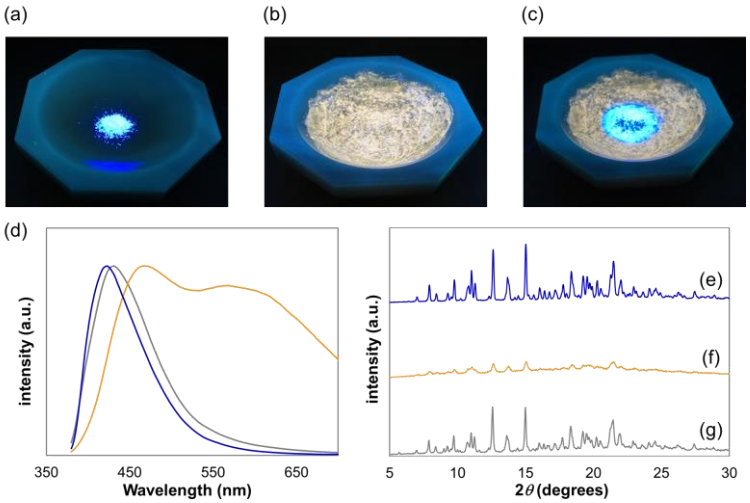

Figure 1-11. Photographs of **1O** under UV light in various states: (a) as-synthesized $\mathbf{1O_B}$, (b) ground $\mathbf{1O_W}$, and (c) $\mathbf{1O_B}$ recovered by treatment with EtOAc after grinding. (d) Changes in the emission spectrum for as-synthesized $\mathbf{1O_B}$ (blue), ground $\mathbf{1O_W}$ (orange), and recovered $\mathbf{1O_B}$ (gray). Changes in the PXRD pattern of (e) as-synthesized $\mathbf{1O_B}$ (blue), (f) ground $\mathbf{1O_W}$ (orange), and $\mathbf{1O_B}$ (gray) recovered by treatment with EtOAc after grinding.

In the case of **1M** and **1N**, similar mechanochromic behaviors, from the green emission of as-synthesized samples ($\mathbf{1M_G}$ and $\mathbf{1N_G}$) to yellow emission ($\mathbf{1M_Y}$ and $\mathbf{1N_Y}$) after grinding, arising from a crystal-to-amorphous phase transition, were observed, but they showed less reversibility, probably due to the lower crystallinity of **1M** and **1N** compared to **1O** (Figures 1-12 and 1-13). In particular, for **1N**, crystalline phase after a dissolving-drying process is different from the original one, suggesting a formation of EtOAc solvate. These two donors **1M** and **1N** also show lower emission quantum yields than **1O** for both as-synthesized and ground samples. These results suggest that the mechanochromic properties of Ar_4AQDs can be modified by the substituents on the aryl groups and that **1O** with less electron-donating ability is suitable for observing the mechanochromic response behavior.

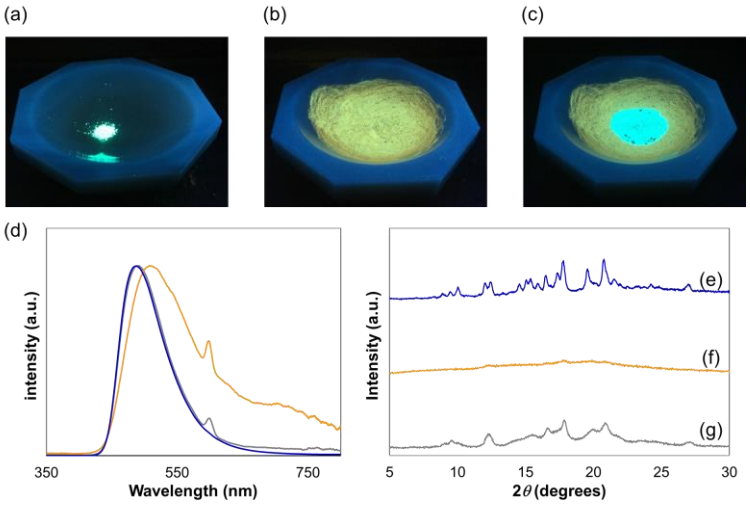

Figure 1-12. Photographs of **1M** under UV light in various states: (a) as-synthesized $\mathbf{1M_G}$, (b) ground $\mathbf{1M_Y}$, and (c) $\mathbf{1M_G}$ recovered by treatment with THF after grinding. (d) Changes in the emission spectrum for as-synthesized $\mathbf{1M_G}$ (blue), ground $\mathbf{1M_Y}$ (orange), and recovered $\mathbf{1M_G}$ (gray). Changes in the PXRD pattern of (e) as-synthesized $\mathbf{1M_G}$ (blue), (f) ground $\mathbf{1M_Y}$ (orange), and $\mathbf{1M_G}$ (gray) recovered by treatment with THF after grinding.

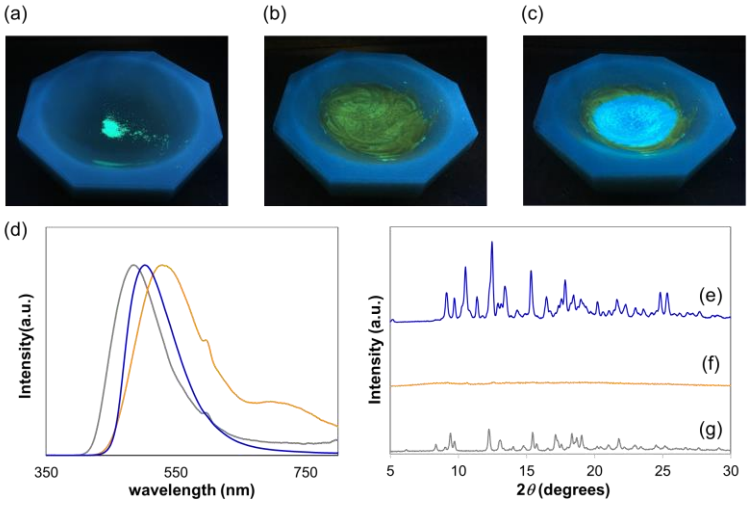

Figure 1-13. Photographs of **1N** under UV light in various states: (a) as-synthesized $\mathbf{1N_G}$, (b) ground $\mathbf{1N_Y}$, and (c) $\mathbf{1N_G}$ recovered by treatment with THF after grinding. (d) Changes in the emission spectrum for as-synthesized $\mathbf{1N_G}$ (blue), ground $\mathbf{1N_Y}$ (orange), and recovered $\mathbf{1N_G}$ (gray). Changes in the PXRD pattern of (e) as-synthesized $\mathbf{1N_G}$ (blue), (f) ground $\mathbf{1N_Y}$ (orange), and $\mathbf{1N_G}$ (gray) recovered by treatment with THF after grinding.

To investigate the detailed mechanism of mechanochromic luminescence, the author first examined the emission lifetimes of **1O$_B$** and **1O$_W$**. The results are summarized in Table 1-4. Single exponential decay was observed in the emission decay curve of **1O$_B$** (Figure 1-14a) and the lifetime was estimated to be 1.25 ns; thus, the blue emission was assigned to fluorescence. Upon grinding of **1O$_B$**, the emission decay curve of **1O$_W$** showed double exponential decay (Figure 1-14a) and the lifetimes were 0.71 and 2.62 ns. This means that **1O$_W$** in an amorphous state would contain multiple emissive species, and one possibility is the coexistence of another conformer such as a twisted structure. In the case of **1M** and **1N**, double exponential decay was observed for both as-synthesized and ground samples probably due to their lower crystallinity compared to **1O** (Figures 1-14b and c).

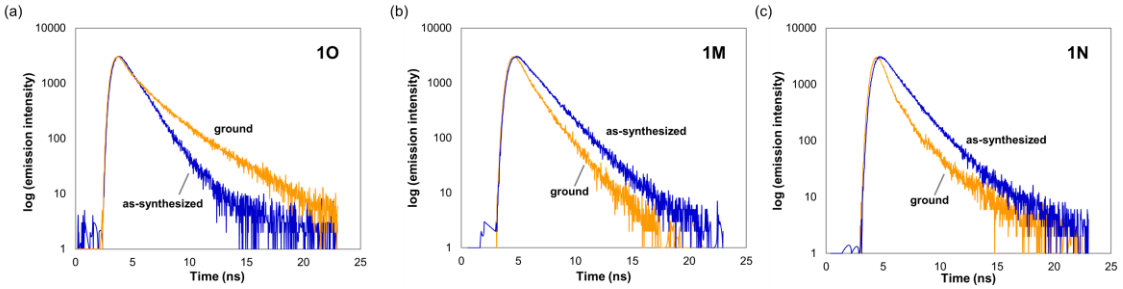

Figure 1-14. Emission decays of (a) **1O** for as-synthesized (blue), and ground (orange) samples, (b) **1M** for as-synthesized (blue), and ground (orange) samples, and (c) **1N** for as-synthesized (blue), and ground (orange) samples at 298 K (λ_{ex} = 300 nm for **1O**, 365 nm for **1M** and **1N**).

To gain insight into the presence of a twisted conformer, the author focused on Raman spectra of **1O** (Figure 1-15). If a twisted conformer of **1O** appeared in **1O$_W$**, the stretching vibration of the central C=C double bond would shift to lower wavenumbers (from around 1600 cm^{-1} to around 1400 cm^{-1}) because the twisted conformer should exhibit some contribution of a C-C single bond. However, the author did not observe a significant shift of the C=C stretching vibration, which appeared at around 1600 cm^{-1} between before and after grinding (Figure 1-15). Thus, it was revealed that there is no contribution of the twisted conformer after grinding of **1O$_W$**.

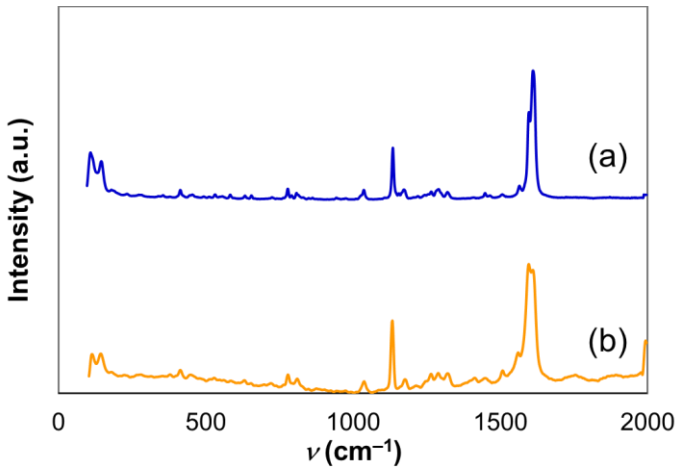

Figure 1-15. Raman spectra of (a) as-synthesized $\mathbf{1O_B}$ measured with a single crystal (blue) and (b) ground $\mathbf{1O_W}$ measured with a KBr pellet (orange) at 298 K.

By considering the emission lifetimes and Raman spectra of **1O**, it is most probable that mechanofluorochromic behavior can be accounted for by the formation of excimer in the amorphous state, since the emission maximum appeared at a longer wavelength and because double exponential decay was observed in $\mathbf{1O_W}$.

1-3. Conclusion

In this chapter, the author reports the Ar_4AQDs **1O**, **1M**, and **1N** exhibiting electrochromic and mechanofluorochromic behaviors. For electrochromism, it was revealed that the color of solution was modified by the substituents on the aryl groups. While the HOMO levels of folded donors differ by the electron-donating properties of aryl groups, the color of twisted dications $\mathbf{1M}^{2+}$ and $\mathbf{1N}^{2+}$ is nearly the same because of their similar band gaps as predicted by DFT calculations. Therefore, the operating voltage to exhibit electrochromism could be controlled without a change in long-wavelength absorption.

Furthermore, mechanofluorochromic behavior was observed for electron donors in a solid state on the basis of a crystal-to-amorphous phase transition. It is most probable that the observed red shift of the emission maximum upon grinding occurred by the formation of excimer in the amorphous state.

Thus, the author has demonstrated the Ar_4AQDs are the first examples exhibiting different chromism in different phases, namely, electrochromism in solution and mechanofluorochromism in the solid state.

1-4. Experimental Section

1-4-1. General

All reactions were carried out under an argon atmosphere. All commercially available compounds were used without further purification unless otherwise indicated. Dry CH_3CN was obtained by distillation from CaH_2 prior to use. Column chromatography was performed on silica gel I-6-40 (YMC) of particle size 40–63 μm, 60N (KANTO KAGAKU, spherical neutral), or Wakogel® 60N (neutral). ^1H and ^{13}C NMR spectra were recorded on a BRUKER Ascend™ 400 (^1H/400 MHz and ^{13}C/100 MHz) spectrometer. IR spectra were measured as a KBr pellet on a JEOL JIR-WINSPEC100 FT/IR spectrophotometer. Mass spectra were recorded on a JMS-T100GCV spectrometer in FD mode (GC-MS & NMR Laboratory, Research Faculty of Agriculture, Hokkaido University). Melting points were measured on a Yamato MP-21 or a Yanagimoto micro melting point apparatus and are uncorrected. Elemental analyses were performed on an EXETER ANALYTICAL CE440 at the Center for Instrumental Analysis of Hokkaido University. UV-Vis spectra were recorded on a Hitachi U-3500 spectrophotometer. Emission spectra were recorded on a JASCO FP-8600 spectrofluorometer. Emission quantum yields were measured on a Hamamatsu Photonics C9920-02 system. Emission lifetimes were measured on a Hamamatsu Photonics Quantaurus-Tau C11367 system. The analysis of Raman spectroscopy was carried out with an in Via Reflex at the OPEN FACILITY, Hokkaido University Sousei Hall. Redox potentials (E^{ox} and E^{red}) were measured by cyclic voltammetry in dry CH_2Cl_2 containing 0.1 M Bu_4NBF_4 as a supporting electrolyte. All of the values shown in the text are in E/V vs. SCE measured at the scan of 100 mVs^{-1}. Pt disk electrodes were used as the working and counter electrodes. The working electrodes was polished using a water suspension of aluminum oxide (0.05 μ) before use. DFT calculations were performed with the Gaussian 09W program package (Revision E.01, 2013, Gaussian Inc.,Wallingford, CT USA). The geometries of the compounds were optimized by using the B3LYP method in combination with the 6-31G* basis set.

1-4-2. Preparations

11,11,12,12-Tetrakis(4-morpholinophenyl)-9,10-anthraquinodimethane (1M)

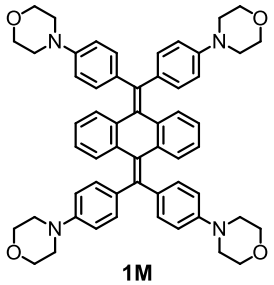

1M

A mixture of 11,11,12,12-tetrabromo-9,10-anthraquinodimethane[47] **2** (2.08 g, 4.00 mmol), 4-morpholinophenylboronic acid[48] **3M** (4.97 g, 24.0 mmol), K_2CO_3 (4.42 g, 32.0 mmol) and $Pd(PPh_3)_4$ (231 mg, 200 μmol) in toluene (90 mL), EtOH (9 mL) and water (9 mL) was stirred at 120 ℃ for 24 h. After cooling to 24 ℃, the precipitates were collected by filtration and washed with EtOAc to give **1M** (1.80 g) as a greenish yellow solid in 53% yield. The resulting filtrate was extracted with EtOAc three times. The combined organic layers were washed with water and brine, and dried over anhydrous $MgSO_4$. After filtration, the solvent was concentrated under reduced pressure. The crude product was purified by column chromatography on silica gel (hexane/EtOAc = 3/2) to give **1M** (1.23 g) as a greenish yellow solid in 36% yield (total 3.03 g, 89%).

Mp: 282-286 ℃ (decomp.); ^{1}H NMR (400 MHz, $CDCl_3$): δ/ppm 7.24 (8H, d, J = 8.8 Hz), 7.03 (4H, dd, J = 3.3, 5.8 Hz) , 6.80 (8H, d, J = 8.8 Hz), 6.73 (4H, dd, J = 3.3, 5.8 Hz), 3.84 (16H, t, J = 4.8 Hz), 3.14 (16H, t, J = 4.8 Hz); ^{13}C NMR (100 MHz, $CDCl_3$): δ/ppm 149.53, 138.86, 138.32, 134.93, 134.49, 130.65, 127.92, 124.87, 115.13, 66.93, 49.20; IR (KBr): ν/cm^{-1} 3061, 3029, 2959, 2891, 2852, 2819, 1606, 1554, 1513, 1449, 1378, 1334, 1303, 1256, 1229, 1195, 1121, 1068, 1050, 1033, 973, 931, 843, 821, 769, 752, 727, 698, 639, 626, 615, 591, 567, 526, 457, 447; LR-MS(FD) m/z (%): 848.49 (M^+, 6), 425.75 (5), 425.25 (22), 424.75 (64), 424.24(M^{2+}, bp), 423.74 (20), 423.24 (30); HR-MS (FD) Calcd. for $C_{56}H_{56}N_4O_4$: 848.43015; Found: 848.43016; UV/Vis (CH_2Cl_2): λ_{max}/nm (ε/M^{-1}cm^{-1}) 319 (25600), 267 (49900).

11,11,12,12-Tetrakis[4-(*N*,*N*-dimethylamino)phenyl]-9,10-anthraquinodimethane (1N)

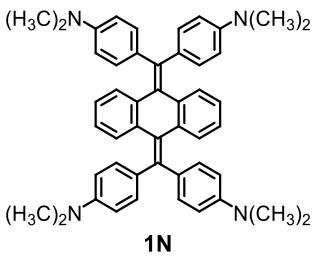

1N

A mixture of 11,11,12,12-tetrabromo-9,10-anthraquinodimethane[47] **2** (157 mg, 303 μmol), 4-(*N,N*-dimethylamino)phenylboronic acid[49] **3N** (299 mg, 1.81 mmol), K_2CO_3 (341 mg, 2.47 mmol) and $Pd(PPh_3)_4$ (17.8 mg, 15.4 μmol) in a mixture of toluene (15 mL), EtOH (1.5 mL) and water (1.5 mL) was stirred at 120 ℃ for 24 h. After cooling to 24 ℃, the reaction mixture was extracted with EtOAc three times. The combined organic layers were washed with water and brine, and dried over anhydrous $MgSO_4$. After filtration, the solvent was concentrated under reduced pressure. The crude product was purified by column chromatography on silica gel (hexane/EtOAc = 3) to give **1N** (176 mg) as a greenish yellow solid in 85% yield.

Mp: 248-251 ℃; ^{1}H NMR (400 MHz, $CDCl_3$): δ/ppm 7.20 (8H, d, J = 8.8 Hz), 7.09 (4H, dd, J = 3.3, 5.8 Hz) , 6.73 (4H, dd, J = 3.3, 5.8 Hz), 6.63 (8H, d, J = 8.8 Hz), 2.91 (24H, s); ^{13}C NMR (100 MHz, $CDCl_3$): δ/ppm 148.93, 139.45, 138.84, 134.10, 131.64, 130.72, 127.90, 124.53, 112.18, 40.64; IR (KBr): ν/cm^{-1} 3087, 3064, 3028, 2987, 2882, 2852, 2798, 1650, 1639, 1609, 1562, 1552, 1519, 1479, 1444, 1408, 1351, 1226, 1190, 1166, 1128, 1088, 1061, 973, 946, 836, 815, 770, 755, 737, 727, 650, 579, 544; LR-MS(FD) *m/z* (%): 681.43 (7), 680.43 (M^+, 13), 341.22 (16), 340.72 (57), 340.22 (M^{2+}, bp); HR-MS (FD) Calcd. for $C_{48}H_{48}N_4$: 680.38790; Found: 680.38947; UV/Vis (CH_2Cl_2): λ_{max}/nm (ε/M^{-1}cm^{-1}) 328 (26600), 272 (56000).

Anthracene-9,10-diyl-bis[bis(4-morpholinophenyl)methylium] Bis(hexachloroantimonate) [**1M**$^{2+}$ ($SbCl_6^-$)$_2$]

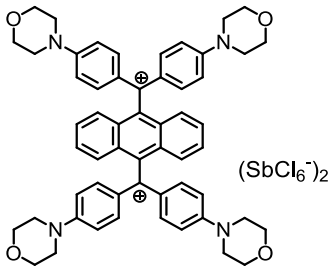

1M^{2+} ($SbCl_6^-$)$_2$

To a solution of 11,11,12,12-tetrakis(4-morpholinophenyl)-9,10-anthraquinodimethane **1M** (38.2 mg, 45.0 μmol) in dry CH_2Cl_2 (3 mL) was added tris(4-bromophenyl)aminium hexachloroantimonate (73.5 mg, 90.0 μmol) at 24℃, and the mixture was stirred for 30 min. The addition of dry ether led to precipitation of the dication salt. The precipitates were filtered, washed with dry ether three times, and dried under reduced pressure to give **1M**$^{2+}$ ($SbCl_6^-$)$_2$ (66.4 mg) as a black powder in 97% yield.

Mp: >300 ℃; ^{1}H NMR (400 MHz, CD_3CN): δ/ppm 7.69 (4H, dd, J = 3.3, 6.8 Hz), 7.58 (8H, d, J = 9.4 Hz) , 7.44 (4H, dd, J = 3.3, 6.8 Hz), 7.07 (8H, d, J = 9.4 Hz), 3.83 (16H, t, J = 4.8 Hz), 3.73 (16H, t, J = 4.8 Hz); ^{13}C NMR (100 MHz, $CDCl_3$): δ/ppm 157.15, 140.20, 136.86, 130.91, 130.26, 128.14, 126.90, 115.76, 66.58, 48.41; IR (KBr): ν/cm^{-1} 3080, 2963, 2916, 2855, 1613, 1579,, 1519,

1386, 1303, 1242, 1186, 1111, 1033, 958, 927, 909, 878, 825, 785, 768, 747, 715, 694, 668, 626, 604, 593, 549, 510; LR-MS(FD) *m/z* (%): 849.48 (22), 848.48 (M^+, 34), 440.21 (18), 425.24 (22), 424.74 (61), 424.23 (M^{2+}, bp), 423.73 (17), 423.23 (28); Anal. Calcd. (%) for $C_{56}H_{56}Cl_{12}N_4O_4Sb_2$: C 44.31, H 3.72, N 3.69; found: C 44.24, H 3.46, N 3.52; UV/Vis (CH_2Cl_2): λ_{max}/nm (ε/$M^{-1}cm^{-1}$) 634 (161000), 418 (32900), 312 (31700), 259 (98200).

Anthracene-9,10-diyl-bis{bis[4-(*N*,*N*-dimethylamino)phenyl]methylium} Bis(hexachloroantimonate) [**1N**$^{2+}$ ($SbCl_6^-$)$_2$]

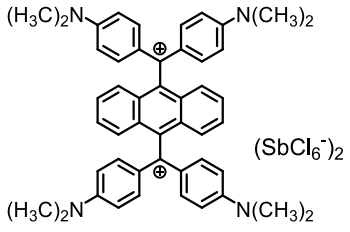

1N^{2+} ($SbCl_6^-$)$_2$

To a solution of 11,11,12,12-tetrakis[4-(*N,N*-dimethylamino)phenyl]-9,10-anthraquinodimethane **1N** (69.3 mg, 102 μmol) in dry CH_2Cl_2 (5 mL) was added tris(4-bromophenyl)aminium hexachloroantimonate (167 mg, 204 μmol) at 24 ℃, and the mixture was stirred for 30 min. The addition of dry ether led to precipitation of the dication salt. The precipitates were filtered, washed with dry ether three times, and dried under reduced pressure to give **1N**$^{2+}$ ($SbCl_6^-$)$_2$ (132 mg) as a black-brown powder in 96% yield.

Mp: >300 ℃; ^{1}H NMR (400 MHz, CD_3CN): δ/ppm 7.68 (4H, dd, *J* = 3.2, 6.9 Hz), 7.55 (8H, d, *J* = 9.2 Hz) , 7.42 (4H, dd, *J* = 3.2, 6.9 Hz), 6.95 (8H, d, *J* = 9.2 Hz), 3.33 (24H, s); ^{13}C NMR (100 MHz, $CDCl_3$): δ/ppm 171.62, 158.04, 140.24, 137.36, 131.31, 129.19, 128.36, 127.32, 115.47, 41.52; IR (KBr): *ν*/cm^{-1} 3079, 2926, 2861, 2814, 2363, 2343, 1615, 1584, 1483, 1463, 1453, 1441, 1421, 1367, 1169, 940, 910, 877, 827, 788, 769, 727, 695, 669, 596, 522; LR-MS(FD) *m/z* (%): 681.40 (20), 680.39 (M^+, 36), 341.20 (15), 340.70 (60), 340.20 (M^{2+}, bp); Anal. Calcd. (%) for $C_{56}H_{56}Cl_{12}N_4O_4Sb_2 \cdot 0.5(CH_2Cl_2)$: C 41.84, H 3.55, N 4.02; found: C 41.60, H 3.28, N 3.93; UV/Vis (CH_2Cl_2: λ_{max}/nm (ε/$M^{-1}cm^{-1}$) 628 (187000), 414 (35500), 308 (37400), 259 (103000).

Reduction of dication salt **1M**$^{2+}$ ($SbCl_6^-$)$_2$ to **1M**

To a solution of **1M**$^{2+}$ ($SbCl_6^-$)$_2$ (131 mg, 86.6 μmol) in dry CH_3CN (10 mL) was added activated zinc powder (1.13 g, 17.3 mmol) at 25 ℃. The mixture was stirred for 1 h, and then diluted with water. The whole mixture was extracted with CH_2Cl_2 three times. The combined organic layers were washed with water and brine, and dried over anhydrous $MgSO_4$. After filtration, the solvent was concentrated under reduced pressure to give **1M** (73.1 mg) as a greenish yellow solid in 100% yield.

Reduction of dication salt $\mathbf{1N}^{2+}$ $(SbCl_6^-)_2$ to **1N**

To a solution of $\mathbf{1N}^{2+}$ $(SbCl_6^-)_2$ (91.2 mg, 65.4 μmol) in dry CH_3CN (13 mL) was added activated zinc powder (887 mg, 13.6 mmol) at 23 ℃. The mixture was stirred for 1 h, and then diluted with water. The whole mixture was extracted with EtOAc three times. The combined organic layers were washed with water and brine, and dried over anhydrous $MgSO_4$. After filtration, the solvent was concentrated under reduced pressure to give **1N** (44.5 mg) as a greenish yellow solid in 98% yield.

11,11,12,12-Tetrabromo-9,10-anthraquinodimethane (2)

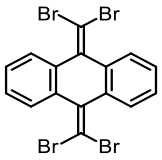

2

To a solution of 9,10-anthraquinone (4.17 g, 20.1 mmol) and CBr_4 (17.7 g, 53.4 mmol) in dry CH_2Cl_2 (300 mL) was added PPh_3 (27.4 g, 104 mmol) at 26 ℃. After stirring at 26 ℃ for 14.5 h, the precipitates were filtered and washed with CH_2Cl_2. The resulting filtrate was extracted with CH_2Cl_2 three times. The combined organic layers were washed with water and brine, and dried over anhydrous $MgSO_4$. After filtration, the solvent was concentrated under reduced pressure. The crude product was purified by column chromatography on silica gel (hexane) to give **2** (8.44 g) as a colorless crystal in 81% yield.

^{1}H NMR data were identical to those in literature.[47]

1-4-3. X-ray analyses

Data were collected with a Rigaku Mercury 70 diffractometer (Mo-Kα radiation, λ = 0.71075 Å) for **1N**, **1M**$^{2+}$, and **1N**$^{2+}$ and a Rigaku XtaLAB Synergy (Cu-Kα radiation, λ = 1.54184 Å) for **1O** and **1M**. The structure was solved by the direct method (SIR2004) or ShelXT (Sheldrick) and refined by the full-matrix least-squares method on F^2 with anisotropic temperature factors for non-hydrogen atoms. All the hydrogen atoms were located at the calculated positions and refined with riding.

Crystal data of **1O**

Crystals were obtained by recrystallization from EtOAc/hexane. MF: $C_{44}H_{36}O_4$, FW: 628.73, clear light colorless block, 0.40 × 0.40 × 0.20 mm^3, triclinic $P\bar{1}$, a = 10.81354(14) Å, b = 10.86215(13) Å, c = 15.3552(2) Å, α = 103.8333(11)°, β = 93.9383(2)°, γ = 107.1145(11)°, V = 1654.84(4) Å^3, ρ (Z = 2) = 1.262 g·cm^{-3}. A total of 19220 reflections were measured at T = 150 K. Numerical absorption correction was applied (μ = 0.628 mm^{-1}). The final $R1$ and $wR2$ values are 0.0421 ($I > 2\sigma I$) and 0.1087 (all data) for 6666 reflections and 437 parameters. Estimated standard deviations are 0.0014-0.0019 Å for bond lengths and 0.09-0.12° for bond angles. CCDC 1906562

Crystal data of **1M**·CH_2Cl_2

Crystals were obtained by recrystallization from CH_2Cl_2/hexane. MF: $C_{57}H_{58}N_4O_4Cl_2$, FW: 933.97, clear light yellow plate, 0.20 × 0.20 × 0.02 mm^3, monoclinic $P2_1/n$, a = 14.4210(6) Å, b = 13.6809(5) Å, c = 26.3009(9) Å, β = 97.511(3)°, V = 5144.4(3) Å^3, ρ (Z = 4) = 1.206 g·cm^{-3}. A total of 29131 reflections were measured at T = 150 K. Numerical absorption correction was applied (μ = 1.520 mm^{-1}). The final $R1$ and $wR2$ values are 0.0993 ($I > 2\sigma I$) and 0.2952 (all data) for 10256 reflections and 604 parameters. Estimated standard deviations are 0.005-0.008 Å for bond lengths and 0.3-0.5° for bond angles. Solvent mask procedure was used for the analysis. CCDC 1906563

Crystal data of **1N**

Crystals were obtained by recrystallization from EtOAc/hexane. MF: $C_{48}H_{48}N_4$, FW: 680.93, yellow block, 0.30 × 0.20 × 0.20 mm^3, monoclinic $P2_1/c$, a = 13.1937(9) Å, b = 16.1412(9) Å, c = 18.7248(10) Å, β = 104.298(3)°, V = 3864.2(4) Å^3, ρ (Z = 4) = 1.170 g·cm^{-3}. A total of 28828 reflections were measured at T = 150 K. Numerical absorption correction was applied (μ = 0.683 cm^{-1}). The final $R1$ and $wR2$ values are 0.0570 ($I > 2\sigma I$) and 0.1557 (all data) for 7541 reflections and 477 parameters. Estimated standard deviations are 0.003-0.004 Å for bond lengths and 0.14-0.20° for bond angles. CCDC 1906564

Crystal data of **1M**$^{2+}$ $(SbCl_6^-)_2$·$2(CH_3NO_2)$

Crystals were obtained by recrystallization from CH_3NO_2/Et_2O. MF: $C_{58}H_{62}Cl_{12}N_6O_8Sb_2$, FW: 1640.10, blue plate, 0.30 × 0.30 × 0.02 mm^3, monoclinic $P2_1/c$, a = 9.910(2) Å, b = 29.014(7) Å, c

= 12.469(3) Å, β = 108.766(3)°, V = 3395(2) Å^3, ρ (Z = 2) = 1.604 g·cm^{-3}. A total of 21405 reflections were measured at T = 150 K. Numerical absorption correction was applied (μ = 13.213 cm^{-1}). The final $R1$ and $wR2$ values are 0.0548 (I > 2σI) and 0.1513 (all data) for 5306 reflections and 404 parameters. Estimated standard deviations are 0.0018-0.04 Å for bond lengths and 0.07-5.0° for bond angles. CCDC 1906565

Crystal data of **1N**$^{2+}$ ($SbCl_6^-$)$_2$·3(1,4-dioxane)

Crystals were obtained by recrystallization from CH_3CN/1,4-dioxane. MF: $C_{60}H_{72}Cl_{12}N_4O_6Sb_2$, FW: 1614.19, dark blue plate, 0.40 × 0.20 × 0.05 mm^3, monoclinic $P2_1/c$, a = 9.829(3) Å, b = 18.272(6) Å, c = 19.131(7) Å, β = 92.662(6)°, V = 3432(2) Å^3, ρ (Z = 2) = 1.562 g·cm^{-3}. A total of 25303 reflections were measured at T = 150 K. Numerical absorption correction was applied (μ = 13.025 cm^{-1}). The final $R1$ and $wR2$ values are 0.0505 (I > 2σI) and 0.1533 (all data) for 6715 reflections and 383 parameters. Estimated standard deviations are 0.0014-0.01 Å for bond lengths and 0.05-0.7° for bond angles. CCDC 1906566

Chapter 2

Demonstration of Polymorph-Dependent Color Tone and Emission of Crystals Based on Exceptionally Flexible Overcrowded Ethylenes with Multiple Conformations

2-1. Introduction

As mentioned in general introduction (Chapter 0), the construction of stimuli-responsive systems based on a conformational change of the molecule will lead to the development of materials that can switch both color tone and emission color. The most promising candidates are OCEs, in which the large difference in electronic configuration between their **F**- and **T**-forms can be used. However, the molecular design strategy is limited to BAEs with rigid and planar tricyclic aromatic groups among OCEs. In addition, such stimuli-responsive behavior is also limited to that derived from the conformational change between two states in almost all systems. Therefore, the author aimed to construct a unique molecule that can adopt not only **F**- and **T**-forms but also other conformations [e.g., planar (**P**) and twisted-folded (**TF**) forms], so that unprecedented switching behavior could be achieved with the involvement of multiple states.

BAEs, which have the moderate rigidity of the tricyclic aromatic groups linked to both sides of the central C=C double bond, have been used to realize stimuli-responsive systems involving multiple-conformations derived from nonplanar alkenes. Indeed, not BAE-type OCEs, Ar_4AQDs **1** with four freely rotatable aryl groups as shown in Chapter 1, generally adopt the **F**-form in both solid and

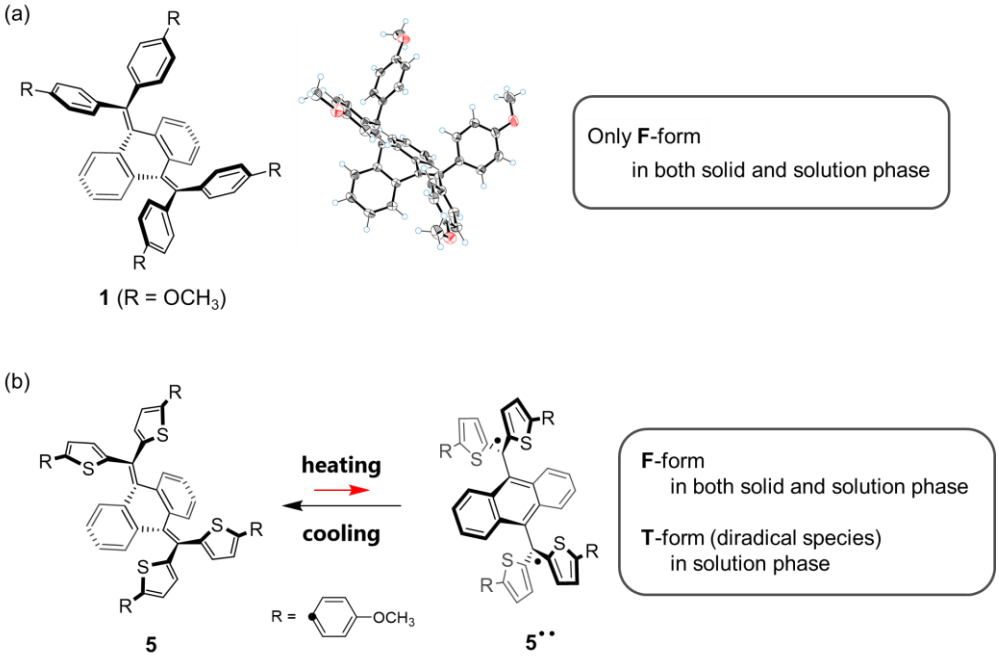

Figure 2-1. Molecular conformations of (a) Ar_4AQD **1** and (b) Th_4AQD **5**.

solution phases (Figure 2-1a).[53] On the other hand, the author's group recently found that tetrathienylanthraquinodimethane (Th_4AQD) **5**, which is also a class of monotricyclic aromatic enes (MAEs), exhibits the closed-shell **F**-form in crystals and low-temperature solution, whereas the open-shell **T**-form (diradical species) also contributes in high-temperature solution (Figure 2-1b).[27] This is a unique example in which the **T**-form appears in thermal equilibrium with the **F**-form accompanied by switching of redox properties between **T**- and **F**-forms for MAE-type OCEs.

However, the presence of the **T**-form was confirmed only in solution and it provided a negligibly small contribution. In addition, it should be noted that the introduction of thienyl groups into the AQD skeleton, as in compound **5**, preferred the "open-shell" **T**-form. While open-shell species are interesting from the viewpoint of their potential applications, their high reactivity often causes a problem in handling. Therefore, the author envisaged that further functional molecules that exhibit drastic changes in absorption and emission based on the conformers with different electronic configurations should be obtained when MAE-type molecules could exhibit the closed-shell **T**-form and other conformations in addition to the **F**-form.

In this chapter, the author reports N_4AQD derivatives **2a-d**, which can adopt both the closed-shell **T**- and **F**-forms in crystals by reducing the steric hindrance in the overcrowded fjord region (Figure 2-2). Furthermore, the author has also succeeded in creating not only these two structures, but also several intermediate structures in polymorphs. In other words, the author modulated the photophysical properties based on the conformation observed in the crystal. Generally, since dynamically averaged physical properties are observed in solution, the present results represent the first example where color tone and emission color are based on multiple conformations in the crystal that can be generated by recrystallization from appropriate solvents.

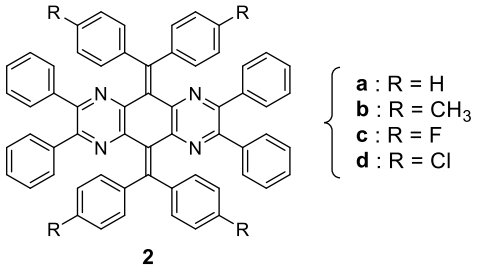

2

Figure 2-2. Tetraazaanthraquinodimethane (N_4AQD) derivatives **2a**, **2b**, **2c**, and **2d**.

2-2. Results and Discussion

2-2-1. Molecular Design

On the basis of the difference in structures found in quinodimethane derivatives **1** and **5**, the author expected that the conformations could be significantly affected by a change in steric hindrance around the central C=C double bond. Therefore, the author considered that the decrease in steric hindrance in the fjord region would be key for creating the **T**-form for MAE-type OCEs. At the same time, to control the conformations of MAEs, the author proposes a new strategy: reducing the steric hindrance in the overcrowded fjord region by replacing the C-H moiety of the central AQD skeleton with nitrogen atom (derivative **6**, Figure 2-3a). Instead of an approach that uses thienyl groups, which contribute to the stabilization of open-shell species, the introduction of pyrazine rings into the central AQD skeleton is designed to reduce the aromaticity of the tricyclic core and allow the skeleton itself to twist.

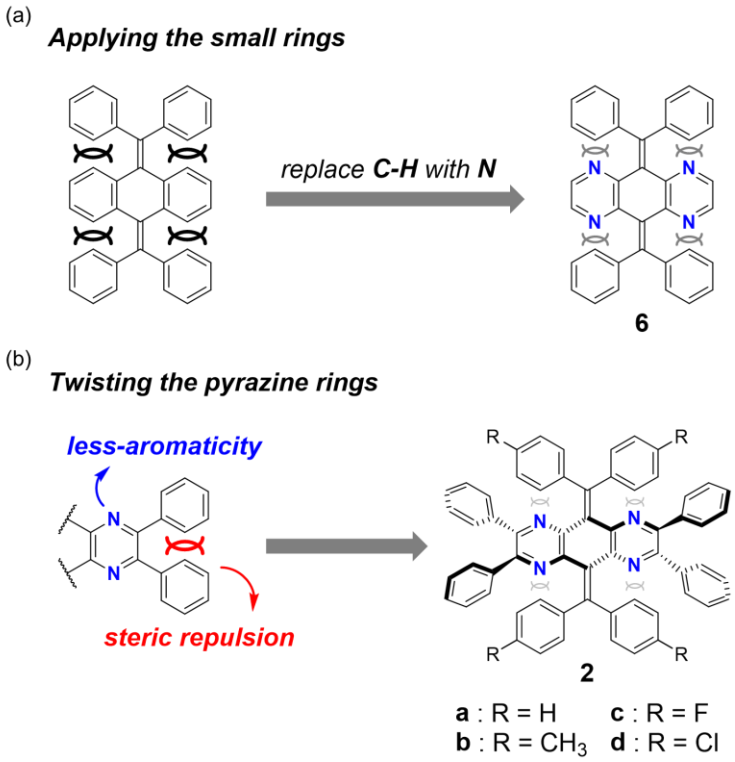

Figure 2-3. Author's approaches to create **T**-form for AQD derivative.

Before starting the synthesis, the author performed density functional theory (DFT) calculations at the (U)B3LYP/6-31G* level for N_4AQDs **6** (as well as **1** and **5** for comparison). The results showed that the closed-shell **T**-form in **6** is significantly stabilized compared to those in **1** and **5**, but the **T**-form is still calculated as a transition state with one imaginary frequency even for **6** (Table 2-1).

Table 2-1. Relative energies of **1**, **5**, **6**, **7** and **2a** based on the optimized structures obtained by DFT calculations [(U)B3LYP/6-31G*].

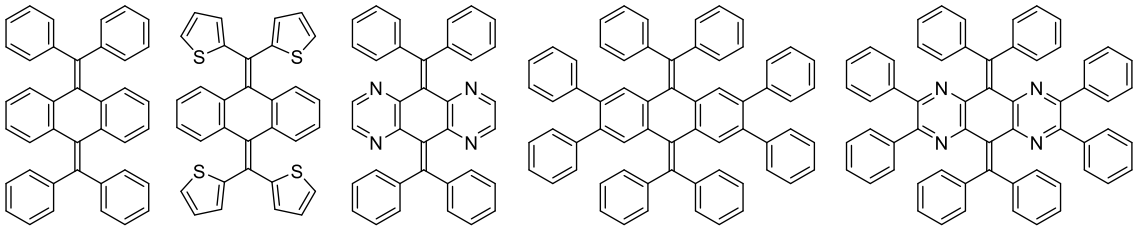

1 (Ar = Ph) **5** (R = H) **6** **7** **2a**

ΔE_{rel} [kcal/mol]	**F**-form	**T**-form	**T**-form (diradical)	
			Singlet	Triplet
1H	0	14.0[a]	13.6	13.9
5	0	9.40	2.31	2.35
6	0	3.35[a]	14.3	16.1
7	0	11.3	12.8	13.4
2a	3.15	0	10.9	13.9

[a] Optimized as a transition-state structure.

Table 2-2. Relative energies of **2a-d** based on the optimized structures obtained by DFT calculations [(U)B3LYP/6-31G*].

ΔE_{rel} [kcal/mol]	**F**-form	**T**-form	**T**-form (diradical)	
			Singlet	Triplet
2a (R = H)	3.15	0	10.9	13.9
2b (R = CH_3)	3.45	0	10.7	14.0
2c (R = F)	2.86	0	10.8	14.0
2d (R = Cl)	2.74	0	10.3	12.9

Thus, to obtain the **T**-form as a stable structure, the author decided to use an additional approach to perturb the crystal structure by the introduction of two *vic*-diphenyl groups into both sides of the central N_4AQD skeleton (compound **2**, Figure 2-3b). This strategy can induce a further twisting of the less-aromatic pyrazine ring due to steric repulsion between adjacent phenyl groups, resulting in a decrease in steric hindrance between the N_4AQD core and the aryl groups on the exocyclic bonds to make the **T**-form more stable. DFT calculations were then performed on the N_4AQD derivative **2**,

which suggested that the **T**-form would be obtained as the most stable structure and the **F**-form would also exist as a metastable structure (Tables 1 and 2). The results of the DFT study for non-aza analogue **7** confirmed the validity of our molecular design. Thus, the author focuses on N_4AQDs with peripheral phenyl groups, with the expectation that both the **F**- and **T**-forms could appear in crystals, and designed four derivatives **2a**-**d** to investigate the effect of the steric and electronic properties of the substituent at the 4-position on each of the aryl groups (Table 2).

Table 2. Hammett's σ_p values[54] about CH_3, H, F, and Cl groups, which are the substituents at the 4-position on the aryl groups of N_4AQDs **2**.

	gas phase σ_p	**benzene solution** σ_p	**aqueous solution** σ_p	σ_p^+
CH_3	-0.07	-0.11	-0.17	-0.31
H	0.00	0.00	0.00	0.00
F	0.19	0.17	0.06	-0.07
Cl	0.29	0.27	0.23	0.11

2-2-2. Preparation

The newly designed N_4AQD derivatives **2a-d** were synthesized as follows (Scheme 2-1). First, the dehydrative condensation of 2,3,5,6-tetraamino-1,4-benzoquinone **8**[55] with benzil, and subsequent double dibromo-olefination led to the precursor **10**.[56] Next, Suzuki-Miyaura cross-coupling reactions of **10** with the corresponding boronic acid or boroxine afforded the desired N_4AQD derivatives **2a-d** in 78-99% yields.

Scheme 2-1. Preparation of N_4AQDs **2**.

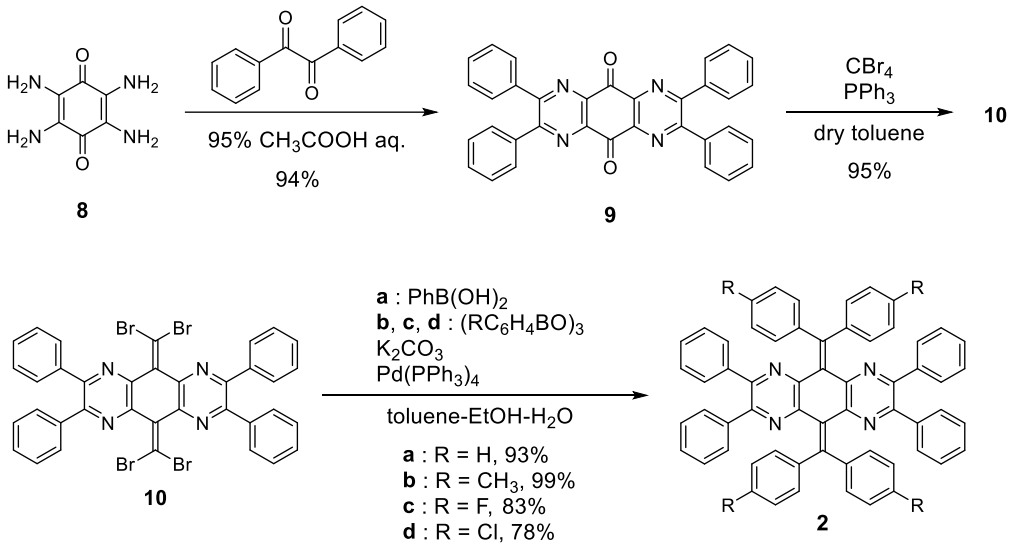

Reference compounds **1**, **6**, and **7** were synthesized from 9,10-anthraquinone, 2,3,5,6-tetraamino-1,4-benzoquinone, and 1,4-benzoquinone, respectively, in a similar manner (Scheme 2-2).

Scheme 2-2. Preparation of reference compounds (**1**, **6**, and **7**).

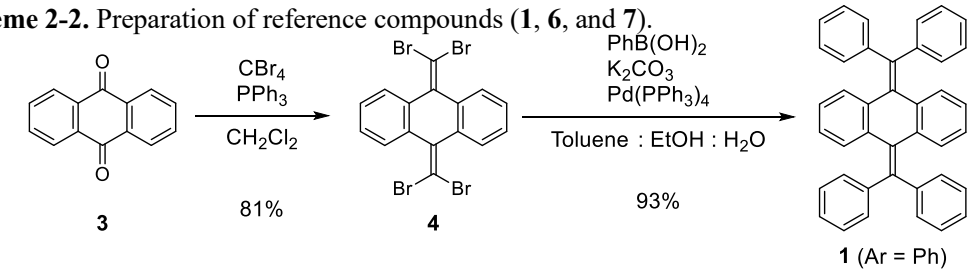

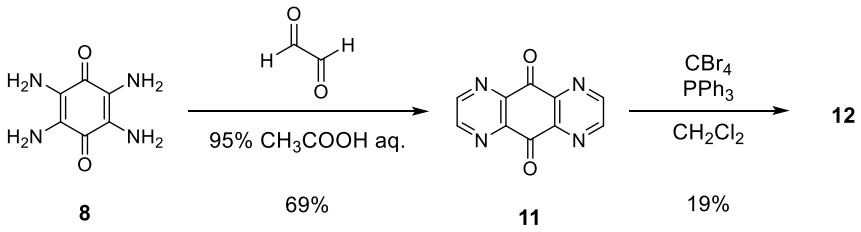

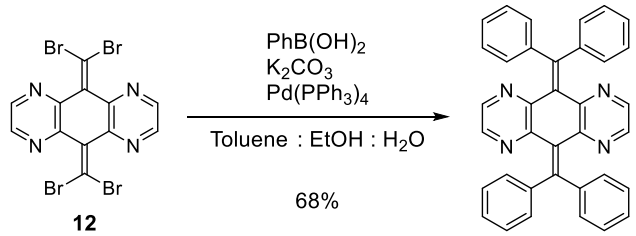

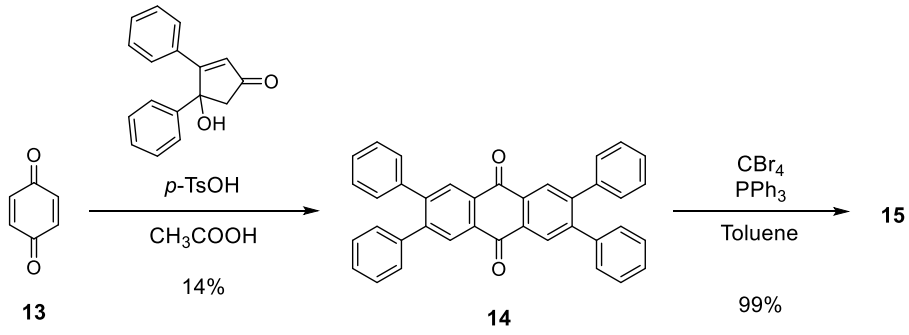

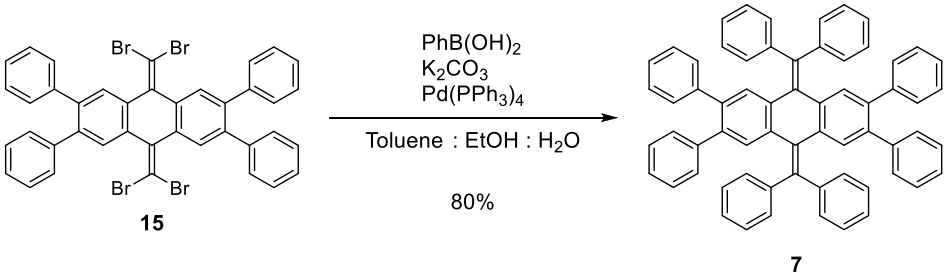

2-2-3. Investigation in a Solution-phase Properties

To gain insight into the solution-phase structure of the N_4AQD derivatives, the UV/Vis spectrum of the parent phenyl derivative **2a** (R = H) was measured in CH_2Cl_2. Compared to the spectra of the reference compounds **1**, **6**, and **7**, a red shift of the absorption maxima was clearly observed (λ_{max} = 440 nm for **2a** and $\lambda_{max} \approx$ 320 nm for **1**, **6**, and **7**), and the solution of **2a** is reddish-orange whereas those of **1**, **6** and **7** are colorless to pale yellow (Figure 2-4, Table 2-3).

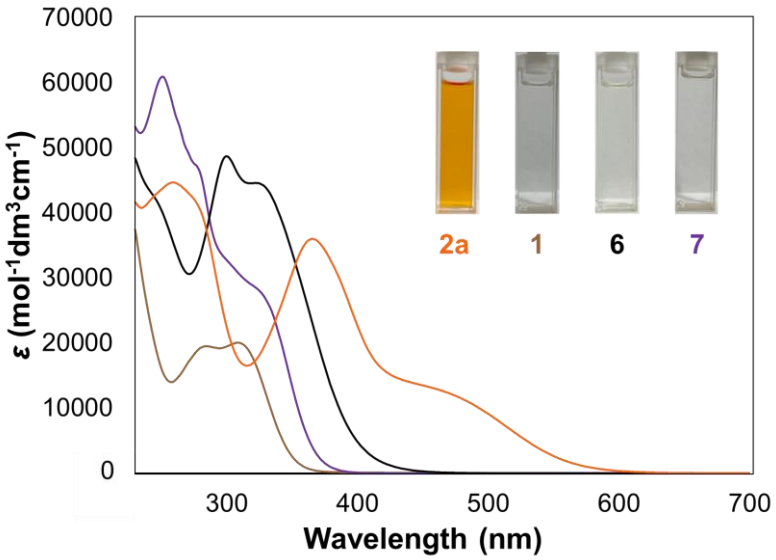

Figure 2-4. UV/Vis spectra of **2a**, **1**, **6**, and **7** in CH_2Cl_2.

Table 2-3. Experimental and theoretical absorption properties of **2a**, **1**, **6**, and **7**. Shoulder peaks are marked with "sh". λ_{end} is the absorption end of each spectrum. The energy gap $\Delta E^{DFT}_{LUMO\text{-}HOMO}$ was estimated by DFT calculations (B3LYP/6-31G*).

	λ_{max} [nm] (log ε)	λ_{end} [nm]	$\Delta E^{DFT}_{LUMO\text{-}HOMO}$ [eV] / [nm]
2a (Ph_8N_4AQD)	sh 440 (4.15) 366 (4.56) 259 (4.65)	657	3.50 / 354 (**F**-form) 2.38 / 520 (**T**-form)
1 (Ph_4AQD)	308 (4.30) 285 (4.29)	453	4.11 / 302
6 (Ph_4N_4AQD)	322 (4.65) 300 (4.69)	498	3.67 / 338
7 (Ph_8AQD)	sh 326 (4.44) sh 276 (4.68) 251 (4.78)	409	3.88 / 319

The HOMO-LUMO gaps of each derivative predicted by DFT calculations were estimated to be 4.11 eV, 3.67 eV, and 3.87 eV for the **F**-forms of **1**, **6**, and **7**, respectively, and 2.38 eV for the **T**-form of **2a**, which is in good agreement with the trend of the absorption end of each derivative (Table 2-3). These results suggest that only **2a** can have a contribution from a twisted structure in solution. In addition, the UV/Vis spectra of **2b** (R = CH_3), **2c** (R = F), and **2d** (R = Cl) in CH_2Cl_2 were almost the same as that of **2a** (Figure 2-5, Table 2-4), indicating that all N_4AQD derivatives **2** have contributions from the **T**-form.

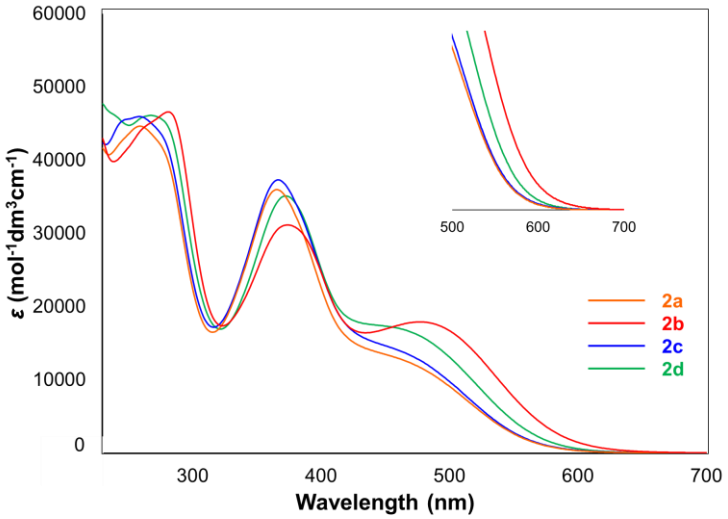

Figure 2-5. UV/Vis spectra of **2a**, **2b**, **2c**, and **2d** in CH_2Cl_2.

Table 2-4. Experimental and theoretical absorption properties of **2a**, **2b**, **2c**, and **2d**. Shoulder peaks are marked with "sh". The λ_{end} is the absorption end of each spectrum. The energy gap $\Delta E^{DFT}_{LUMO\text{-}HOMO}$ was estimated by DFT calculations (B3LYP/6-31G*).

	λ_{max} [nm] (log ε)	λ_{end} [nm]	$\Delta E^{DFT}_{LUMO\text{-}HOMO}$ [eV] / [nm]
2a	sh 440 (4.15) 366 (4.56) 259 (4.65)	657	3.50 / 354 (**F**-form) 2.38 / 520 (**T**-form)
2b	477 (4.25) 374 (4.49) 281 (4.67)	711	3.44 / 361 (**F**-form) 2.33 / 532 (**T**-form)
2c	sh 443 (4.18) 367 (4.57) 259 (4.66)	683	3.39 / 365 (**F**-form) 2.35 / 529 (**T**-form)
2d	sh 435 (4.25) 373 (4.55) 268 (4.66)	668	3.34 / 371 (**F**-form) 2.31 / 536 (**T**-form)

According to variable-temperature (VT) ^{1}H NMR analysis of derivative **2b**, no broadening of signals was observed upon heating from 303 K to 393 K in DMSO-d_6 (Figure 2-6). Thus, there is no contribution of open-shell species. On the other hand, some proton signals shifted upon heating in DMSO-d_6 and cooling in CD_2Cl_2 (Figures 2-6, 7).

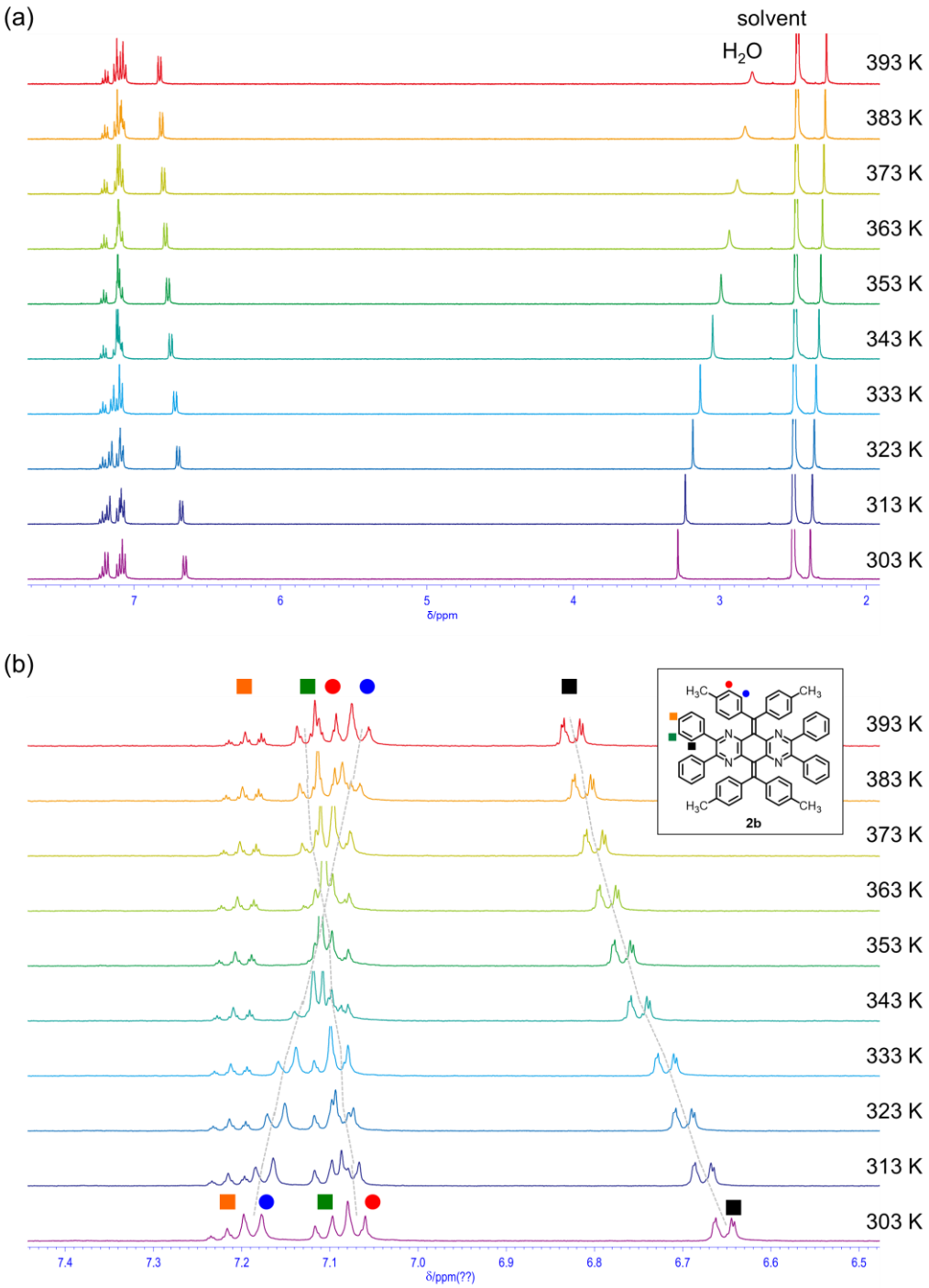

Figure 2-6. (a) VT ^{1}H NMR spectra of **2b** in DMSO-d_6 from 303 K to 393 K (every 10 K), and (b) enlarged view of aromatic region.

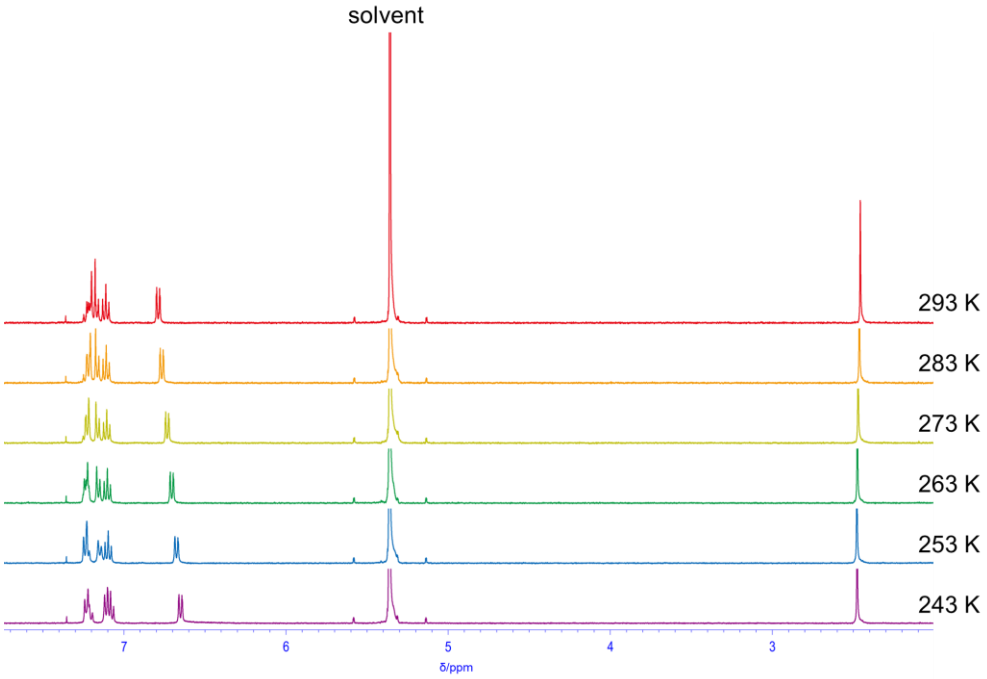

Figure 2-7. VT ^{1}H NMR spectra of **2b** in CD_2Cl_2 from 293 K to 203 K (every 10 K).

To clarify the reason why some proton signals shifted upon temperature change in the VT ^{1}H NMR spectra of **2b**, VT UV/Vis measurement was also carried out from 293 K to 373 K in DMSO (Figure 2-8). As the temperature increased, a decrease in the absorption band around 500 nm was observed, and the color of the solution changed from reddish-orange to nearly yellow.

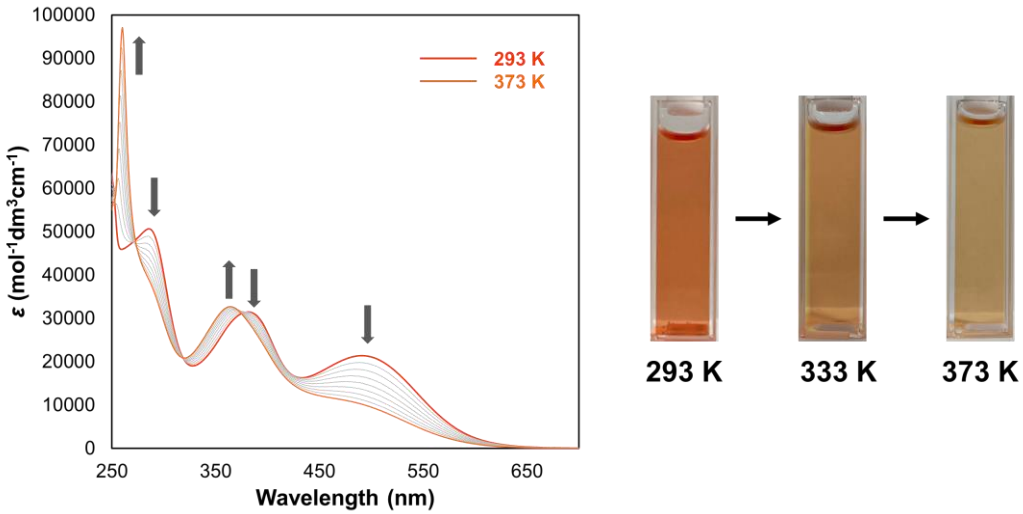

Figure 2-8. VT UV/Vis spectra of **2b** in DMSO from 293 K to 373 K (every 10 K).

These observations clearly indicate that the **F**- and **T**-forms are in thermal equilibrium in solution, and it seems that the contribution of the metastable **F**-form increases at higher temperature according to the Boltzmann distribution. Due to the rapid change in structures, all N_4AQD derivatives **2** are non-fluorescent in solution. Such fluorescence quenching can often be observed in tetraarylethylenes,[24,25] which are the representative molecules with aggregation-induced emission properties.[23]

2-2-4. X-ray Analyses

Since the presence of the **T**-form was indicated for N_4AQD derivatives (**2**), the author turned our attention to their structures and photophysical properties in the solid states. X-ray structures were investigated using single crystals of N_4AQD derivatives **2a-d**, which were obtained by recrystallization from various solvents. For the tolyl derivative **2b**, recrystallization from EtOAc/EtOH produced yellow crystals as EtOH solvate, while that from EtOAc/hexane provided red crystals without any solvent. X-ray analyses of both crystals revealed that **2b** adopts the **F**- and **T**-forms in yellow crystals containing EtOH and red crystals, respectively (Figure 2-9a).

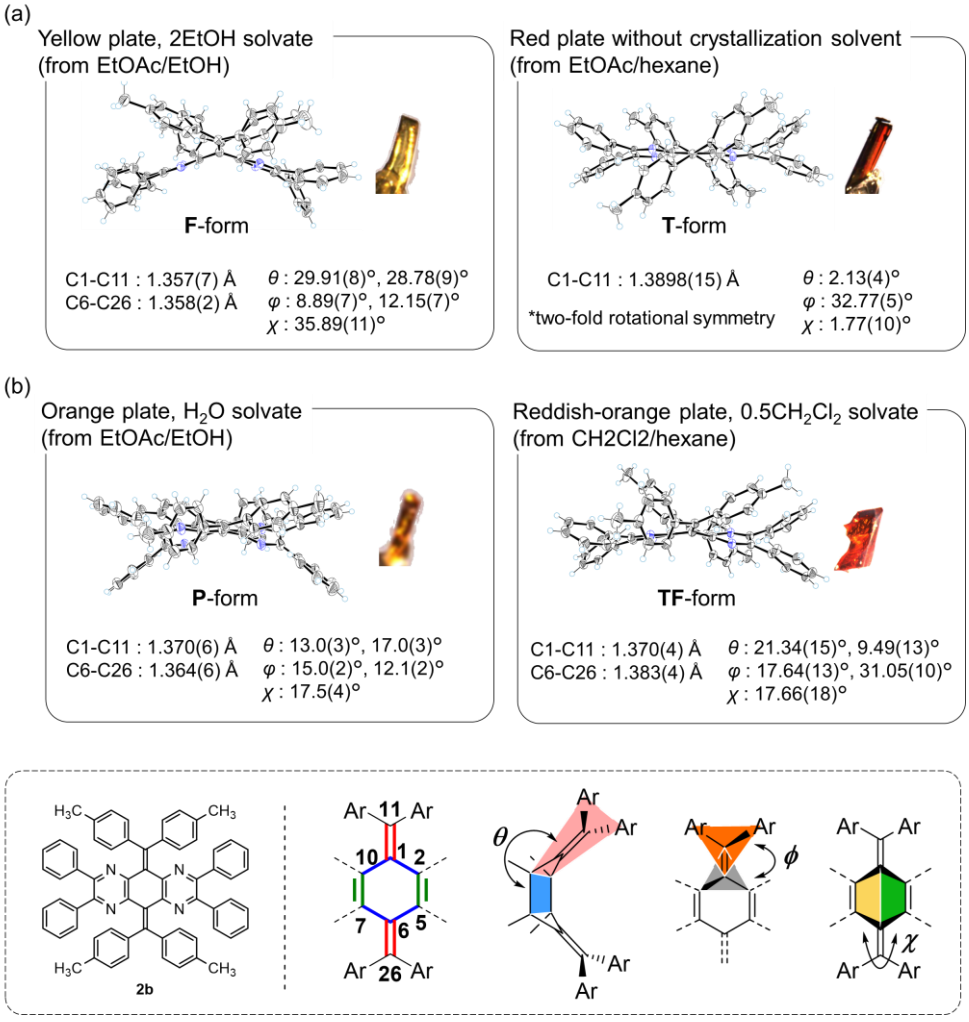

Figure 2-9. ORTEP drawings of **2b** [(a) **F**-form in 2EtOH solvate (recrystallized from EtOAc/EtOH) and **T**-form without any solvent (recrystallized from EtOAc/hexane), and (b) **P**-form in H_2O solvate (recrystallized from EtOAc/EtOH) and **TF**-form in $0.5CH_2Cl_2$ solvate (recrystallized from CH_2Cl_2/hexane)]. The solvent molecules are omitted for clarity.

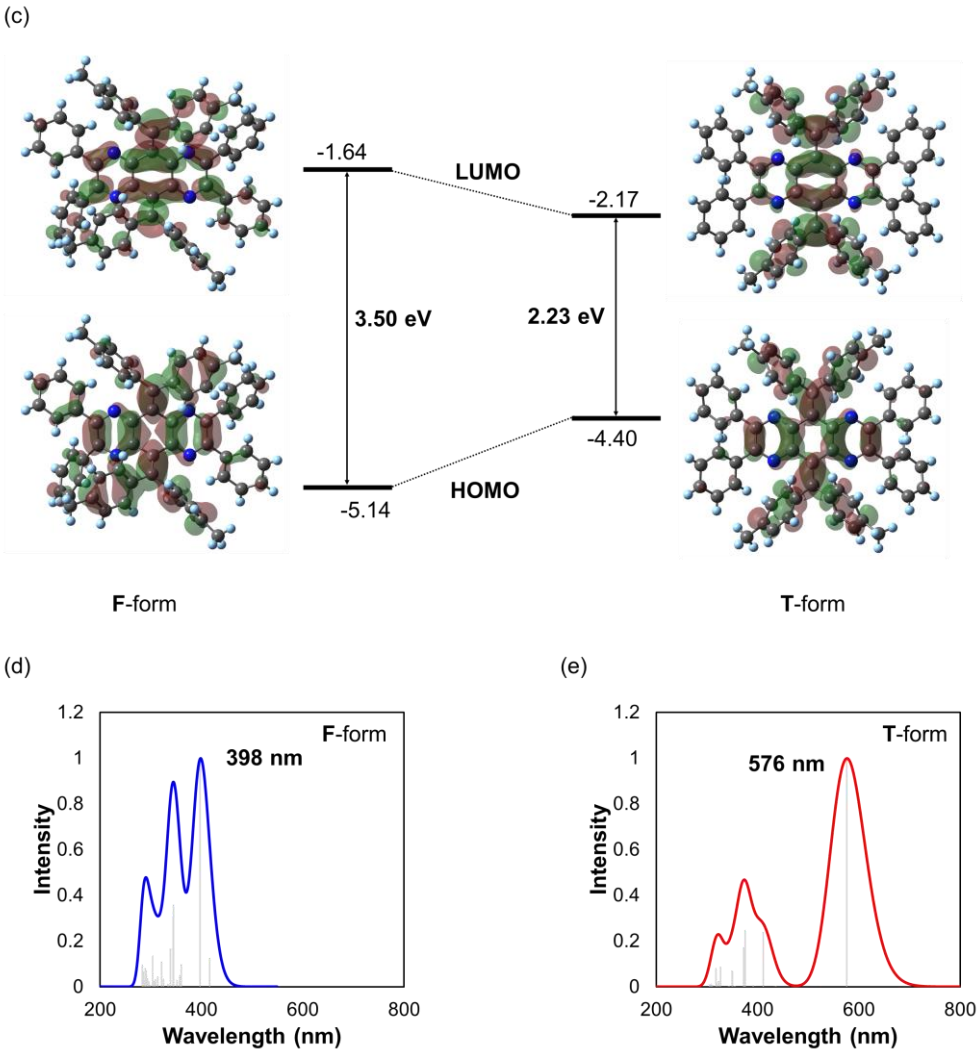

Figure 2-9. (c) HOMO and LUMO levels calculated by the DFT method (B3LYP/6-31G*). Simulated UV/Vis spectra of (d) **F**-form and (e) **T**-form obtained by TD-DFT calculations (B3LYP/6-31G*) based on the crystallographic coordinates.

To investigate the origin of their color, the author performed DFT calculations (B3LYP/6-31G*) using the obtained crystallographic coordinates, and the results indicated that the **T**-form has a higher HOMO and lower LUMO than the **F**-form, i.e., the electronic structures of these conformers are significantly different (Figure 2-9c). Actually, time-dependent (TD)-DFT calculations (B3LYP/6-31G*) predicted a ca. 180-nm difference in simulated absorption maxima between these conformers (398 nm for **F**-form and 576 nm for **T**-form), which well reproduces the color of each crystal (Figure 2-9d, e). On the other hand, the only X-ray structures obtained for the reference compounds **6** and **7** were folded (Figure 2-10). These results emphasize that both the nitrogen atoms and the *vic*-diphenyl groups introduced into the central AQD skeleton contribute to stabilization of the **T**-form.

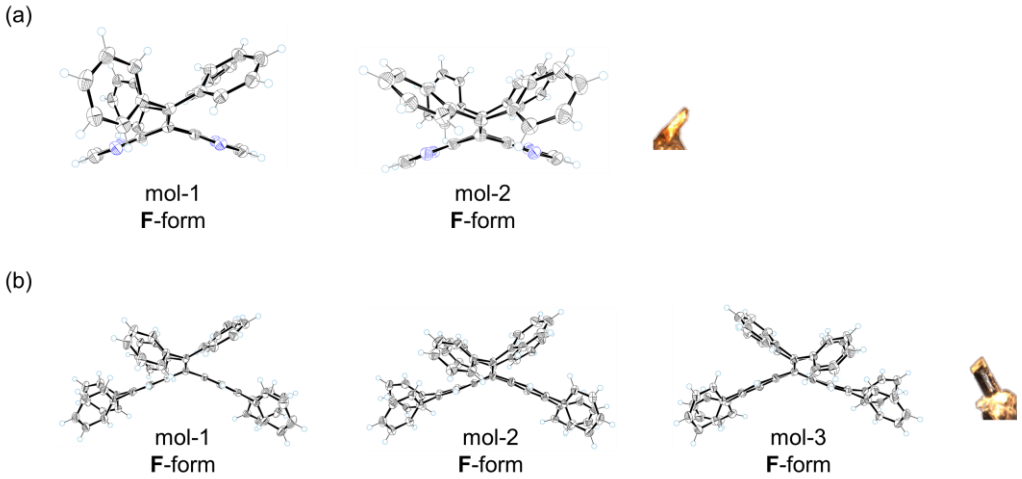

Figure 2-10. ORTEP drawings of (a) **6** [**F**-form (mol-1 and mol-2) without crystallization solvent (recrystallized from $CHCl_3$/hexane)], and (b) **7** [**F**-form (mol-1, mol-2, and mol-3) without crystallization solvent (recrystallized from CH_2Cl_2/hexane)]. The solvent molecules are omitted for clarity. Thermal ellipsoids are shown at the 50% probability level.

The most important finding is that the obtained crystal structures were not only the **F**- and **T**-forms but also several other conformations, which could not be classified as either of them. For orange-colored H_2O-solvated crystal and reddish-orange-colored CH_2Cl_2-solvated crystal of **2b**, the **P**-form with almost a normal planar geometry of the C=C double bond and the **TF**-form with an intermediary structure between **F**- and **T**-forms were observed, respectively (Figure 2-9b, Table 2-5).

Table 5. Structural parameters of **2b** obtained from X-ray structures (**F**-, **P**-, **TF**-, and **T**-forms) and from optimized structures (**F**-, and **T**-forms) calculated by the DFT method (B3LYP/6-31G*).

	C1-C2 [Å]	C5-C6 [Å]	C6-C7 [Å]	C10-C1 [Å]	C2-C5 [Å]	C7-C10 [Å]	C1-C11 [Å]	C6-C26 [Å]	θ [°]	φ [°]	χ [°]
F-form (Expt.)	1.4813(19)	1.483(2)	1.4870(19)	1.481(2)	1.410(2)	1.409(2)	1.357(2)	1.358(2)	29.91(8) 28.78(9)	8.89(7) 12.15(7)	35.86(11)
F-form (Calcd.)	*1.4869*	*1.4875*	-	-	*1.4202*	-	*1.3665*	-	*34.66*	*13.55* *13.55*	*40.79*
T-form (Expt.)	1.4650(12)	1.4636(17)	-	-	1.4158(15)	-	1.3898(15)	-	2.13(4)	32.77(5)	1.77(10)
T-form (Calcd.)	*1.4686*	*1.4686*	*1.4687*	*1.4686*	*1.4280*	-	*1.3900*	-	*3.92* *3.92*	*27.90*	*2.48*
P-form (Expt.)	1.475(6)	1.481(7)	1.479(6)	1.471(7)	1.408(6)	1.413(6)	1.370(6)	1.364(6)	13.0(3) 17.0(3)	15.0(2) 12.1(2)	17.5(4)
TF-form (Expt.)	1.481(4)	1.478(3)	1.467(4)	1.467(4)	1.411(4)	1.411(4)	1.370(4)	1.383(4)	21.34(15) 9.49(13)	17.64(13) 31.05(10)	17.66(18)

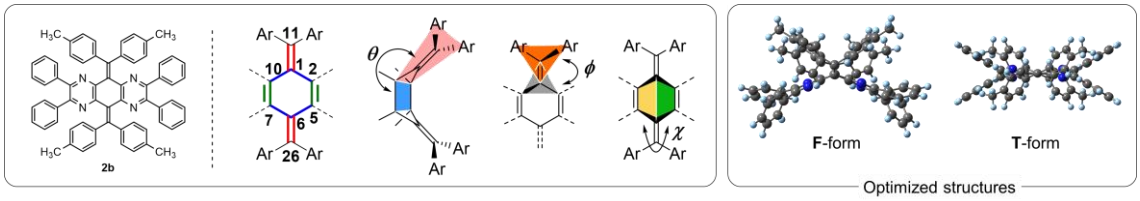

Furthermore, for other derivatives (e.g., phenyl derivative **2a**, fluorophenyl derivative **2c**, and chlorophenyl derivative **2d**), multiple conformations were observed in their crystals, regardless of the difference in the steric and electronic properties of the substituents on the aryl groups (Table 2-6, Figures 2-10, 11, 12 and 13).

Table 2-6. List of the single crystals of **2a**, **2b**, **2c**, and **2d** analyzed by X-ray in this study.

	Conformation	Color[b]	Shape	Solvate	Recrystallization solvent
2a (R = H)	**F**-form	Yellow	Plate	CH_2Cl_2	CH_2Cl_2/hexane
	F-form	Yellow	Plate	$CHCl_3$	$CHCl_3$/EtOH
	T-form	Red	Block	None	CH_2Cl_2/EtOH
2b (R = CH_3)	**F**-form	Yellow	Plate	2EtOH	EtOAc/EtOH
	P-form	Orange	Plate	H_2O	EtOAc/EtOH
	P-form	Orange	Plate	CH_2Cl_2	CH_2Cl_2/hexane
	P-form	Orange	Plate	$0.5CHCl_3$	$CHCl_3$/EtOH
	TF-form	Reddish-orange	Plate	$0.5CH_2Cl_2$	CH_2Cl_2/hexane
	TF-form	Reddish-orange	Block	0.5hexane	EtOAc/hexane
	TF-form	Reddish-orange	Plate	0.5EtOAc	EtOAc/EtOH
	TF-form	Reddish-orange	Plate	CH_2Cl_2	CH_2Cl_2/EtOH
	T-form	Red	Plate	None	EtOAc/hexane
2c (R = F)	**F**-form	Yellow	Block	EtOAc	EtOAc
	F-form	Yellow	Plate	$0.25CH_2Cl_2$	CH_2Cl_2/hexane
	F-form	Yellow	Plate	$1.25CH_2Cl_2$	CH_2Cl_2/EtOH
	F-form	Yellow	Plate	$2CHCl_3$	$CHCl_3$/EtOH
	F-form + semi-**P**-form[a]	Orange	Plate	H_2O	$CHCl_3$/hexane
	TP-form	Red	Needle	$CHCl_3$	$CHCl_3$/hexane
	TP-form[a]	Red	Needle	CH_2Cl_2	CH_2Cl_2/hexane
	TP-form[a]	Red	Needle	EtOH	EtOAc/EtOH
	TF-form	Reddish-orange	Plate	$CHCl_3$	$CHCl_3$/hexane
2d (R = Cl)	**P**-form[a]	Orange	Plate	$CHCl_3$	$CHCl_3$/EtOH
	P-form	Orange	Plate	CH_2Cl_2	CH_2Cl_2/hexane
	TF-form	Reddish-orange	Plate	$CHCl_3$	$CHCl_3$/hexane
	T-form	Red	Needle	None	$CHCl_3$/hexane

[a] In a crystal, there are two crystallographically independent molecules.

[b] Colors are determined visually.

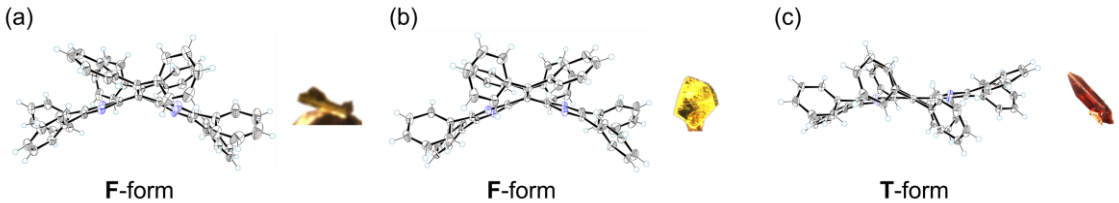

Figure 2-10. ORTEP drawings of **2a** [(a) **F**-form in CH_2Cl_2 solvate (recrystallized from CH_2Cl_2/hexane), (b) **F**-form in $CHCl_3$ solvate (recrystallized from $CHCl_3$/EtOH), and (c) **T**-form without crystallization solvent (recrystallized from CH_2Cl_2/EtOH)]. The solvent molecules are omitted for clarity. Thermal ellipsoids are shown at the 50% probability level.

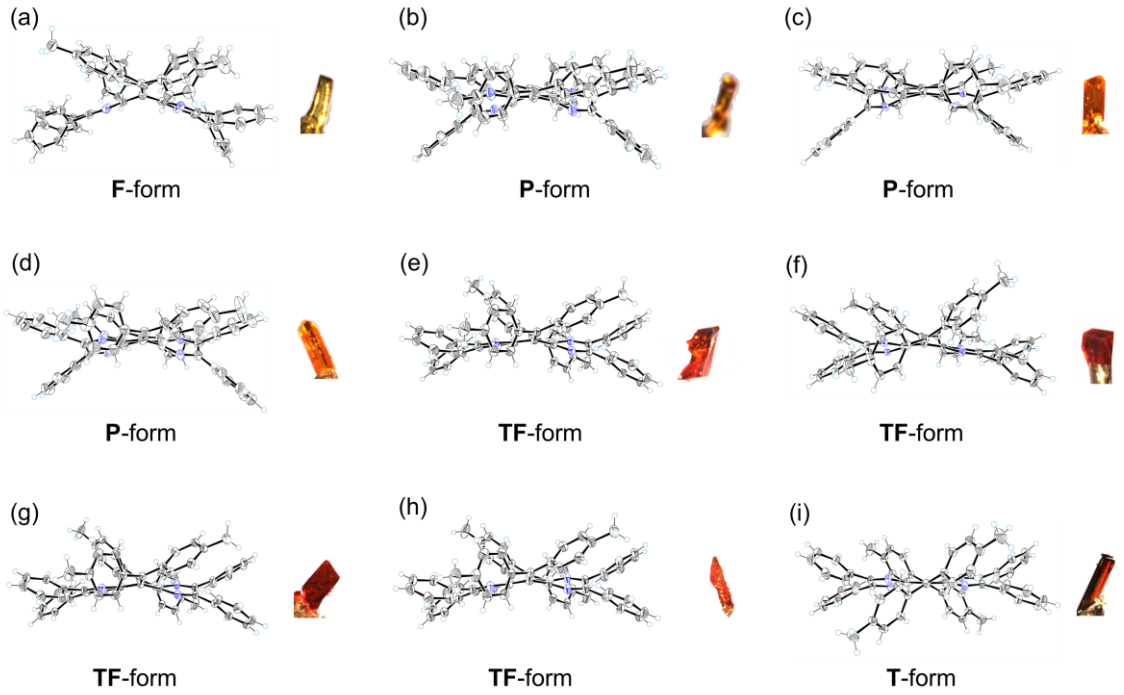

Figure 2-11. ORTEP drawings of **2b** [(a) **F**-form in 2EtOH solvate (recrystallized from EtOAc/EtOH), (b) **P**-form in H_2O solvate (recrystallized from EtOAc/EtOH), (c) **P**-form in CH_2Cl_2 solvate (recrystallized from CH_2Cl_2/hexane), (d) **P**-form in $0.5CHCl_3$ solvate (recrystallized from $CHCl_3$/EtOH), (e) **TF**-form in $0.5CH_2Cl_2$ solvate (recrystallized from CH_2Cl_2/hexane), (f) **TF**-form in 0.5hexane solvate (recrystallized from EtOAc/hexane), (g) **TF**-form in 0.5EtOAc solvate (recrystallized from EtOAc/EtOH), (h) **TF**-form in CH_2Cl_2 solvate (recrystallized from CH_2Cl_2/EtOH), and (i) **T**-form without crystallization solvent (recrystallized from EtOAc/hexane)]. The solvent molecules are omitted for clarity. Thermal ellipsoids are shown at the 50% probability level.

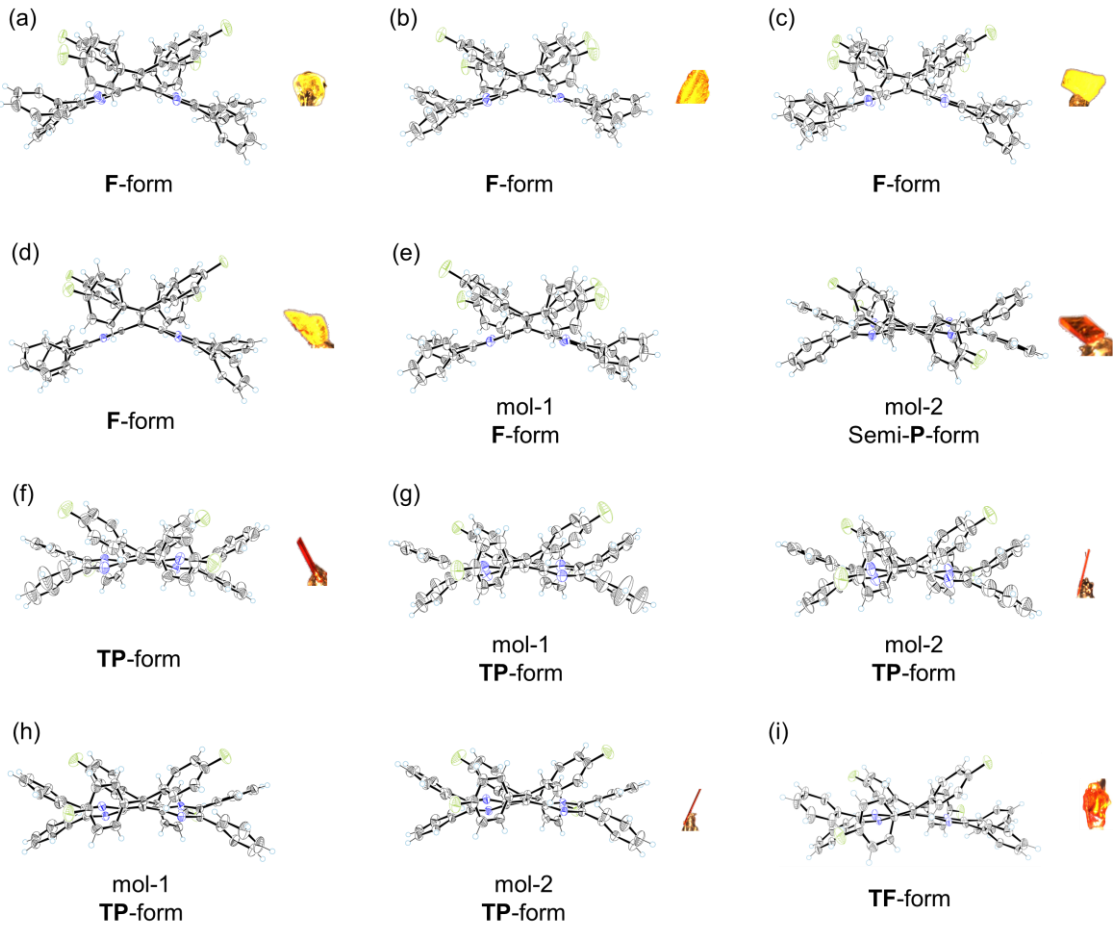

Figure 2-12. ORTEP drawings of **2c** [(a) **F**-form in EtOAc solvate (recrystallized from EtOAc), (b) **F**-form in $0.25CH_2Cl_2$ solvate (recrystallized from CH_2Cl_2/hexane) (c) **F**-form in $1.25CH_2Cl_2$ solvate (recrystallized from CH_2Cl_2/EtOH), (d) **F**-form in $2CHCl_3$ solvate (recrystallized from $CHCl_3$/EtOH), (e) **F**-form (mol-1) and semi-**P**-form (mol-2) in H_2O solvate (recrystallized from $CHCl_3$/hexane), (f) **TP**-form in $CHCl_3$ solvate (recrystallized from $CHCl_3$/hexane), (g) **TP**-form (mol-1 and mol-2) in CH_2Cl_2 solvate (recrystallized from CH_2Cl_2/hexane), (h) **TP**-form (mol-1 and mol-2) in EtOH solvate (recrystallized from EtOAc/EtOH), and (i) **TF**-form in $CHCl_3$ solvate (recrystallized from $CHCl_3$/hexane)]. The solvent molecules are omitted for clarity. Thermal ellipsoids are shown at the 50% probability level.

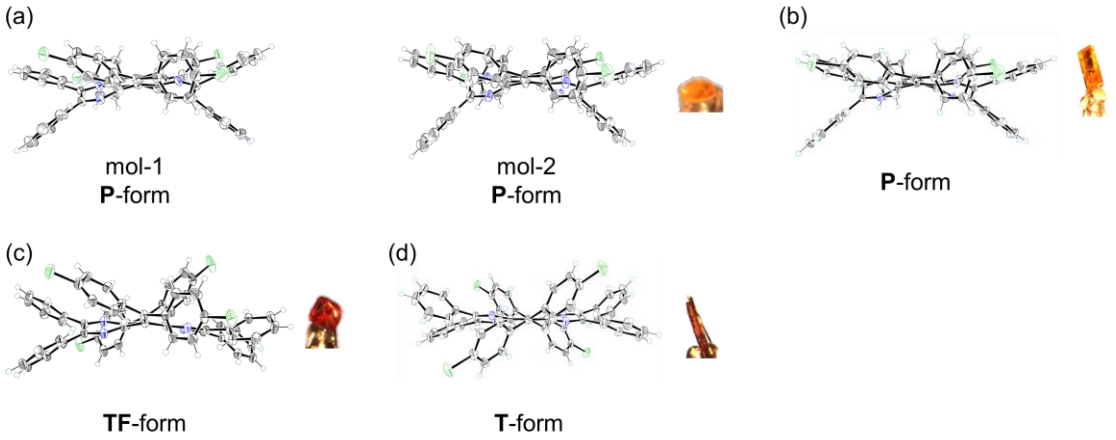

Figure 2-13. ORTEP drawings of **2d** [(a) **P**-form (mol-1 and mol-2) $CHCl_3$ in solvate (recrystallized from $CHCl_3$/EtOH), (b) **P**-form in CH_2Cl_2 solvate (recrystallized from CH_2Cl_2/hexane), (c) **TF**-form in $CHCl_3$ solvate (recrystallized from $CHCl_3$/hexane), and (d) **T**-form without crystallization solvent (recrystallized from $CHCl_3$/hexane)]. The solvent molecules are omitted for clarity. Thermal ellipsoids are shown at the 50% probability level.

Since these intermediate structures are considered to be unstable in solution, their abundance ratio is generally zero. In fact, optimization from the obtained crystallographic coordinates as the initial structure yielded the **T**-form, which is the most stable structure. Even though there are some intermolecular contacts between molecules in each crystal, no significant interactions were observed to stabilize the specific conformation (Figures 2-14, 15, 16 and 17). Based on these results, the intermediate structures observed in the pseudopolymorphs are stabilized by solvent molecules filling a void while forming a crystal. Accordingly, we clarified that multiple intermediate structures as well as the **F**- and **T**-forms can arise in the same molecule for MAE-type OCEs. Although a few examples have been described previously, where multiple conformations with a slight difference in dihedral angles were observed in (pseudo)polymorphs,[57,58] this study is quite unique because a drastic change in color has been achieved for multiple conformers with a large difference in molecular geometry such as the **F**-, **T**-, **P**-, and **TF**-forms. Thus, specific electronic properties such as HOMO-LUMO gaps based on the structures of the pseudopolymorphs can be determined, whereas dynamically averaged physical properties are generally observed in solution (Table 2-7, Figure 2-18).

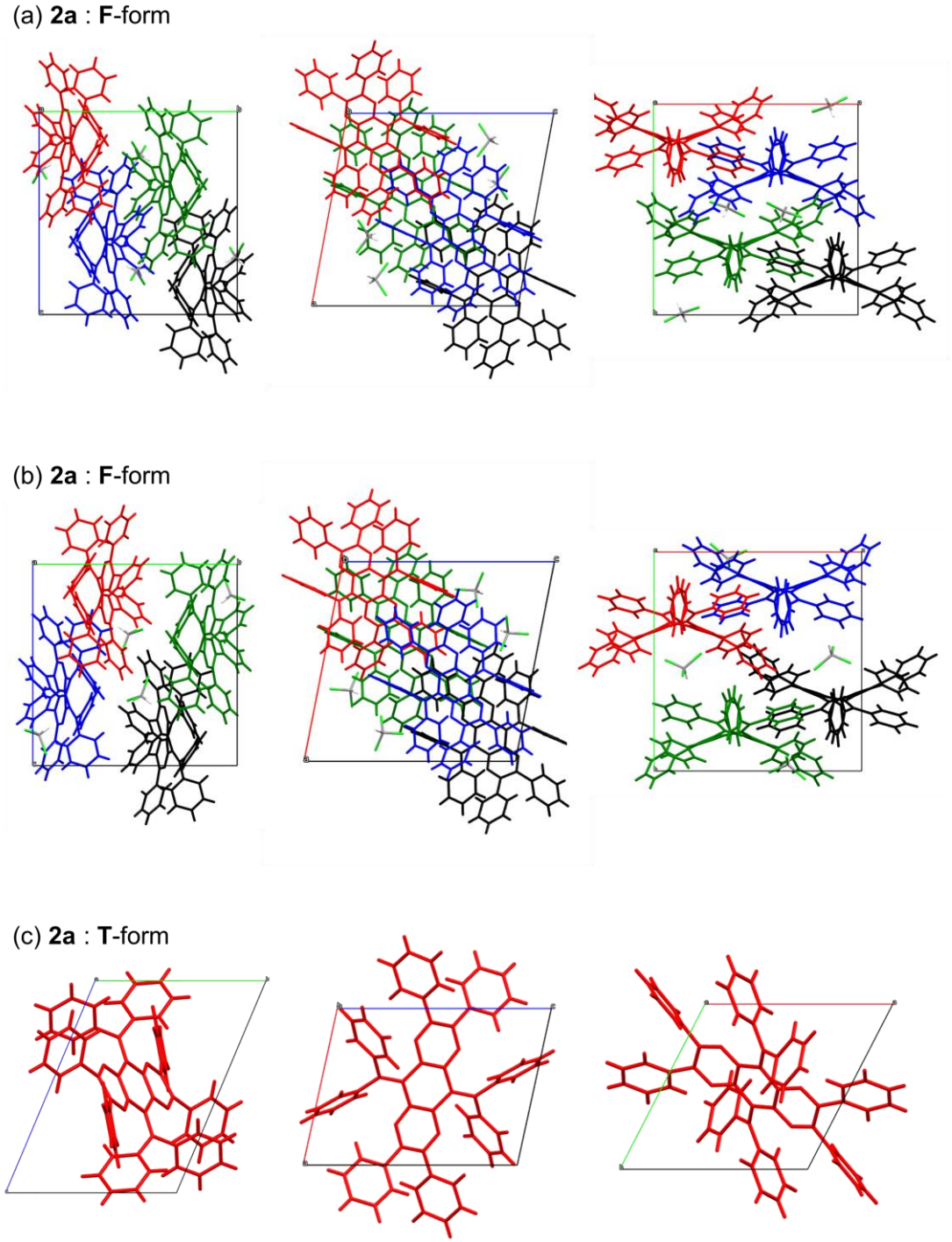

Figure 2-14. Molecular packing in the crystals of **2a** along the *a*-, *b*-, and *c*-axis (left, middle, and right, respectively) [(a) **F**-form in CH_2Cl_2 solvate (recrystallized from CH_2Cl_2/hexane), (b) **F**-form in $CHCl_3$ solvate (recrystallized from $CHCl_3$/EtOH), and (c) **T**-form without crystallization solvent (recrystallized from CH_2Cl_2/EtOH)].

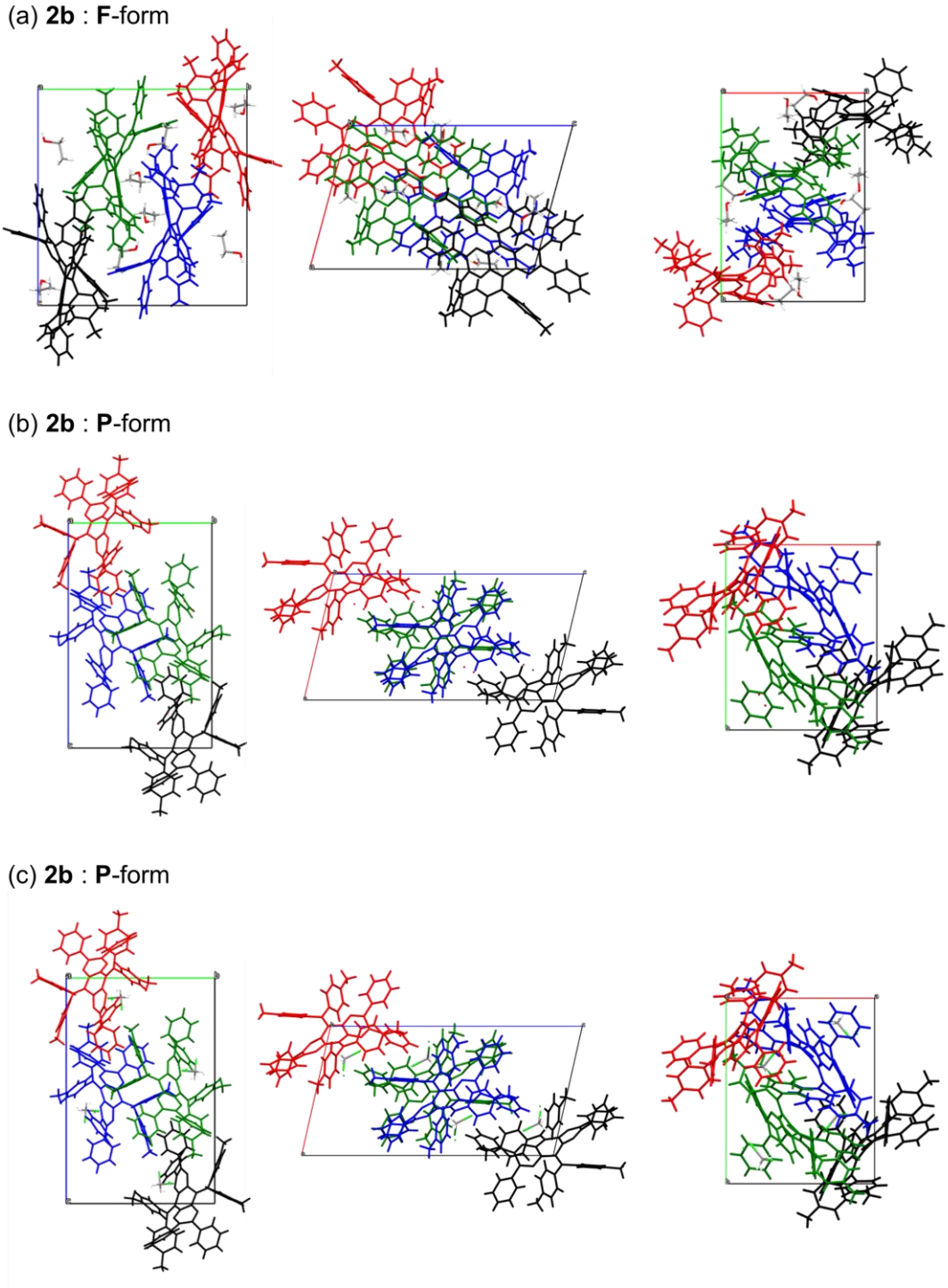

Figure 2-15. Molecular packing in the crystals of **2b** along the *a*-, *b*-, and *c*-axis (left, middle, and right, respectively) [(a) **F**-form in 2EtOH solvate (recrystallized from EtOAc/EtOH), (b) **P**-form in H_2O solvate (recrystallized from EtOAc/EtOH), and (c) **P**-form in CH_2Cl_2 solvate (recrystallized from CH_2Cl_2/hexane)].

(d) **2b** : **P**-form

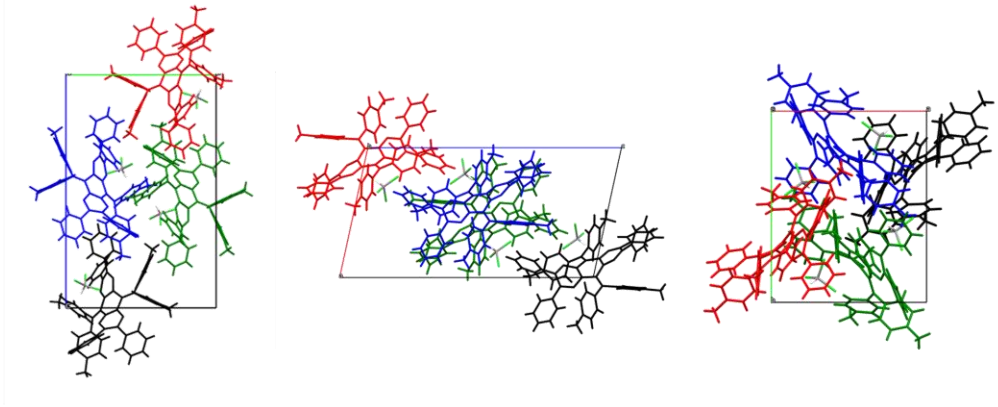

(e) **2b** : **TF**-form

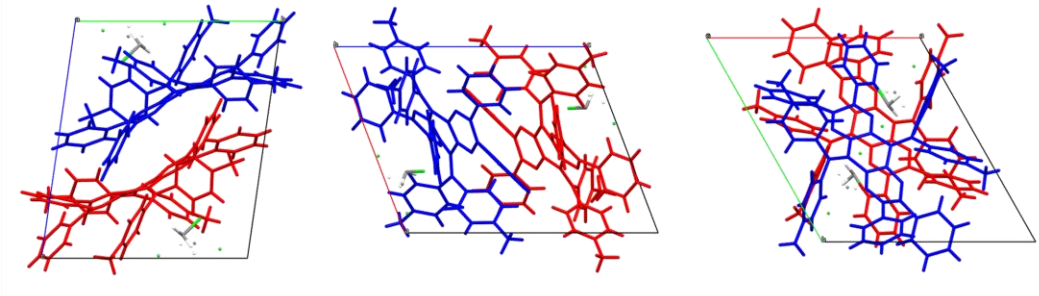

(f) **2b** : **TF**-form

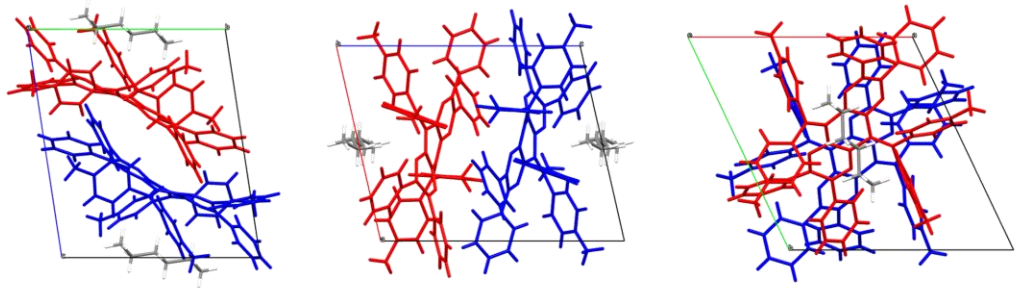

Figure 2-15. Molecular packing in the crystals of **2b** along the *a*-, *b*-, and *c*-axis (left, middle, and right, respectively) [(d) **P**-form in 0.5$CHCl_3$ solvate (recrystallized from $CHCl_3$/EtOH), (e) **TF**-form in 0.5CH_2Cl_2 solvate (recrystallized from CH_2Cl_2/hexane), and (f) **TF**-form in 0.5hexane solvate (recrystallized from EtOAc/hexane)].

(g) **2b** : **TF**-form

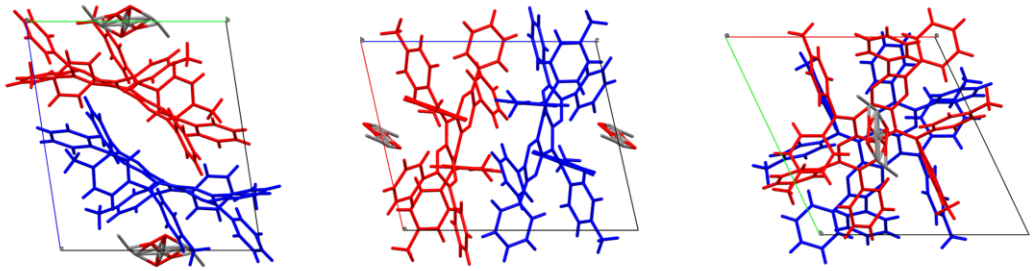

(h) **2b** : **TF**-form

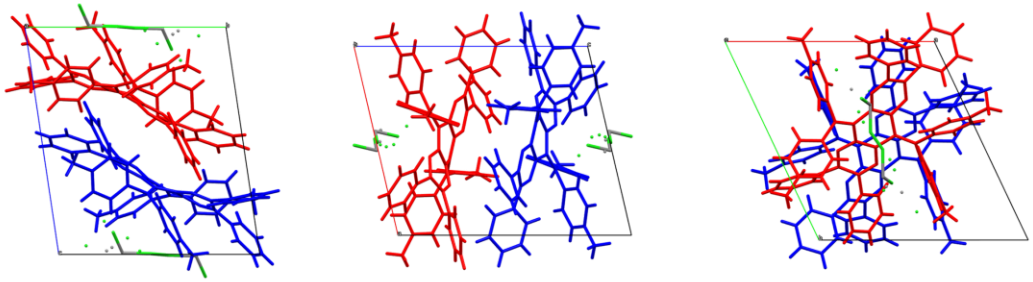

(i) **2b** : **T**-form

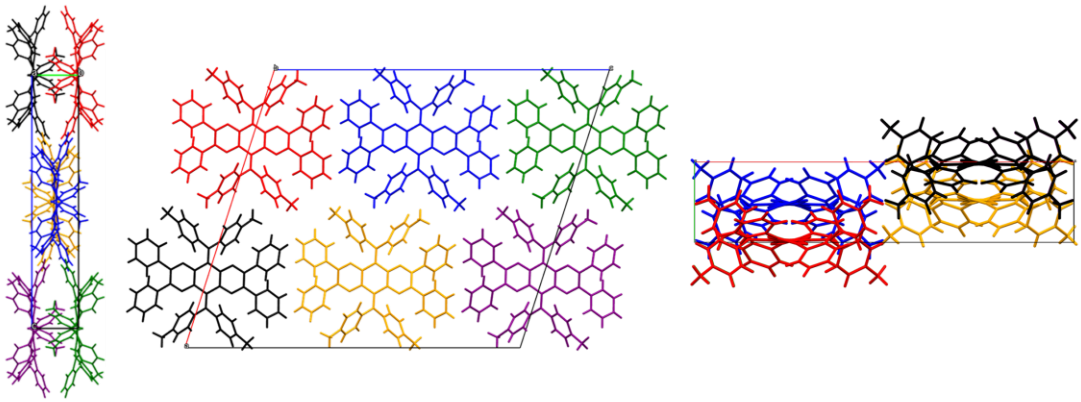

Figure 2-15. Molecular packing in the crystals of **2b** along the *a*-, *b*-, and *c*-axis (left, middle, and right, respectively) [(g) **TF**-form in 0.5EtOAc solvate (recrystallized from EtOAc/EtOH), (h) **TF**-form in CH_2Cl_2 solvate (recrystallized from CH_2Cl_2/EtOH), and (i) **T**-form without crystallization solvent (recrystallized from EtOAc/hexane)].

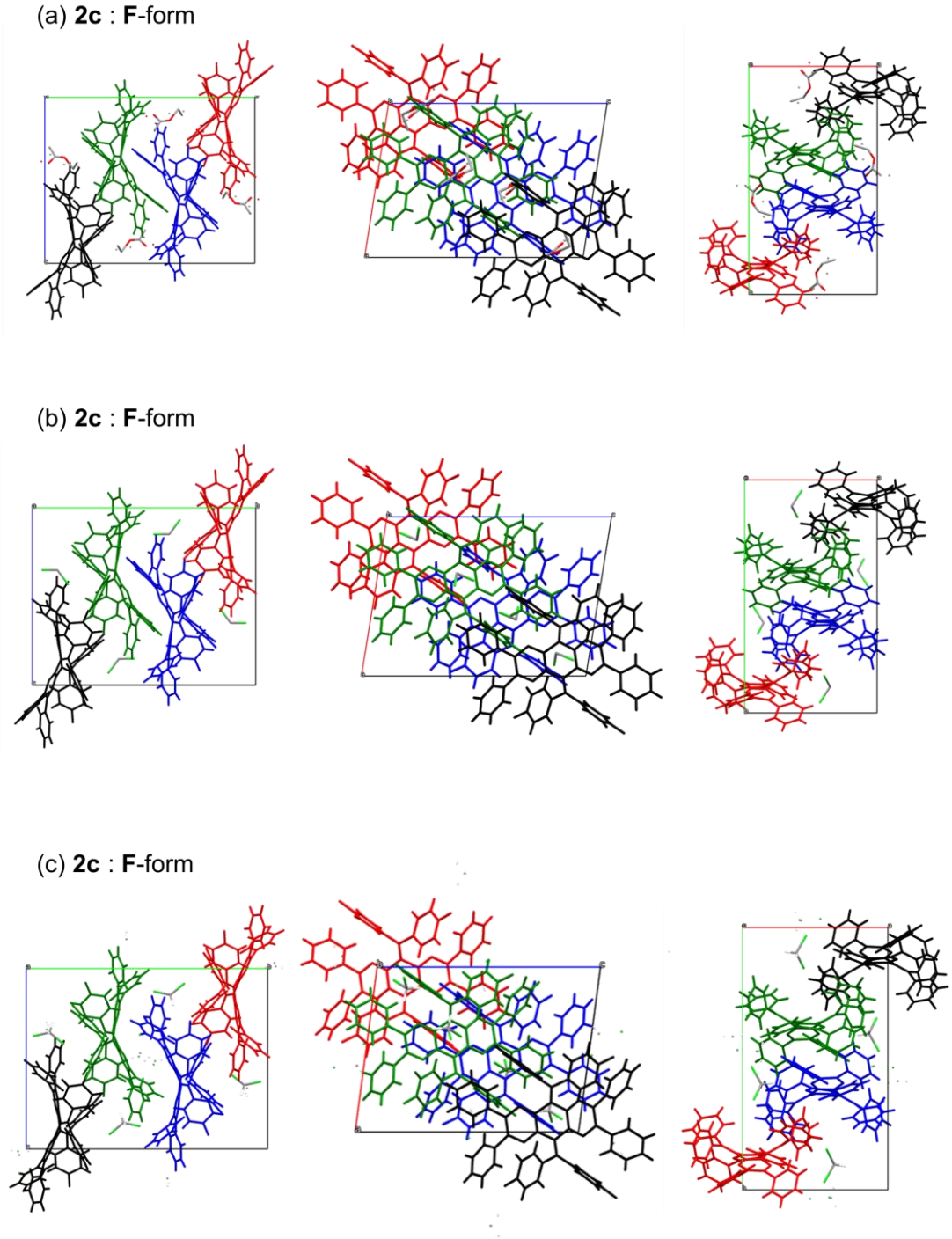

Figure 2-16. Molecular packing in the crystals of **2c** along the *a*-, *b*-, and *c*-axis (left, middle, and right, respectively) [(a) **F**-form in EtOAc solvate (recrystallized from EtOAc), (b) **F**-form in $0.25CH_2Cl_2$ solvate (recrystallized from CH_2Cl_2/hexane), and (c) **F**-form in $1.25CH_2Cl_2$ solvate (recrystallized from CH_2Cl_2/EtOH)].

(d) **2c** : **F**-form

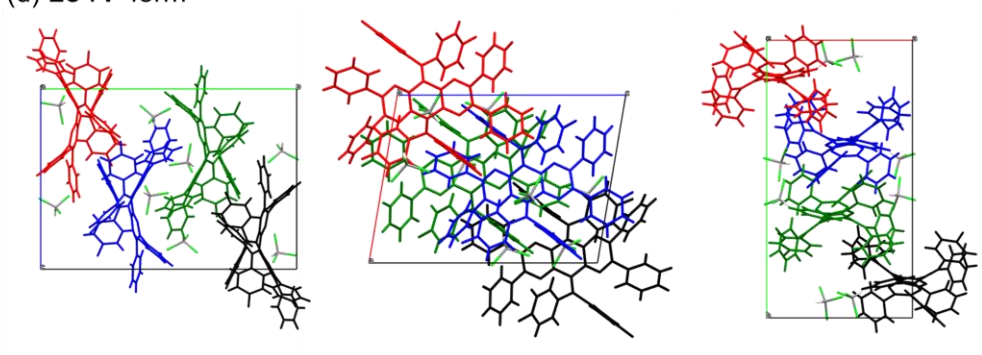

(e) **2c** : **F**-form + semi-**P**-form

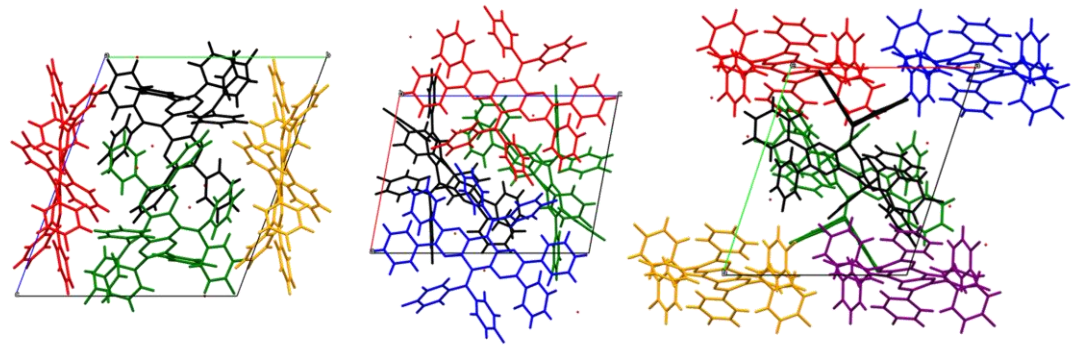

(f) **2c** : **TP**-form

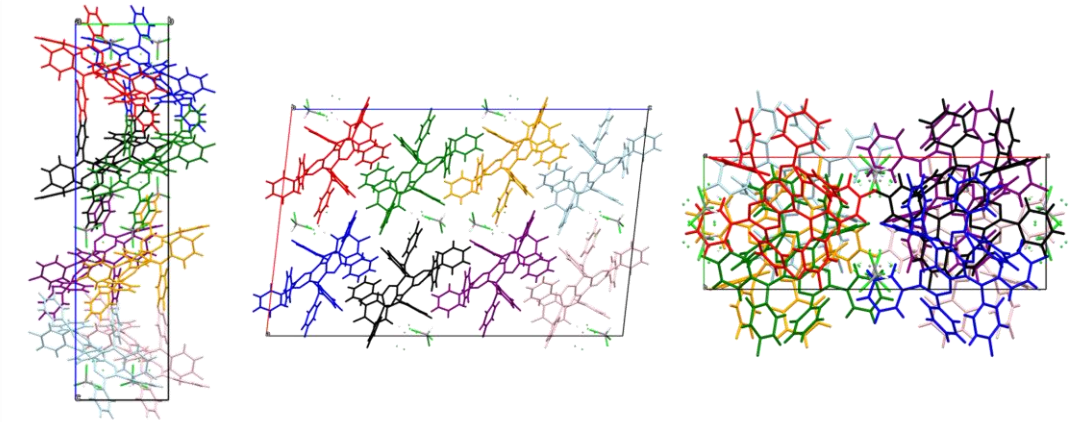

Figure 2-16. Molecular packing in the crystals of **2c** along the *a*-, *b*-, and *c*-axis (left, middle, and right, respectively) [(d) **F**-form in $2CHCl_3$ solvate (recrystallized from $CHCl_3$/EtOH), (e) **F**-form (mol-1) and semi-**P**-form (mol-2) in H_2O solvate (recrystallized from $CHCl_3$/hexane), and (f) **TP**-form in $CHCl_3$ solvate (recrystallized from $CHCl_3$/hexane)].

(g) **2c** : **TP**-form

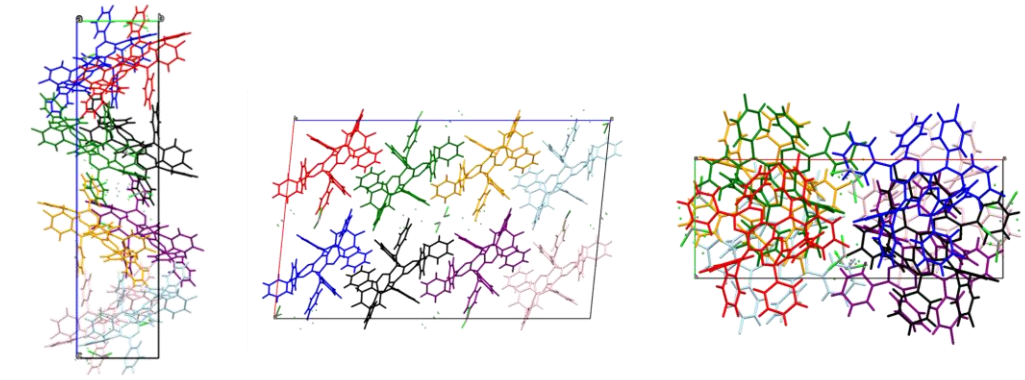

(h) **2c** : **TP**-form

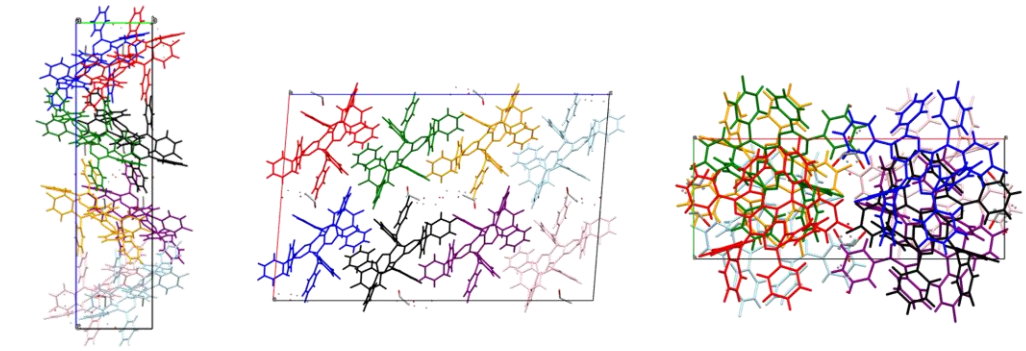

(i) **2c** : **TF**-form

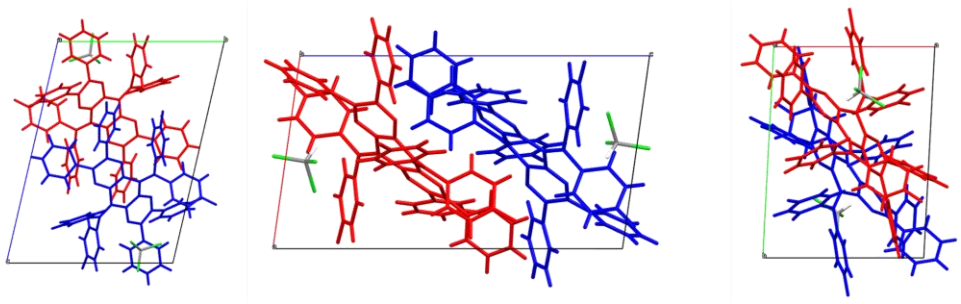

Figure 2-16. Molecular packing in the crystals of **2c** along the *a*-, *b*-, and *c*-axis (left, middle, and right, respectively) [(g) **TP**-form (mol-1 and mol-2) in CH_2Cl_2 solvate (recrystallized from CH_2Cl_2/hexane), (h) **TP**-form (mol-1 and mol-2) in EtOH solvate (recrystallized from EtOAc/EtOH), and (i) **TF**-form in $CHCl_3$ solvate (recrystallized from $CHCl_3$/hexane)].

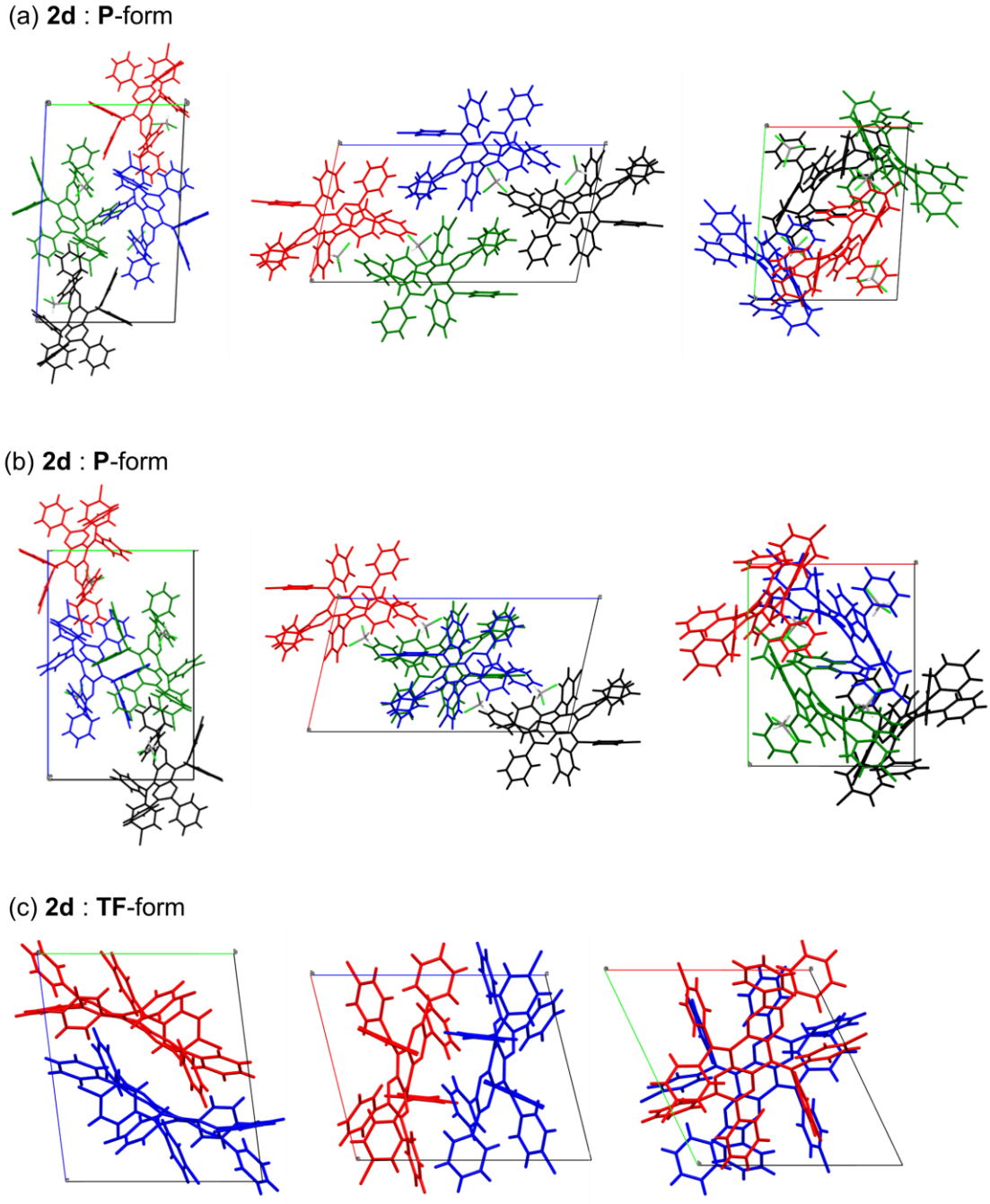

Figure 2-17. Molecular packing in the crystals of **2d** along the *a*-, *b*-, and *c*-axis (left, middle, and right, respectively) [(a) **P**-form (mol-1 and mol-2), $CHCl_3$ in solvate (recrystallized from $CHCl_3$/EtOH), (b) **P**-form in CH_2Cl_2 solvate (recrystallized from CH_2Cl_2/hexane), and (c) **TF**-form in $CHCl_3$ solvate (recrystallized from $CHCl_3$/hexane),].

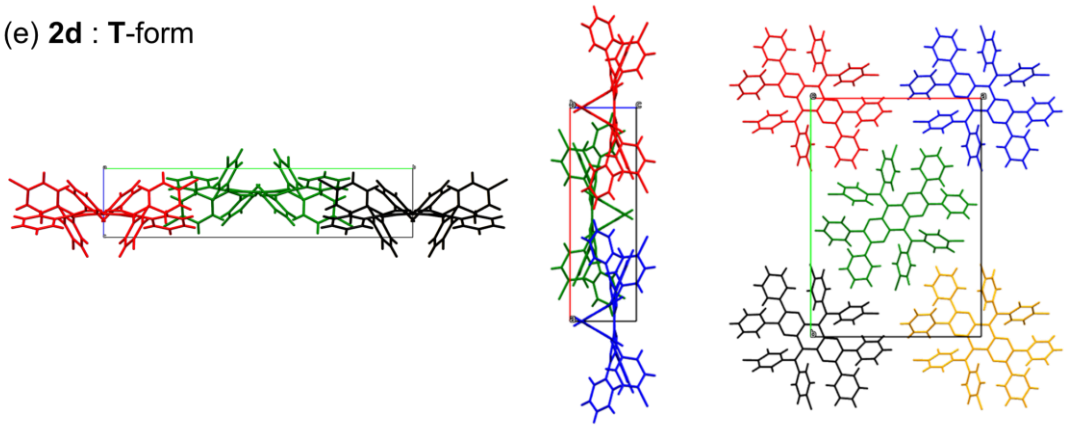

Figure 2-17. Molecular packing in the crystals of **2d** along the *a*-, *b*-, and *c*-axis (left, middle, and right, respectively) [(e) **T**-form without crystallization solvent (recrystallized from $CHCl_3$/hexane)].

Table 2-7. Estimated electronic properties of **2b** (**F**-, **P**-, **TF**-, and **T**-forms). All data were calculated using the (TD-)DFT method (B3LYP/6-31G*).

	E^{DFT}_{HOMO} [eV]	E^{DFT}_{LUMO} [eV]	$E^{DFT}_{LUMO-HOMO}$ [eV]	λ^{TD-DFT}_{max} [nm]
F-form	-5.14	-1.64	3.50	398
T-form	-4.40	-2.17	2.23	576
P-form	-4.79	-1.91	2.88	464
TF-form	-4.68	-2.04	2.64	48

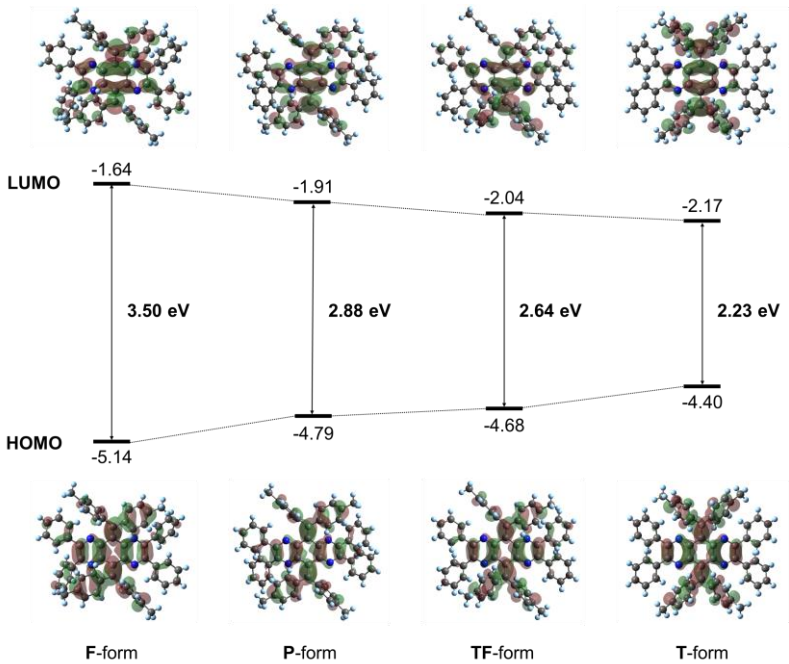

Figure 2-18. HOMO and LUMO levels calculated by the DFT method (B3LYP/6-31G*) based on the crystallographic coordinates of **2b**.

2-2-5. Luminescence Properties

Notably, luminescence of the crystals is strongly affected by the difference in the conformations of N4AQD derivatives **2**. Figure 2-19b shows the emission spectra of crystals for fluorophenyl derivative **2c** under excitation at 380 nm. The emission wavelength changed depending on the conformations of the crystals (λ_{em} = 548 nm and Φ_{em} = 4.4% for **F**-form, λ_{em} = 672 nm and Φ_{em} = 2.8% for twisted-planar (**TP**) form, λ_{em} = 690 nm and Φ_{em} = 2.2% for **TF**-form, λ_{em} = 650 nm and Φ_{em} = 2.4% for **F**-form + semi-**P**-form), and a red shift of the emission maximum was observed as the dihedral angle φ increased [φ = 15.06(9)°, 14.27(9)° for **F**-form, mol-1 : φ = 20.8(3)°, 24.5(3)°, mol-2 : φ = 23.5(3)°, 27.0(3)° for **TP**-form, φ = 26.23(11)°, 18.66(11)° for **TF**-form, mol-1: φ = 7.84(9)°, 14.81(8)°,mol-2: φ = 23.06(9)° for **F**-form + semi-**P**-form] (Figure 2-19a).

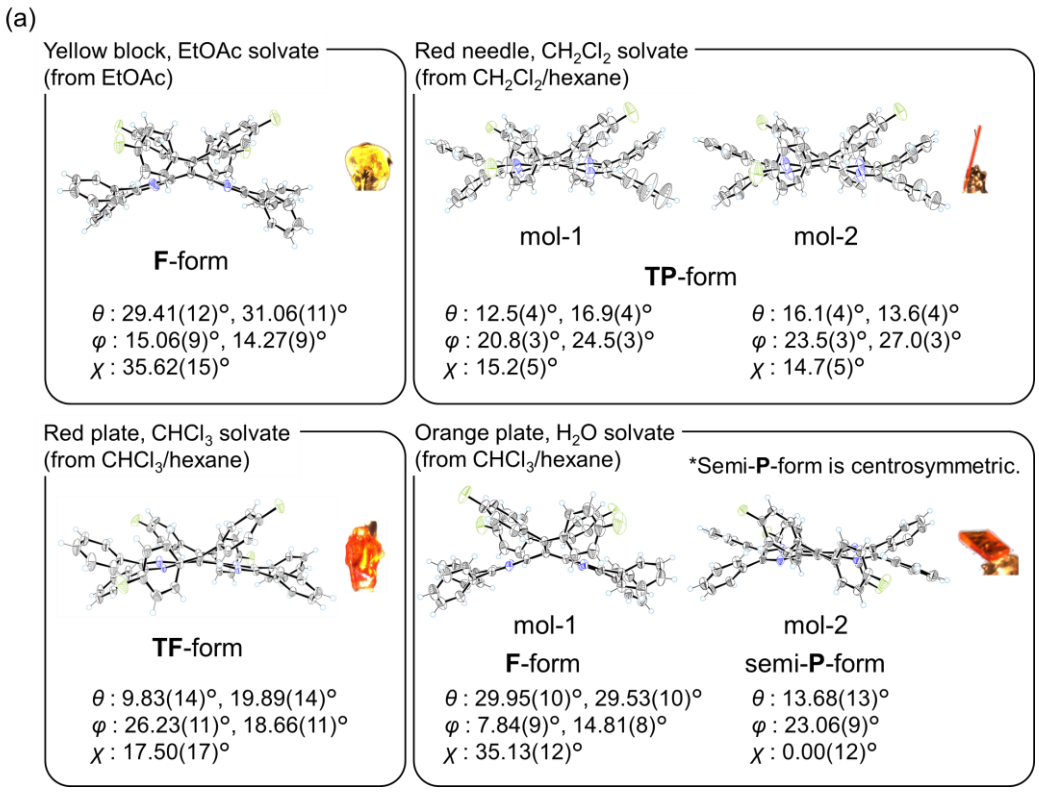

Figure 2-19. (a) ORTEP drawings of **2c** [**F**-form in EtOAc solvate (recrystallized from EtOAc), **TP**-form in CH_2Cl_2 solvate (recrystallized from CH_2Cl_2/hexane), **TF**-form in $CHCl_3$ solvate (recrystallized from $CHCl_3$/hexane), and those in which the **F**- and semi-**P**-forms exist as two crystallographically independent molecules in H_2O solvate (recrystallized from $CHCl_3$/hexane)]. Each of them was classified by the difference in dihedral angle θ, φ, and χ) for which emission spectra were measured. The solvent molecules are omitted for clarity.

(b)

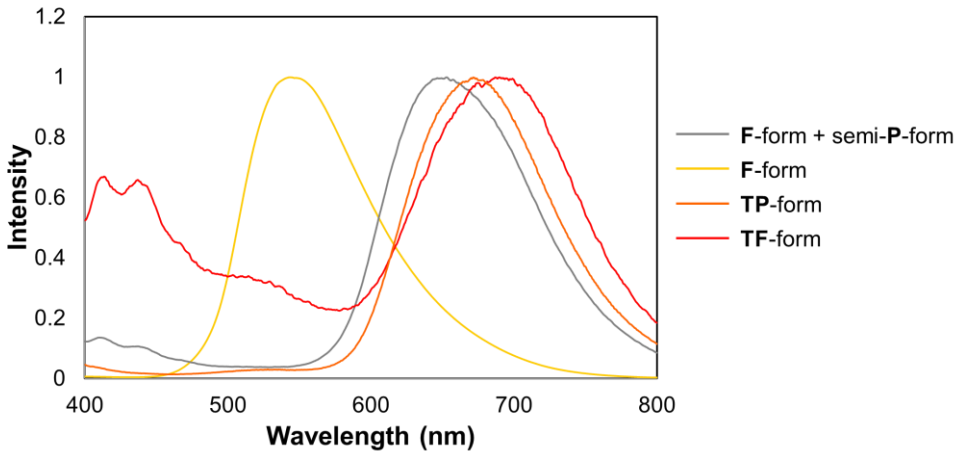

(c)

	λ_{em} [nm]	τ_1 [ns]	τ_2 [ns]	τ_{av} [ns]	Φ_{em} [%]	λ_{ex} [nm]
F-form	548	0.6	2.3	2.3	4.4	467
TP-form	672	0.6	2.5	2.4	2.8	512
TF-form	690	0.1	2.2	2.2	2.2	546
F-form + semi-**P**-form	650	0.4	3.1	3.1	2.4	503

Figure 2-19. (b) Emission spectra and (c) luminescence properties of each conformation of **2c** were recorded in the solid state. All crystals are excited at 380 nm. Emission lifetimes are detected at the longer emission maximum. λ_{ex} is the value of the peak in the excitation spectra of **2c**.

Interestingly, there is about a 140-nm difference in the emission maximum between the **F**-form and **TF**-form, even though they are the same molecule, whereas there is an 80-nm difference in the excitation spectra between them (Figures 2-19c and 2-20). In addition, the emission of the **TF**-form extends to the red to near-infrared (NIR) region even in the neutral species. Long-wavelength emission of **2c** is unlikely to be in a polarized form[59,60] but is solely due to the twisted conformation of the molecule. In the case of **2a**, **2b**, and **2d**, the emission spectra also depend on the conformation in the crystal. Additionally, no significant intermolecular interactions which can be enough to influence their photophysical properties were observed in the pseudopolymorphs of N_4AQD derivatives **2** (Figures 2-14, 15, 16 and 17), though the change in the color of luminescence in ordinary polymorphs is mostly due to changes in intermolecular interactions.[61–63] These results indicate that the changes in the color of luminescence in N_4AQDs **2** depend only on the conformations of the molecules in the crystals, and a shift of the emission maximum up to 140 nm was accomplished by dynamic structural changes based on the flexibility of molecules.

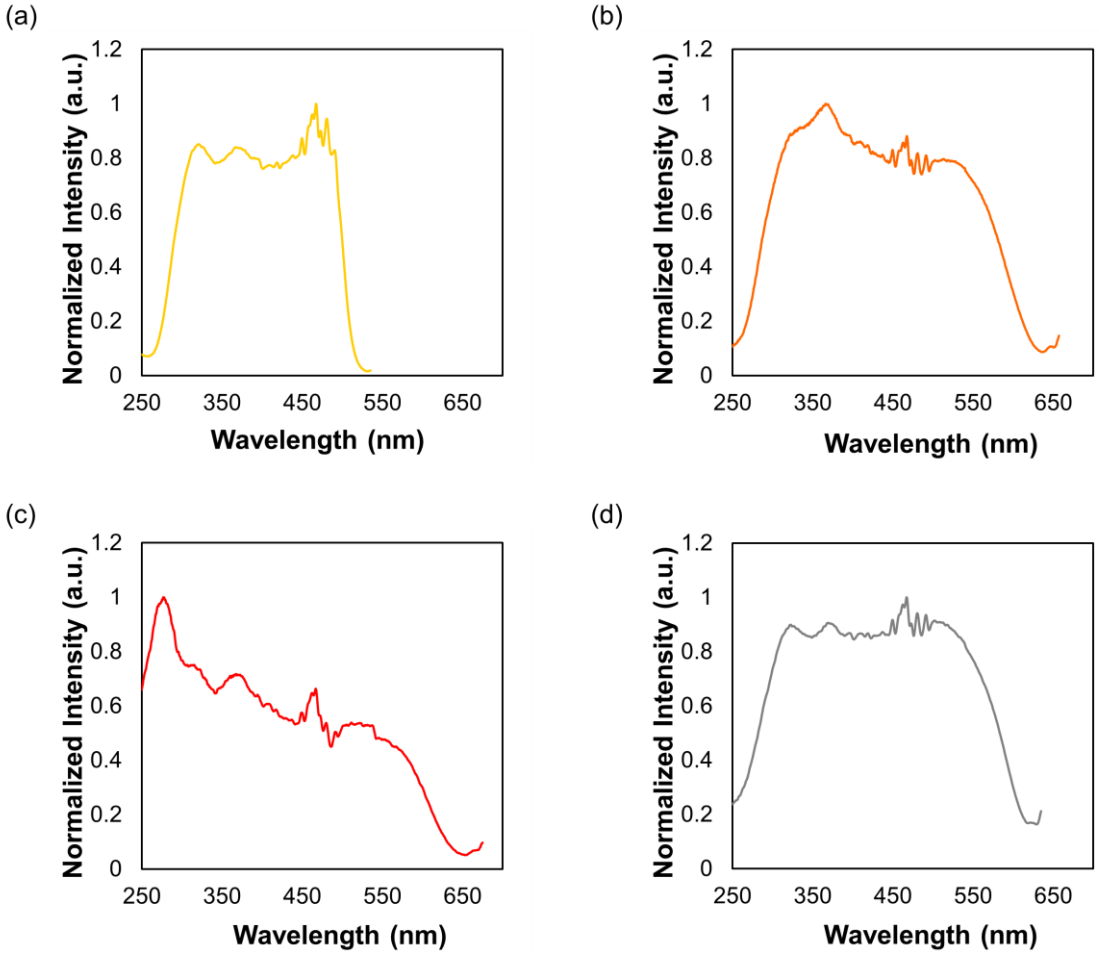

Figure 2-20. Excitation spectra of (a) **F**-form, (b) **TP**-form, (c) **TF**-form, and (d) **F**-form + semi-**P**-form of **2c**. All measurements were detected at the longer emission maximum.

2-2-6. Mechanochromic Behavior

The author then investigated a stimuli-responsive behavior of crystals for **2c**. Actually, color changes were observed under visible and UV light of fluorophenyl derivative **2c** when the yellow EtOAc-solvated crystals (**F**-form) were ground in an agate mortar and pestle, as shown in Figure 2-21a. After yellow crystals with a folded conformation were ground, the color of the samples became reddish-orange (Figure 2-22) and the maximum emission wavelength shifted from λ_{em} = 544 nm to λ_{em} = 636 nm (Figure 2-21b and Table 2-8), suggesting that a twisted conformation is produced. Furthermore, the original crystal with yellow emission (λ_{em} = 559 nm) can be recovered by dissolving the ground powder with EtOAc followed by drying (Figure 2-21b), which indicates that the HOMO-LUMO gap can be modulated based on the conformations by being exposed to external stimuli. To investigate the origin of the change in the photophysical properties upon mechanical stimulation, powder X-ray diffraction (PXRD) analyses were conducted for each solid-state sample of **2c**.

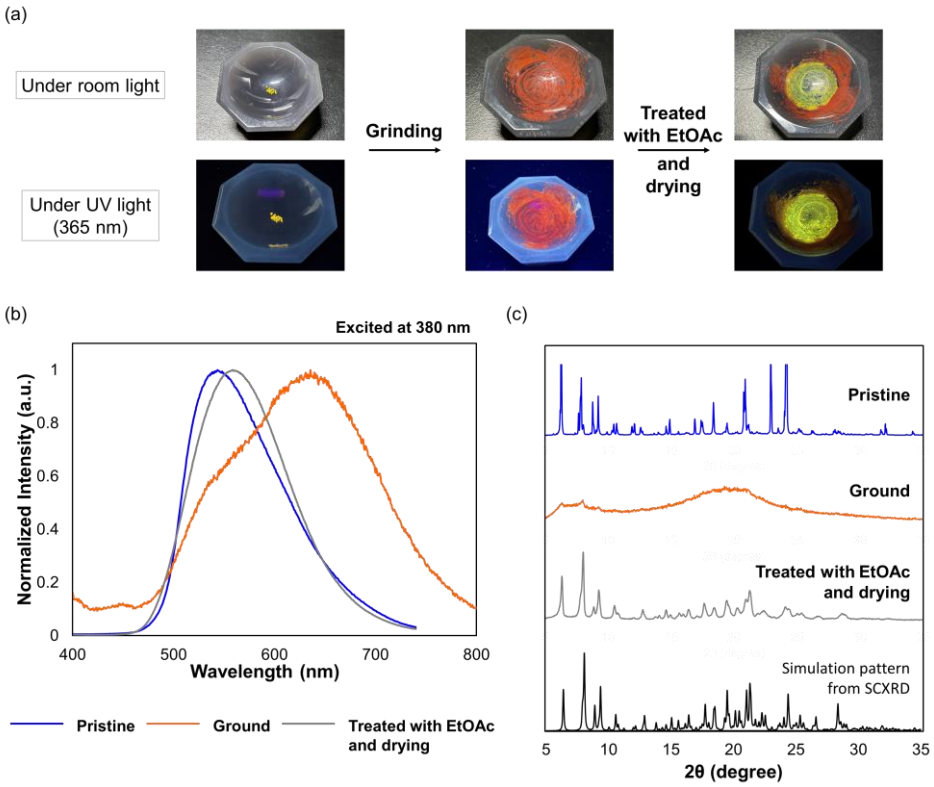

Figure 2-21. (a) Photographs of **2c** under room light (upper) and UV light (lower) in various states. (b) Changes in the emission spectrum for **2c**. (c) Changes in the PXRD pattern of **2c**. The black line is the simulation pattern from single-crystal X-ray diffraction (SCXRD).

Table 2-8. Luminescence properties of each state of **2c** were recorded in the solid state. All samples are excited at 380 nm. Emission lifetimes are detected at the longer emission maximum.

	λ_{em} [nm]	τ_1 [ns]	τ_2 [ns]	τ_{av} [ns]	Φ_{em} [%]
Pristine	544	0.901	2.491	1.810	5.9
Ground	636	0.311	1.303	0.674	1.0
Treated with EtOAc and drying	559	0.498	1.233	1.067	2.8

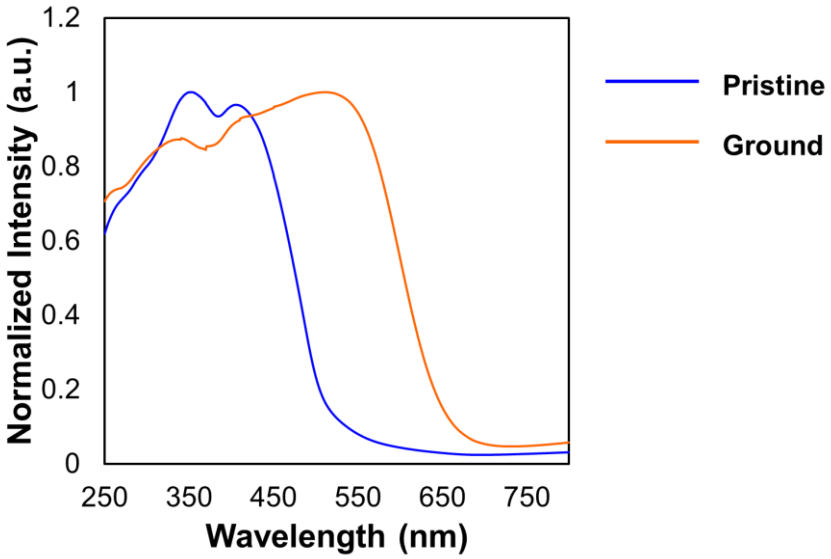

Figure 2-22. Diffuse reflectance spectra of **2c**.

As shown in Figure 2-21c, since the PXRD pattern of the ground sample (orange line) has no sharp peaks, a phase transition from crystal to amorphous occurred upon grinding the pristine crystal. As a result, the metastable **F**-form could no longer be maintained in an amorphous state, and thus the more stable twisted conformation appeared. Next, the sharp diffraction pattern was regenerated by treating the sample with EtOAc followed by drying (Figure 2-21c, from the orange line to the gray line), which demonstrates that **2c** exhibits mechanochromism in the ground and excited states based on the crystal-to-amorphous phase transition. This phenomenon was realized due to the "flexibility" granted to the MAE-type OCE, i.e., not only the reduction of steric hindrance by the introduction of nitrogen atoms into the central framework but also the introduction of *vic*-diphenyl groups on the fused pyrazine rings are important for creating multiple conformations with tunable photophysical properties.

2-3. Conclusion

In summary, the author has designed and synthesized four kinds of tetraaza AQD derivative **2** with moderately reduced steric hindrance in the overcrowded fjord region with the introduction of *vic*-diphenyl groups. The author succeeded in observing not only the **F**- and **T**-forms but also many other conformers, e.g., **P**-form, **TF**-form, and **TP**-form, in pseudopolymorphs of **2**, and this is the first demonstration of such multiple conformations for MAE-type OCEs. In addition, the author demonstrated that the HOMO/LUMO levels can be modulated by the conformations in crystals. Thus, the changes in color tone and emission of the crystals were accounted for by the difference in the electronic configurations of the conformers. It is particularly significant that the formation of twisted conformations with long-wavelength absorption/NIR-emission were achieved without the involvement of charge-separation states. This study has realized the control of absorption and luminescence properties derived from conformational changes, which is a very rare phenomenon in organic molecules, and revealed the potential value of novel sensor materials composed of simple but flexible organic molecule exhibiting an unprecedented gradual change in color.

2-4. Experimental Section

2-4-1. General

All reactions were carried out under an argon atmosphere. All commercially available compounds were used without further purification unless otherwise indicated. Dry toluene was obtained by distillation from CaH_2 prior to use. Column chromatography was performed on silica gel 60N (KANTO KAGAKU, spherical neutral) of particle size 40-50 μm or Wakogel® 60N (neutral) of particle size 38-100 μm. ^1H and ^{13}C NMR spectra were recorded on a BRUKER Ascend^{TM} 400 (^1H/400 MHz and ^{13}C/100 MHz) spectrometer. IR spectra were measured on a Shimadzu IRAffinity-1S spectrophotometer using the attenuated total reflection (ATR) mode. Mass spectra were recorded on a JMS-T100GCV spectrometer in FD mode by Dr. Eri Fukushi and Mr. Yusuke Takata (GC-MS & NMR Laboratory, Research Faculty of Agriculture, Hokkaido University). Melting points were measured on a Stanford Research Systems OptiMelt MPA100 and are uncorrected. UV/Vis-NIR spectra were recorded on a Hitachi U-2910 spectrophotometer. UV/Vis diffuse reflectance measurements were recorded using a JASCO V-770 spectrometer (JASCO) with an integration sphere. A JASCO FP-8500 fluorescence spectrometer was used to collect excitation and emission spectra at room temperature. The absolute photoluminescence quantum yields (Φ_F) were calculated using the C9920-02 absolute photoluminescence quantum yields measurement system (Hamamatsu photonics). Time-resolved photoluminescence lifetimes were measured using a time-correlated single-photon counting lifetime spectroscopy system, Quantaurus-Tau C11367-02 (Hamamatsu photonics). PXRD data were collected at room temperature using a Rigaku SmartLab system (Rigaku) diffractometer with a copper K-alpha source. Redox potentials (E^{ox} and E^{red}) were measured on a BAS ALS-600A by cyclic voltammetry in dry DMF containing 0.1 M Bu_4NBF_4 as a supporting electrolyte. All of the values shown in the text are in E/V vs. SCE measured at the scan rate of 0.1 V s^{-1}. Pt electrodes were used as the working (disk) and counter electrodes. The working electrode was polished using a water suspension of aluminum oxide (0.05 μm) before use. DFT calculations were performed with the Gaussian 16W program package.[64] The geometries of the compounds were optimized by using the B3LYP method in combination with the 6-31G* basis set unless otherwise indicated.

2-4-2. Preparations

2,3,6,7-Tetraphenyl-1,4,5,8-tetraaza-9,10-anthraquinone (9)

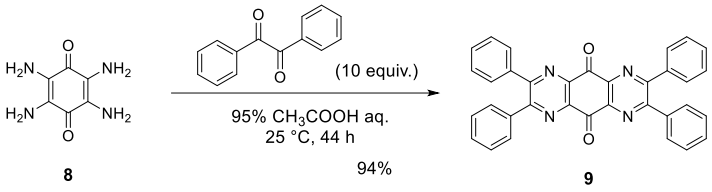

8 9

A mixture of 2,3,5,6-tetraamino-1,4-benzoquinone **8**[55] (1.26 g, 7.50 mmol) and benzil (15.8 g, 75.0 mmol) in 95% CH_3COOH aq. (263 mL) was stirred at 25 ℃ for 44 h. Then, the precipitates were collected by filtration, washed with water and EtOH, and dried *in vacuo* to give a **9** (3.63 g) as a yellow powder in 94% yield.

^{1}H NMR data were identical to those in literature.[65]

11,11,12,12-Tetrabromo-2,3,6,7-tetraphenyl-1,4,5,8-tetraaza-9,10-anthraquinodimethane (10)

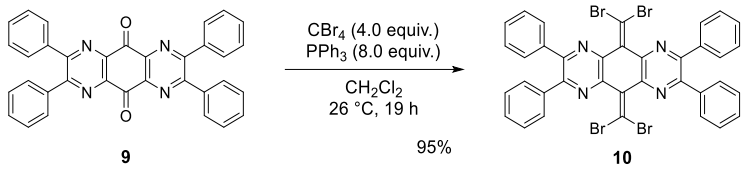

9 10

A mixture of CBr_4 (82.65 g, 8.00 mmol) and PPh_3 (4.20 g, 16.0 mmol) in dry CH_2Cl_2 (20 mL) was stirred at 26 ℃ for 1 h, and then 2,3,6,7-tetraphenyl-1,4,5,8-tetraaza-9,10-anthraquinone **9** (1.03 g, 2.00 mmol) was added to the mixture at 0 ℃. After warming to 26 ℃, the mixture was stirred at 26 ℃ for 19 h. After diluting with water, the reaction mixture was extracted with CH_2Cl_2 three times. The combined organic layers were washed with water and brine, and dried over anhydrous $MgSO_4$. After filtration, the solvent was concentrated under reduced pressure. The crude product was washed with CH_2Cl_2 until the filtrate becomes colorless, and the residue was dried *in vacuo* to give **10** (1.48 g) as a white powder in 89 %. The resulting filtrate was concentrated under reduced pressure, and purified by column chromatography on silica gel (CH_2Cl_2) to give **10** (101 mg) as a white powder in 6% yield (total 1.58 g, 95%).

^{1}H NMR data were identical to those in literature.[56]

2,3,6,7,11,11,12,12-Octaphenyl-1,4,5,8-tetraaza-9,10-anthraquinodimethane (2a)

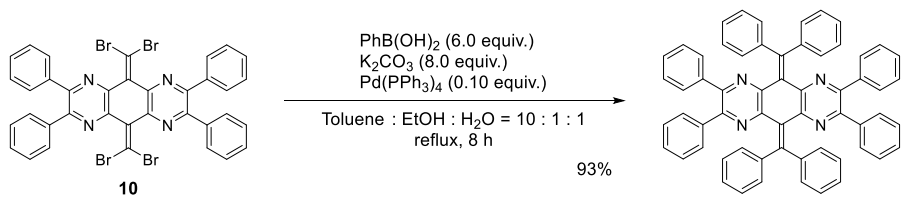

10 2a

A mixture of 11,11,12,12-tetrabromo-2,3,6,7-tetraphenyl-1,4,5,8-tetraaza-9,10-anthraquinodimethane **10** (108 mg, 130 μmol), phenylboronic acid (95.7 mg, 785 μmol), K_2CO_3 (144 mg, 1.04 mmol) and $Pd(PPh_3)_4$ (15.6 mg, 13.5 μmol) in a mixture of toluene (6 mL), EtOH (0.6 mL) and water (0.6 mL) was stirred at 120 ℃ for 8 h. After cooling to 26 ℃, the reaction mixture was extracted with EtOAc three times. The combined organic layers were washed with water and brine, and dried over anhydrous $MgSO_4$. After filtration, the solvent was concentrated under reduced pressure. The crude product was purified by column chromatography on silica gel (hexane/EtOAc = 10) to give **2a** (99.0 mg) as a red solid in 93% yield.

^{1}H NMR data were identical to those in literature.[56]

11,11,12,12-Tetrakis(4-methylphenyl)-2,3,6,7-tetraphenyl-1,4,5,8-tetraaza-9,10-anthraquinodimethane (2b)

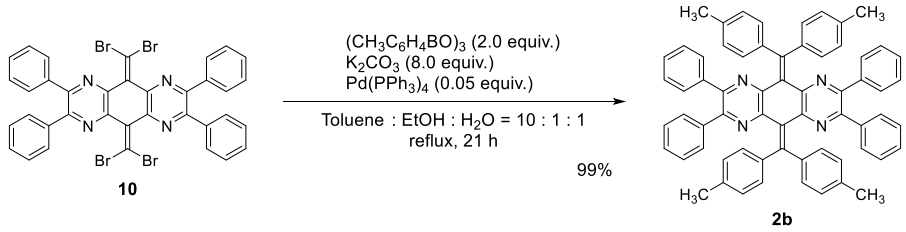

A mixture of 11,11,12,12-tetrabromo-2,3,6,7-tetraphenyl-1,4,5,8-tetraaza-9,10-anthraquinodimethane **10** (828 mg, 1.00 mmol), tris(4-methylphenyl)boroxine (708 mg, 2.00 mmol), K_2CO_3 (1.11 g, 8.00 mmol) and $Pd(PPh_3)_4$ (57.8 mg, 50.0 μmol) in a mixture of toluene (10 mL), EtOH (1 mL) and water (1 mL) was stirred at 120 ℃ for 21 h. After cooling to 25 ℃, the reaction mixture was extracted with CH_2Cl_2 three times. The combined organic layers were washed with water and brine, and dried over anhydrous Na_2SO_4. After filtration, the solvent was concentrated under reduced pressure. The crude product was purified by column chromatography on silica gel (hexane/CH_2Cl_2 = 1) to give **2b** (863 mg) as a wine red solid in 99% yield.

Mp: 254.3-260.1 ℃ (decomp); ^{1}H NMR (400 MHz, $CDCl_3$): δ/ppm 7.19-7.10 (20H, m), 7.04 (8H, t, J = 7.6 Hz), 6.71 (8H, d, J = 7.6 Hz), 2.45 (12H, s); ^{13}C NMR (100 MHz, $CDCl_3$): δ/ppm 151.64, 146.06, 144.01, 141.39, 137.83, 137.68, 131.30, 129.82, 128.70, 128.30, 127.61, 127.56, 21.43; IR (ATR): ν/cm^{-1} 3056, 3021, 2917, 2862, 1603, 1572, 1517, 1503, 1478, 1450, 1400, 1372, 1310, 1266, 1205, 1180, 1115, 1090, 1075, 1032, 1005, 922, 881, 845, 818, 808, 791, 783, 773, 761, 735, 693, 952, 639, 617, 601, 581, 544, 502, 487, 479; LR-MS(FD) m/z (%): 873.34 (28), 873.33 (73), 872.33 (M^+, bp); HR-MS (FD) Calcd. for $C_{64}H_{48}N_4$: 872.38790; Found: 872.38885.

11,11,12,12-Tetrakis(4-fluorophenyl)-2,3,6,7-tetraphenyl-1,4,5,8-tetraaza-9,10-anthraquinodimethane (2c)

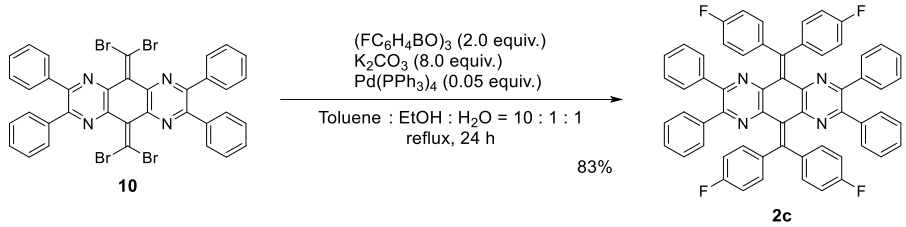

A mixture of 11,11,12,12-tetrabromo-2,3,6,7-tetraphenyl-1,4,5,8-tetraaza-9,10-anthraquinodimethane **10** (828 mg, 1.00 mmol), tris(4-fluorophenyl)boroxine (732 mg, 2.00 mmol), K_2CO_3 (1.11 g, 8.00 mmol) and $Pd(PPh_3)_4$ (57.8 mg, 50.0 μmol) in a mixture of toluene (10 mL), EtOH (1 mL) and water (1 mL) was stirred at 120 ℃ for 24 h. After cooling to 24 ℃, the reaction mixture was extracted with CH_2Cl_2 three times. The combined organic layers were washed with water and brine, and dried over anhydrous Na_2SO_4. After filtration, the solvent was concentrated under reduced pressure. The crude product was purified by column chromatography on silica gel (hexane/CH_2Cl_2 = 1) to give **2c** (742 mg) as a yellow solid in 83% yield.

Mp: 274.4-280.0 ℃ (decomp); ^{1}H NMR (400 MHz, $CDCl_3$): δ/ppm 7.25-7.18 (12H, m), 7.12 (8H, t, J = 7.8 Hz), 7.04 (8H, t, J = 8.7 Hz), 6.82 (8H, d, J = 7.8 Hz); ^{13}C NMR (100 MHz, $CDCl_3$): δ/ppm 162.68 (C, d, $J_{C\text{-}F}$ = 247 Hz), 149.11, 147.24, 141.86, 141.26 (C, d, $J_{C\text{-}F}$ = 4.0 Hz), 137.54, 132.81 (C, d, $J_{C\text{-}F}$ = 8.0 Hz), 129.55, 128.75, 128.54, 127.86, 115.04 (C, d, $J_{C\text{-}F}$ = 21 Hz); IR (ATR): ν/cm^{-1} 3052, 3041, 3000, 2982, 1731, 1596, 1500, 1452, 1398, 1368, 1314, 1296, 1221, 1174, 1153, 1116, 1101, 1074, 1049, 1030, 1015, 940, 920, 882, 830, 810, 797, 788, 772, 762, 756, 741, 695, 638, 633, 619, 611, 594, 587, 573, 543, 525, 508, 501, 471; LR-MS(FD) m/z (%): 890.24 (25), 889.24 (69), 888.24 (M^+, bp); HR-MS (FD) Calcd. for $C_{60}H_{36}F_4N_4$: 888.28761; Found: 888.28895.

11,11,12,12-Tetrakis(4-chlorophenyl)-2,3,6,7-tetraphenyl-1,4,5,8-tetraaza-9,10-anthraquinodimethane (2d)

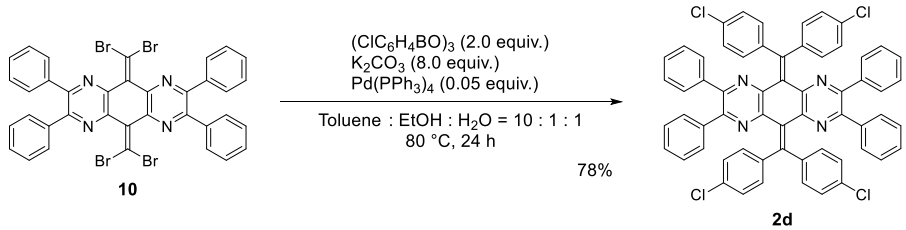

A mixture of 11,11,12,12-tetrabromo-2,3,6,7-tetraphenyl-1,4,5,8-tetraaza-9,10-anthraquinodimethane **10** (828 mg, 1.00 mmol), tris(4-chlorophenyl)boroxine (830 mg, 2.00 mmol), K_2CO_3 (1.11 g, 8.00 mmol) and $Pd(PPh_3)_4$ (57.8 mg, 50.0 μmol) in a mixture of toluene (10 mL), EtOH (1 mL) and water (1 mL) was stirred at 80 ℃ for 24 h. After cooling to 24 ℃, the reaction mixture was extracted with CH_2Cl_2 three times. The combined organic layers were washed with water

and brine, and dried over anhydrous Na_2SO_4. After filtration, the solvent was concentrated under reduced pressure. The crude product was purified by column chromatography on silica gel (hexane/CH_2Cl_2 = 1) to give **d** (740 mg) as an orange solid in 78% yield.

Mp: 300.1-303.2 ℃ (decomp); ^{1}H NMR (400 MHz, $CDCl_3$): δ/ppm 7.33 (8H, d, *J* = 8.4 Hz), 7.22 (4H, d, *J* = 7.4 Hz), 7.16 (8H, d, *J* = 8.4 Hz), 7.13 (8H, t, *J* = 7.4 Hz), 6.75 (8H, d, *J* = 7.4 Hz); ^{13}C NMR (100 MHz, $CDCl_3$): δ/ppm 148.65, 147.47, 144.43, 141.20, 137.29, 133.92, 132.21, 129.54, 128.86, 128.64, 128.44, 127.92; IR (ATR): *ν*/cm^{-1} 3058, 3046, 2986, 2955, 2926, 1583, 1520, 1484, 1451, 1396, 1374, 1269, 1205, 1179, 1118, 1085, 1030, 1012, 1004, 920, 880, 843, 827, 810, 804, 791, 785, 766, 734, 692, 665, 642, 631, 617, 598, 545, 530, 521, 507, 490, 454; LR-MS(FD) *m*/*z* (%): 959.12 (10), 958.12(23), 957.12 (37), 956.12 (66), 955.12 (67), 954.12 (bp), 953.13 (49), 952.12 (M^+, 70); HR-MS (FD) Calcd. for $C_{60}H_{36}Cl_4N_4$: 952.16941; Found: 952.16801.

11,11,12,12-Tetrabromo-9,10-anthraquinodimethane (4)

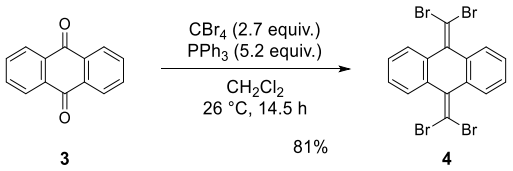

3 4

To a solution of 9,10-anthraquinone **3** (4.18 g, 20.1 mmol) and CBr_4 (17.7 g, 53.4 mmol) in dry CH_2Cl_2 (300 mL) was added PPh_3 (27.4 g, 104 mmol) at 26 ℃. After stirring at 26 ℃ for 14.5 h, the precipitates were filtered and washed with CH_2Cl_2. The resulting filtrate was extracted with CH_2Cl_2 three times. The combined organic layers were washed with water and brine, and dried over anhydrous $MgSO_4$. After filtration, the solvent was concentrated under reduced pressure. The crude product was purified by column chromatography on silica gel (hexane) to give **4** (8.44 g) as a colorless crystal in 81% yield.

^{1}H NMR data were identical to those in literature.[47]

11,11,12,12-Tetraphenyl-9,10-anthraquinodimethane (1)

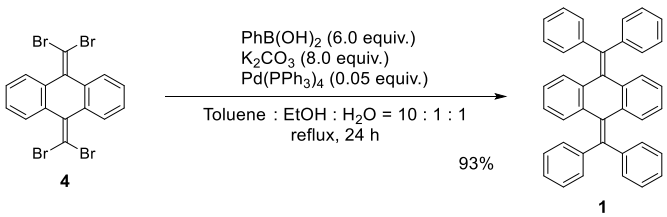

4 1

A mixture of 11,11,12,12-tetrabromo-9,10-anthraquinodimethane **4** (130 mg, 250 μmol), phenylboronic acid (183 mg, 1.50 mmol), K_2CO_3 (277 mg, 2.00 mmol) and $Pd(PPh_3)_4$ (14.5 mg, 12.5 μmol) in a mixture of toluene (3 mL), EtOH (0.3 mL) and water (0.3 mL) was stirred at 120 ℃ for 24 h. After cooling to 25 ℃, the reaction mixture was extracted with EtOAc three times. The combined

organic layers were washed with water and brine, and dried over anhydrous $MgSO_4$. After filtration, the solvent was concentrated under reduced pressure. The crude product was purified by column chromatography on silica gel (hexane/EtOAc = 30) to give **1** (118 mg) as an orange solid in 93% yield.
^{1}H NMR data were identical to those in literature.[66]

1,4,5,8-Tetraaza-9,10-anthraquinone (11)

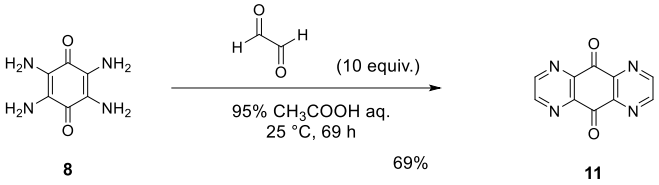

A mixture of 2,3,5,6-tetraamino-1,4-benzoquinone **8** (1.01 g, 6.00 mmol) and glyoxal (40% in water, 13.7 mL, 120 mmol) in 95% CH_3COOH aq. (210 mL) was stirred at 25 ℃ for 69 h. After stirring, the precipitates were collected by filtration and washed with water. The residue was redissolved in EtOH (50 mL) and stirred at 80 ℃ for 1 h, and the solution was filtered to give a **11** (882 mg) as a gray solid in 69% yield.
^{1}H NMR data were identical to those in literature.[67]

11,11,12,12-Tetrabromo-1,4,5,8-tetraaza-9,10-anthraquinodimethane (12)

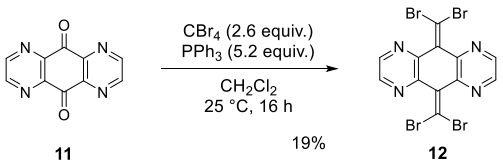

A mixture of CBr_4 (4.07 g, 12.3 mmol) and PPh_3 (6.44 g, 24.6 mmol) in dry CH_2Cl_2 (50 mL) was stirred at 25 ℃ for 1 h, and then 1,4,5,8-tetraaza-9,10-anthraquinone **11** (1.00 g, 4.72 mmol) was added to the mixture at 0 ℃. After warming to 25 ℃, the mixture was stirred at 25 ℃ for 16 h. After diluting with water, the precipitates were filtered and washed with $CHCl_3$. The resulting filtrate was extracted with $CHCl_3$ three times. The combined organic layers were washed with water and brine, and dried over anhydrous $MgSO_4$. After filtration, the solvent was concentrated under reduced pressure. The crude product was purified by column chromatography on silica gel (hexane/EtOAc/$CHCl_3$ = 4/1/4) to give **12** (467 mg) as a white solid in 19% yield.
^{1}H NMR data were identical to those in literature.[68]

11,11,12,12-Tetraphenyl-1,4,5,8-tetraaza-9,10-anthraquinodimethane (6)

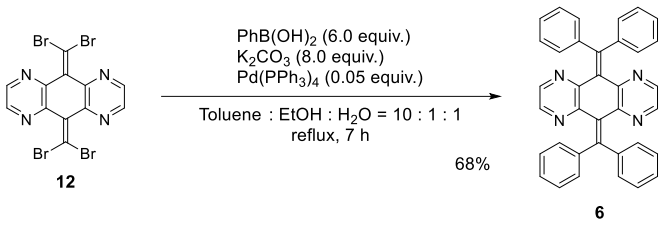

A mixture of 11,11,12,12-tetrabromo-1,4,5,8-tetraaza-9,10-anthraquinodimethane **12** (81.4 mg, 155 μmol), phenylboronic acid (114 mg, 933 μmol), K_2CO_3 (172 mg, 1.24 mmol) and $Pd(PPh_3)_4$ (9.1 mg, 7.9 μmol) in a mixture of toluene (3 mL), EtOH (0.3 mL) and water (0.3 mL) was stirred at 120 ℃ for 7 h. After cooling to 24 ℃, the reaction mixture was extracted with CH_2Cl_2 three times. The combined organic layers were washed with water and brine, and dried over anhydrous $MgSO_4$. After filtration, the solvent was concentrated under reduced pressure. The crude product was purified by column chromatography on silica gel (hexane/EtOAc = 3) to give **6** (54.3 mg) as an orange solid in 68% yield.
^{1}H NMR data were identical to those in literature.[68]

2,3,6,7-Tetraphenyl-9,10-anthraquinone (14)

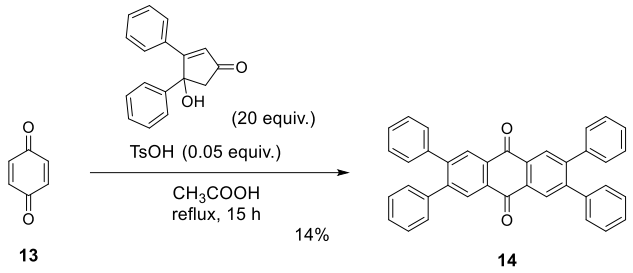

A mixture of 1,4-benzoquinone **13** (216 mg, 2.00 mmol), 4-hydroxy-3,4-diphenylcyclopent-2-en-1-one (1.00 g, 4.00 mmol) and *p*-toluenesulfonic acid monohydrate (19.0 mg, 100 μmol) in CH_3COOH (55 mL) was stirred at reflux for 15 h. After cooling to 26 ℃, the mixture was diluted with water and extracted with CH_2Cl_2 three times. The combined organic layers were washed with water, saturated $NaHCO_3$ aq. and brine, and dried over anhydrous $MgSO_4$. After filtration, the solvent was concentrated under reduced pressure. The crude product was purified by column chromatography on silica gel (hexane/CH_2Cl_2 = 1) to give **14** (143 mg) as a yellow powder in 14% yield.
^{1}H NMR data were identical to those in literature.[69]

11,11,12,12-Tetrabromo-2,3,6,7-tetraphenyl -9,10-anthraquinodimethane (15)

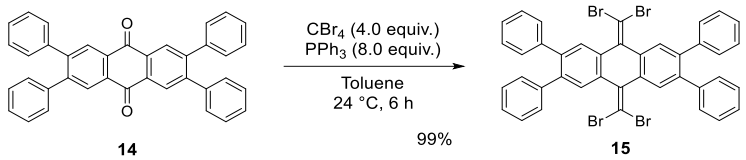

A mixture of CBr_4 (265 mg, 799 μmol) and PPh_3 (412 mg, 1.60 mmol) in dry toluene (2 mL) was stirred at 24 ℃ for 1 h. To the suspension was added 2,3,6,7-tetraphenyl-9,10-anthraquinone **14** (102 mg, 200 μmol), and the mixture was heated at reflux for 6 h. After cooling to 24 ℃, the reaction mixture was diluted with water, and extracted with CH_2Cl_2 three times. The combined organic layers were washed with water and brine, and dried over anhydrous $MgSO_4$. After filtration, the solvent was concentrated under reduced pressure. The crude product was purified by column chromatography on silica gel (hexane/CH_2Cl_2 = 1) to give **15** (164 mg) as a white powder in 99% yield.

Mp: >400 ℃; ^{1}H NMR (400 MHz, $CDCl_3$): δ/ppm 7.96 (4H, s), 7.25-7.18 (12H, m), 7.17-7.09 (8H, m); ^{13}C NMR (100 MHz, $CDCl_3$): δ/ppm 140.57, 139.43, 138.75, 134.90, 129.85, 129.81, 128.05, 126.94, 90.67; IR (ATR): ν/cm^{-1} 3077, 3050, 3021, 2959, 2926, 2862, 1726, 1600, 1576, 1539, 1494, 1467, 1381, 1279, 1262, 1182, 1122, 1074, 1026, 1000, 960, 909, 783, 769, 746, 697, 650, 622, 614, 585, 564, 536, 521, 503; LR-MS(FD) *m*/*z* (%): 827.76 (24), 826.77 (32), 824.77 (44), 823.76 (bp), 822.77 (30), 821.77 (66), 819.77 (M^+, 17); HR-MS (FD) Calcd. for $C_{40}H_{24}Br_4$: 819.86115; Found: 819.86086.

2,3,6,7,11,11,12,12-Octaphenyl-9,10-anthraquinodimethane (7)

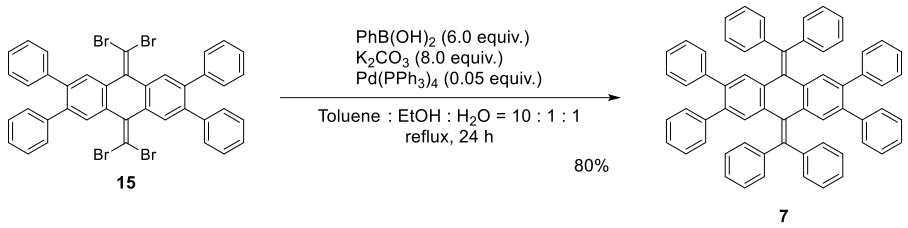

A mixture of 11,11,12,12-tetrabromo-2,3,6,7-tetraphenyl-9,10-anthraquinodimethane **15** (124 mg, 150 μmol), phenylboronic acid (110 mg, 901 μmol), K_2CO_3 (166 mg, 1.20 mmol) and $Pd(PPh_3)_4$ (8.70 mg, 7.50 μmol) in a mixture of toluene (3 mL), EtOH (0.3 mL) and water (0.3 mL) was stirred at 120 ℃ for 24 h. After cooling to 25 ℃, the reaction mixture was extracted with EtOAc three times. The combined organic layers were washed with water and brine, and dried over anhydrous $MgSO_4$. After filtration, the solvent was concentrated under reduced pressure. The crude product was purified by column chromatography on silica gel (hexane/EtOAc = 20) to give **7** (98.0 mg) as a pale-yellow powder in 80% yield.

Mp: 297.6-298.9 ℃; ^{1}H NMR (400 MHz, $CDCl_3$): δ/ppm 7.47 (8H, dd, J = 1.3, 7.4 Hz), 7.30 (8H, t, J = 7.4 Hz), 7.20 (4H, tt, J = 1.3, 7.4 Hz), 7.10-6.99 (12H, m), 7.07 (4H, s), 6.65 (8H, dd, J = 1.4,

7.3 Hz); ^{13}C NMR (100 MHz, $CDCl_3$): δ/ppm 142.51, 141.17, 140.58, 137.56, 136.61, 134.63, 130.41, 129.77, 129.66, 128.33, 127.39, 126.72, 126.05; IR (ATR): ν/cm^{-1} 3077, 3055, 3020, 1599, 1576, 1490, 1472, 1464, 1442, 1383, 1243, 1179, 1155, 1073, 1030, 1001, 980, 964, 925, 917, 905, 777, 769, 754, 747, 719, 697, 644, 624, 616, 596, 576, 537, 506, 475; LR-MS(FD) *m*/*z* (%): 814.32 (27), 813.31 (73), 812.31 (M^+, bp), 406.66 (11), 406.16 (M^{2+}, 16); HR-MS (FD) Calcd. for $C_{64}H_{44}$: 812.34430; Found: 812.34621.

2-4-3. X-ray analyses

Method

A suitable crystal was selected and measured on a Rigaku XtaLAB Synergy (Cu-Kα radiation, λ = 1.54184 Å) with HyPix diffractometer. The crystal was kept at 150 K during data collection. Using Olex2,[70] the structure was solved with the SHELXT[71] structure solution program using Intrinsic Phasing and refined with the SHELXL[72] refinement package using Least Squares minimization.

Table 2-9. Crystal data of **6**, **7**, and **2a**.

	6	**7**	**(a) F-form**	**(b) F-form**	**(c) T-form**
Recrystallization solvent	$CHCl_3$/hexane	CH_2Cl_2/hexane	CH_2Cl_2/hexane	$CHCl_3$/EtOH	CH_2Cl_2/EtOH
Color and shape	Yellow block	Colorless plate	Yellow plate	Yellow plate	Red block
Solvate	Non	Non	CH_2Cl_2	$CHCl_3$	None
Empirical formula	$C_{36}H_{24}N_4$	$C_{64}H_{44}$	$C_{61}H_{42}N_4Cl_2$	$C_{61}H_{41}N_4Cl_3$	$C_{60}H_{40}N_4$
Formula weight	512.59	812.99	901.88	936.33	816.96
Temperature/K	150	150	150	150	150
Crystal system	triclinic	triclinic	monoclinic	monoclinic	triclinic
Space group	P-1	P-1	$P2_1/n$	$P2_1/n$	P-1
a [Å]	9.93699(14)	10.81378(14)	16.5930(3)	16.58736(14)	9.75804(18)
b [Å]	13.4375(2)	19.7207(2)	16.7981(3)	17.18100(13)	10.24335(19)
c [Å]	20.7105(3)	32.0682(4)	17.4925(3)	17.25022(14)	12.5631(2)
α [°]	100.7714(13)	87.3043(10)	90	90	109.5893(17)
β [°]	95.4569(12)	80.5761(11)	100.4761(18)	101.0383(8)	92.4238(15)
γ [°]	102.2024(12)	88.2988(10)	90	90	114.6339(18)
Volume [$Å^3$]	2629.12(7)	6737.26(15)	4794.45(16)	4825.14(7)	1050.81(4)
Z	4	6	4	4	1
ρ_{calc}g [cm^3]	1.295	1.202	1.249	1.289	1.291
μ [mm^{-1}]	0.6	0.515	1.559	2.066	0.582
Crystal size [mm^3]	0.2 × 0.15 × 0.1	0.3 × 0.1 × 0.05	0.2 × 0.1 × 0.05	0.6 × 0.5 × 0.05	0.4 × 0.2 × 0.2
Reflections collected	31474	85233	31137	31612	11871
Independent reflections	10588	27336	9524	9741	4276
R_{int}	0.0339	0.0332	0.0708	0.0311	0.0251
Data/restraints/parameters	10588/0/721	27336/0/1729	9524/0/604	9741/0/613	4276/0/289
GOF	1.035	1.032	1.158	1.54	1.034
R1 [I>=2σ (I)]	0.0613	0.0645	0.1134	0.0961	0.0436
wR2 [I>=2σ (I)]	0.1668	0.1753	0.2821	0.3134	0.1136
R1 [all data]	0.0664	0.0702	0.1534	0.1003	0.0458
wR2 [all data]	0.1720	0.1806	0.3074	0.3248	0.1155
CCDC	2176740	2176741	2176742	2176743	2176744

Table 2-10. Crystal data of **2b**.

	(a) F-form	(b) P-form	(c) P-form	(d) P-form	(e) TF-form	(f) TF-form	(g) TF-form	(h) TF-form	(i) T-form
Recrystallization solvent	EtOAc/EtOH	EtOAc/EtOH	CH_2Cl_2/hexane	$CHCl_3$/EtOH	CH_2Cl_2/hexane	EtOAc/hexane	EtOAc/EtOH	CH_2Cl_2/EtOH	EtOAc/hexane
Color and shape	Yellow plate	Orange plate	Orange plate	Orange plate	Reddish-orange plate	Reddish-orange block	Reddish-orange plate	Reddish-orange plate	Red plate
Solvate	2EtOH	H_2O	CH_2Cl_2	0.5$CHCl_3$	0.5CH_2Cl_2	0.5hexane	0.5EtOAc	CH_2Cl_2	None
Empirical formula	$C_{68}H_{60}N_4O_2$	$C_{64}H_{50}N_4O$	$C_{65}H_{50}N_4Cl_2$	$C_{64.5}H_{48.5}N_4Cl_{1.5}$	$C_{64.5}H_{49}ClN_4$	$C_{67}H_{55}N_4$	$C_{66}H_{52}N_4O$	$C_{65}H_{50}Cl_2N_4$	$C_{64}H_{48}N_4$
Formula weight	965.2	891.08	957.99	932.75	915.52	916.15	917.11	957.99	873.06
Temperature/K	150	150	150	150	150	150	150	150	150
Crystal system	monoclinic	monoclinic	monoclinic	monoclinic	triclinic	triclinic	triclinic	triclinic	monoclinic
Space group	$P2_1/n$	$P2_1/n$	$P2_1/n$	$P2_1/n$	P-1	P-1	P-1	P-1	I2/a
a [Å]	13.73810(16)	13.0186(7)	13.06055(8)	13.15327(10)	13.8714(3)	13.8366(2)	13.83784(18)	13.8559(4)	28.1936(3)
b [Å]	19.2903(2)	15.5503(6)	15.93664(9)	15.80594(9)	14.3596(3)	14.3012(2)	14.3149(3)	14.3395(3)	5.66772(5)
c [Å]	20.7162(3)	25.0921(8)	24.82470(16)	25.12301(16)	15.5180(4)	15.4141(3)	15.3314(2)	15.2345(3)	32.3675(3)
α [°]	90	90	90	90	87.623(2)	73.7712(15)	73.8179(14)	73.943(2)	90
β [°]	105.0871(12)	103.288(4)	102.6521(6)	102.2740(7)	70.622(2)	71.2750(16)	71.4192(12)	71.145(2)	107.8392(11)
γ [°]	90	90	90	90	61.366(2)	61.2700(17)	61.3275(16)	61.450(3)	90
Volume [Å^3]	5300.81(11)	4943.7(4)	5041.58(5)	5103.68(6)	2533.36(11)	2504.14(9)	2496.59(8)	2488.83(13)	4923.45(9)
Z	4	4	4	4	2	2	2	2	4
ρ_{calc}g [cm^3]	1.209	1.197	1.262	1.214	1.2	1.215	1.22	1.278	1.178
μ [mm^{-1}]	0.562	0.549	1.511	1.245	1.008	0.539	0.558	1.531	0.526
Crystal size [mm^3]	0.5 × 0.1 × 0.02	0.2 × 0.05 × 0.02	0.5 × 0.2 × 0.03	0.4 × 0.2 × 0.05	0.8 × 0.4 × 0.1	0.4 × 0.2 × 0.15	0.3 × 0.2 × 0.03	0.6 × 0.2 × 0.03	0.6 × 0.1 × 0.05
Reflections collected	35360	35436	34101	34613	30266	28717	29691	30911	17160
Independent reflections	10752	10077	10179	10384	10267	10106	10091	10236	4926
R_{int}	0.0378	0.1381	0.0262	0.0189	0.0512	0.0330	0.0203	0.0416	0.0218
Data/restraints/parameters	10752/0/675	10077/0/625	10179/0/653	10384/0/653	10267/0/662	10106/0/645	10091/0/657	10236/0/645	4926/0/309
GOF	1.016	1.023	1.045	1.065	1.038	1.044	1.034	1.034	1.069
R1 [I>=2σ (I)]	0.0487,	0.0888,	0.0516,	0.0725	0.0880	0.0480	0.0479	0.0718	0.0446
wR2 [I>=2σ (I)]	0.1270	0.2273	0.1413	0.2231	0.2615	0.1283	0.1367	0.2030	0.1160
R1 [all data]	0.0596	0.1802	0.0549	0.0755	0.0931	0.0514	0.0507	0.0770	0.0463
wR2 [all data]	0.1343	0.2836	0.1443	0.2264	0.2679	0.1315	0.1397	0.2083	0.1175
CCDC	2176745	2176746	2176747	2176748	2176749	2176750	2176751	2176752	2176753

Table 2-11. Crystal data of **2c**.

	(a) F-form	(b) F-form	(c) F-form	(d) F-form	(e) F-form + semi-P-form	(f) TP-form	(g) TP-form	(h) TP-form	(i) TF-form
Recrystallization solvent	EtOAc	CH_2Cl_2/hexane	CH_2Cl_2/EtOH	$CHCl_3$/EtOH	$CHCl_3$/hexane	$CHCl_3$/hexane	CH_2Cl_2/hexane	EtOAc/EtOH	$CHCl_3$/hexane
Color and shape	Yellow block	Yellow plate	Yellow plate	Yellow plate	Orange plate	Red needle	Red needle	Red needle	Reddish-orange plate
Solvate	EtOAc	$0.25CH_2Cl_2$	$1.25CH_2Cl_2$	$2CHCl_3$	H_2O	$CHCl_3$	CH_2Cl_2	EtOH	$CHCl_3$
Empirical formula	$C_{64}H_{44}N_4O_2F_4$	$C_{60.25}H_{36.5}Cl_{0.5}F_4N_4$	$C_{61.25}H_{38.5}Cl_{2.5}F_4N_4$	$C_{62}H_{38}Cl_6F_4N_4$	$C_{60}H_{38}F_4N_4O$	$C_{61}H_{37}Cl_3F_4N_4$	$C_{61}H_{38}Cl_2F_4N_4$	$C_{62}H_{42}F_4N_4O$	$C_{61}H_{37}N_4F_4Cl_3$
Formula weight	977.03	910.16	995.08	1127.66	906.94	1008.29	973.85	934.99	1008.29
Temperature/K	150	150	150	150	150	150	150	150	150
Crystal system	monoclinic	monoclinic	monoclinic	monoclinic	triclinic	monoclinic	monoclinic	monoclinic	triclinic
Space group	$P2_1/n$	$P2_1/n$	$P2_1/n$	$P2_1/n$	P-1	C2/c	$P2_1/n$	$P2_1/n$	P-1
a [Å]	12.75083(13)	12.66222(15)	12.7522(3)	12.86604(12)	13.3387(4)	25.6556(5)	25.5002(17)	25.5161(2)	10.12009(13)
b [Å]	22.3845(2)	21.9556(3)	22.7801(8)	24.1764(2)	16.6099(5)	9.8373(2)	9.7673(4)	9.80781(8)	13.5095(2)
c [Å]	17.88186(15)	17.6375(2)	17.1545(6)	17.28731(17)	18.4931(6)	40.0763(7)	40.489(4)	39.5463(4)	18.6161(3)
α [°]	90	90	90	90	108.333(3)	90	90	90	102.7568(13)
β [°]	98.8812(9)	99.1661(11)	97.596(3)	99.5946(9)	94.699(2)	96.4440(18)	95.796(7)	94.5123(9)	97.5345(12)
γ [°]	90	90	90	90	105.688(3)	90	90	90	91.2272(12)
Volume [Å^3]	5042.66(8)	4840.72(11)	4939.6(3)	5302.07(9)	3681.3(2)	10050.6(3)	10032.9(12)	9866.08(15)	2457.54(6)
Z	4	4	4	4	3	8	8	8	2
ρ_{calc}g [cm^3]	1.287	1.249	1.338	1.413	1.227	1.333	1.289	1.259	1.363
μ [mm^{-1}]	0.72	0.929	1.929	3.449	0.685	2.142	1.648	0.696	2.19
Crystal size [mm^3]	0.4 × 0.4 × 0.2	1.0 × 0.7 × 0.1	0.4 × 0.2 × 0.1	0.3 × 0.2 × 0.05	0.3 × 0.1 × 0.02	0.4 × 0.04 × 0.03	0.7 × 0.02 × 0.02	0.8 × 0.05 × 0.03	0.5 × 0.25 × 0.1
Reflections collected	32543	29221	30617	32287	41870	30470	62192	61118	29396
Independent reflections	10208	9726	9950	10723	14790	9912	20204	19771	9922
R_{int}	0.0228	0.0659	0.0303	0.0304	0.0299	0.0341	0.1222	0.0282	0.0360
Data/restraints/parameters	10208/0/657	9726/0/623	9950/0/666	10723/0/685	14790/0/932	9912/0/692	20204/0/1334	19771/0/1279	9922/0/649
GOF	1.04	1.075	1.086	1.013	1.036	1.036	1.088	1.044	1.064
R1 [I>=2σ (I)]	0.0670	0.0756	0.1064	0.1052	0.0527	0.0914	0.1267	0.0796	0.0854
wR2 [I>=2σ (I)]	0.1951	0.2183	0.2531	0.3110	0.1451	0.2775	0.3382	0.2347	0.2582
R1 [all data]	0.0700	0.0817	0.1123	0.1109	0.0609	0.1044	0.2382	0.0998	0.0898
wR2 [all data]	0.1979	0.2248	0.2561	0.3170	0.1508	0.2920	0.4033	0.2561	0.2632
CCDC	2176754	2176755	2176756	2176757	2176758	2176759	2176760	2176761	2176762

Table 2-12. Crystal data of **2d**.

	(a) P-form	(b) P-form	(c) TF-form	(d) T-form
Recrystallization solvent	$CHCl_3$/EtOH	CH_2Cl_2/hexane	$CHCl_3$/hexane	$CHCl_3$/hexane
Color and shape	Orange plate	Orange plate	Reddish-orange plate	Red needle
Solvate	$CHCl_3$	CH_2Cl_2	$CHCl_3$	None
Empirical formula	$C_{61}H_{37}N_4Cl_7$	$C_{61}H_{38}N_4Cl_6$	$C_{61}H_{37}Cl_7N_4$	$C_{60}H_{36}N_4Cl_4$
Formula weight	1074.09	1039.65	1074.09	954.73
Temperature/K	150	150	150	150
Crystal system	triclinic	monoclinic	triclinic	orthorhombic
Space group	P-1	$P2_1/n$	P-1	$P2_12_12$
a [Å]	13.2185(5)	13.13701(8)	13.8192(2)	17.5899(5)
b [Å]	15.7122(5)	15.53185(9)	14.2692(2)	24.5607(6)
c [Å]	25.1598(8)	25.04601(14)	15.4824(2)	5.46102(14)
α [°]	91.884(3)	90	74.8558(14)	90
β [°]	101.524(3)	102.7632(6)	70.7523(14)	90
γ [°]	93.318(3)	90	61.4238(16)	90
Volume [Å^3]	5106.3(3)	4984.17(5)	2511.37(8)	2359.26(11)
Z	4	4	2	2
ρ_{calc}g [cm^3]	1.397	1.385	1.42	1.344
μ [mm^{-1}]	3.907	3.502	3.972	2.634
Crystal size [mm^3]	0.15 × 0.15 × 0.01	0.4 × 0.2 × 0.1	0.15 × 0.15 × 0.05	0.5 × 0.05 × 0.05
Reflections collected	56442	30493	30619	8107
Independent reflections	20217	10068	10148	4279
R_{int}	0.0875	0.0210	0.0420	0.0299
Data/restraints/parameters	20217/0/1297	10068/0/640	10148/0/649	4279/0/307
GOF	1.019	1.024	1.056	1.074
R1 [I>=2σ (I)]	0.1065	0.0396	0.0952	0.0440
wR2 [I>=2σ (I)]	0.2955	0.0994	0.2723	0.1195
R1 [all data]	0.1454	0.0415	0.1061	0.0482
wR2 [all data]	0.3320	0.1008	0.2849	0.1219
CCDC	2176763	2176764	2176765	2176766

Chapter 3.

Efficient Synthesis of Tetraazaquinodimethane Analogues for On-Surface Chemistry

3-1. Introduction

Graphene is a monatomic sheet of carbon atoms tightly and covalently bonded to each other in a honeycomb structure. Its physical properties are fascinating and have been the subject of research on a global scale, including its extremely attractive physical properties and excellent electrical conductivity.[73,74] On the other hand, graphene with some carbon atoms replaced by nitrogen is called nitrogen N-doped (nano)graphene (Figure 3-1). Although N-doped (nano)graphene is expected to have catalytic properties in chemical reactions, e.g., increasing catalytic ability due to the coordination of a metal and nitrogen atom or acting as a catalyst itself, no clear synthetic method has been established, and its chemical properties remain unknown.

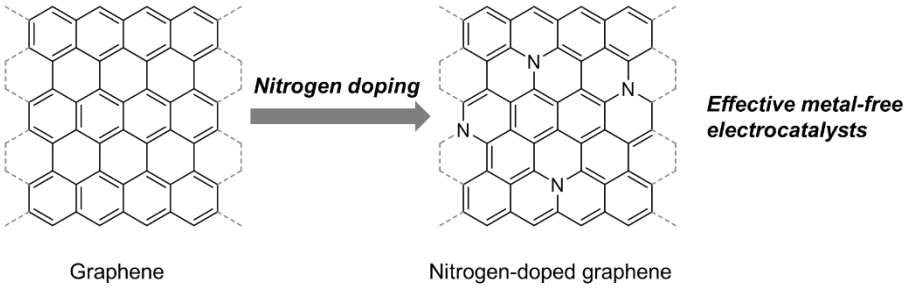

Figure 3-1. Nitrogen-doped graphene.

In addition, many studies on conversions and linking reactions of small molecules by catalytic properties of atoms on a metal surface have been conducted extensively in recent years. In contrast to wet chemistry such as a batch reaction in a flask, surface reactions do not pose solubility problems, making them a representative strategy for synthesizing extended π-conjugated molecules such as graphene nanoribbons.[75–77] Furthermore, the flattening of compounds upon adsorption on metal substrates allows for the synthesis of unique molecules that are rarely obtained in solution.[78]

To gain new insights into the construction of N-doped nanographene, the author focused on the N_4AQD analogues, which was the target compounds in Chapter 2. The author envisaged that the flexible structure of N_4AQDs, which can adopt not only non-planar forms (**F**-form or **T**-form) but also planar form, would be suitable for deposition on a metal substrate, and further on-surface reactions would occur by annealing at higher temperature. Since the formation of covalent C-N bonds through a surface catalyzed thermal reaction has been reported (Scheme 3-1),[79] it is highly likely that a similar reaction with N_4AQDs can proceed to form an extended N-doped nanographene. On the other hand, as a strategy for synthesizing π-conjugated polymers using surface reactions, high-temperature

annealing of derivatives with dibromomethylene moieties on Au(111) has been used to obtain one-dimensional polymers by dehalogenation followed by homocoupling reaction.[80] Especially for bianthraquinodimethane derivatives, the further reaction proceeded to form ladder polymers by annealing (Scheme 3-2).[81] In view of this, it is of significant importance to systematically study how the tetrabromo precursor of the N_4AQD derivative behaves under similar conditions.

Scheme 3-1. Covalent C–N bond formation through a surface catalyzed thermal cyclodehydrogenation.

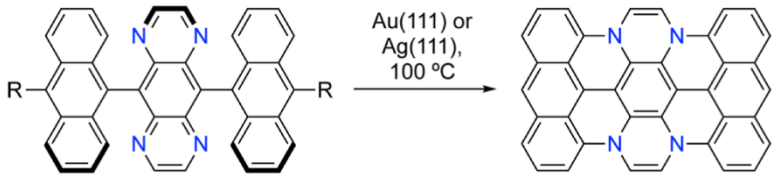

Scheme 3-2. On-surface synthesis of pentalene-bridged (a) anthene and (b) bisanthene polymers.

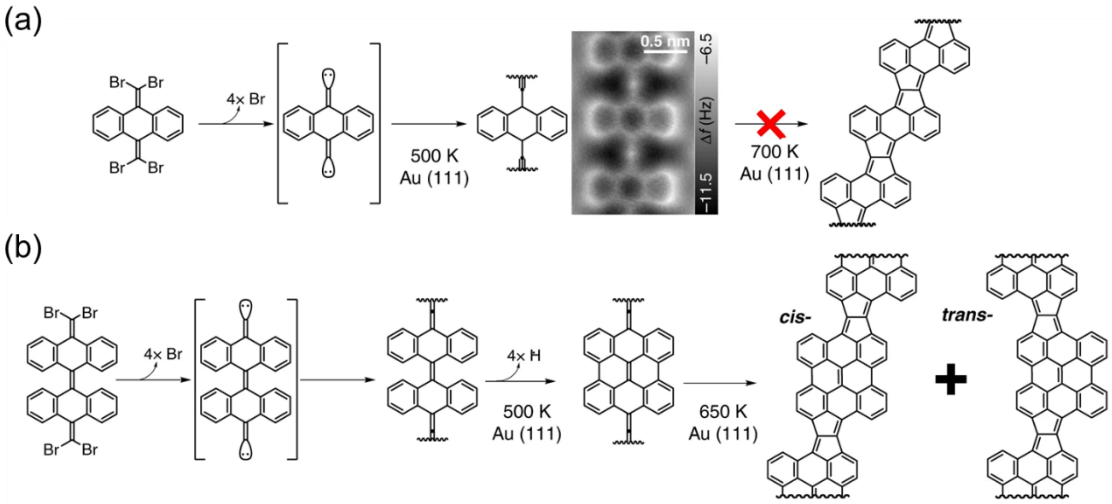

In this chapter, the author describes the efficient synthetic method of the formation of the tettraazaquinodimethane skeleton, i.e., the author has clarified the appropriate conditions under which the desired tetraazanthraquinone can be synthesized in high yield by the dehydrative condensation of 2,3,5,6-tetraamino-1,4-benzoquinone with any α-diketone. These anthraquinone derivatives can be used for dibromo-olefination and subsequent Suzuki-Miyaura cross-coupling reaction to construct tetraazaquinodimethane derivatives with desired substituents at the 2,3,6,7-positions on the central N_4AQD skeleton. On the other hand, collaborative research with Prof. Kawai, in Research Center for Advanced Measurement and Characterization National Institute for Materials Science (NIMS), demonstrated that on-surface reactions using the obtained derivatives were also successfully carried out.

3-2. Results and Discussions

3-2-1. Synthetic Procedure

To construct tetraazanthraquinone derivatives, the author considered the dehydrative condensation of 2,3,5,6-tetraamino-1,4-benzoquinone **8** with corresponding α-diketone as a simple and versatile way (Scheme 3-3). This method can be used as introducing arbitrary substituents at the 2,3,6,7-positions on the tetraazanthraquinone skeleton by changing the substituent R of α-diketone.

Scheme 3-3. Retrosynthetic analysis of 1,4,5,8-tetraaza-9,10-anthraquinone derivatives.

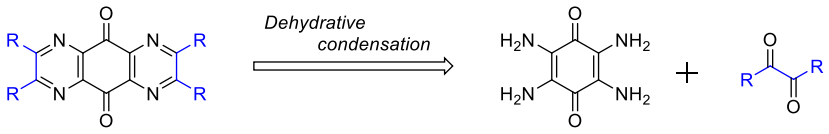

The reaction condition is the addition of an excess amount of α-diketone to **8**. Solvent optimization was performed by changing the mixing ratio of H_2O to CH_3COOH, with H_2O : CH_3COOH = 1 : 20 selected as the optimal condition. Using this reaction condition, **11**, **9**, **16**, and **17** were synthesized as the parent compound, the aryl substituted compound, the alkyl substituted compounds, and the longer substituted compounds, respectively (Scheme 3-4, **11** and **9** synthesized by this procedure were actually used in the study in Chapter 2). All the reactions proceeded in good yields; the condensation with benzil afforded **9** in 94% yields as a yellow powder, with glyoxal gave **11** in 69% as a gray solid, and with decane-5,6-dione and octadecane-9,10-dione led to **16** and **17** in 83% and 96% yields as a yellow powder and a yellow oil, respectively. Several synthetic studies on **11** have been reported, but they require heating or complicated purification processes, resulting in low yields (about 48%).[67,82] In addition, alkyl substituted derivatives have been only reported up to ethyl derivative (68%), even the long chain ones.[83] On the other hand, with the author's way, the reaction can be carried out under mild conditions at room temperature, and the purification can be achieved with simpler operations for all derivatives with even longer alkyl chains in high yields.

Scheme 3-4. Preparation of tetraazaanthraquinone derivatives **9**, **11**, **16**, and **17**.

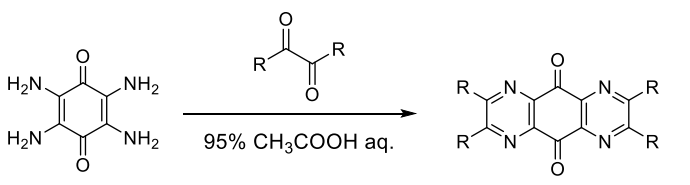

8

9 (R = C_6H_5) : 94%
11 (R = H) : 69%
16 (R = *n*-C_4H_9) : 83%
17 (R = *n*-C_8H_{17}) : 96%

Hereafter, the author reports on the application of the derivatives obtained by dibromo-olefination or/and subsequent Suzuki-Miyaura cross-coupling reactions on these anthraquinone derivatives to on-surface chemistry.

3-2-2. Molecular Design

In collaboration with Prof Kawai and his co-workers at NIMS, the author decided to trace the on-surface reactions of four tetraaza derivatives on Au(111) using a scanning tunneling microscope (STM). In order to investigate the effect of substituents on the central skeleton, 2,3,6,7,11,11,12,12-octaphenyl-1,4,5,8-tetraazanthraquinodimethane **2** was explored, compared with **6**. Then, 3-biphenyl derivative **18** and 2-naphthyl derivative **19** were also investigated how the difference of substituents on the diarylmethylene units (Figure 3-2).

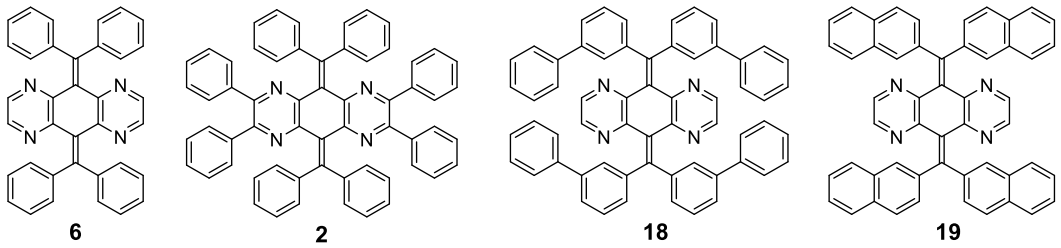

Figure 3-2. Target compounds for the on-surface reaction on Au(111).

As shown in Scheme 3-5, the formation of C-N bond between the central pyrazine ring and the phenyl group on the diarylmethylene unit is expected to form further extended N-doped nanographene, especially in derivative **2**.

Scheme 3-5. Expected on-surface reaction in which the formation of C-N and C-C bonds.

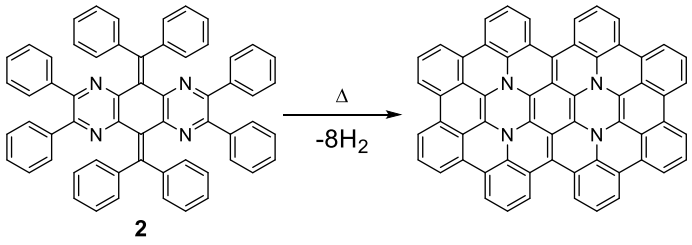

3-2-3. Heterocyclic Segregation

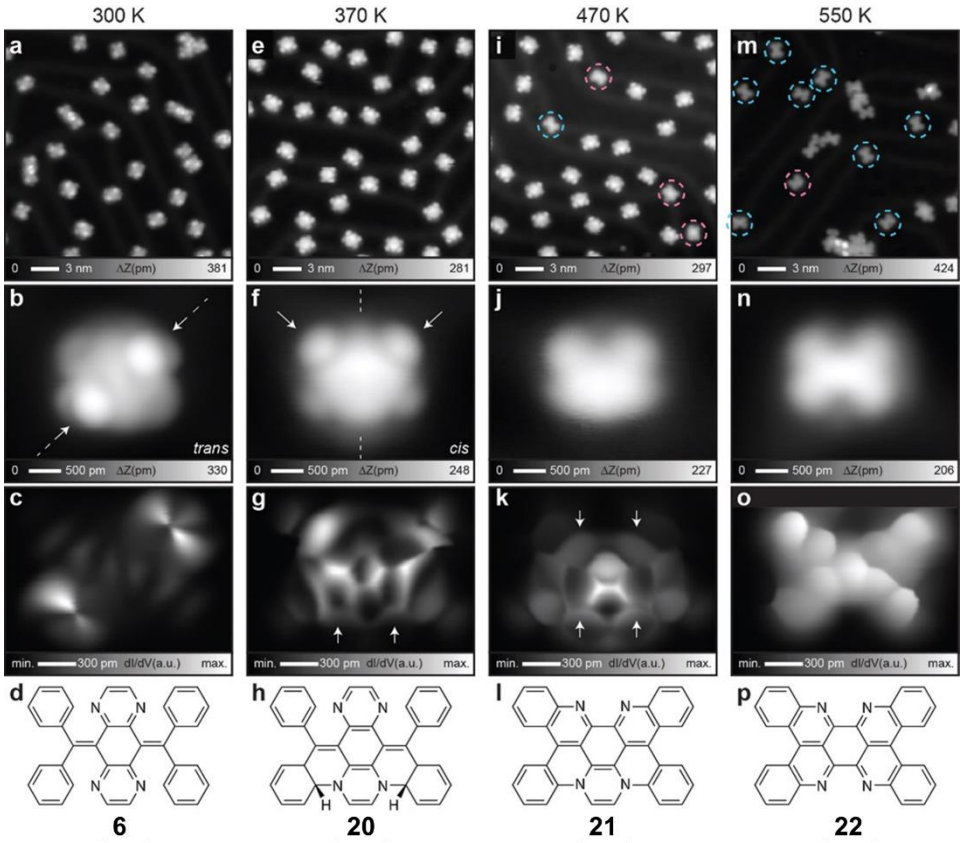

Figure 3-3. On-surface reaction of 11,11,12,12-tetraphenyl-1,4,5,8-tetraazaanthraquinodimethane **6** on Au(111). (a) STM topography of as-deposited **6**. (b) Close-up view of single molecule. (c) Constant height d*I*/d*V* map and (d) the corresponding chemical structure. (e) Large-scale STM topography of the surface after annealing at 370 K for 10 min. (f) Close-up view of single intermediate molecule. (g) Constant height d*I*/d*V* map and (h) the corresponding chemical structure. (i) Large-scale STM topography of the surface after annealing at 470 K for 10 min. (j) Close-up view of single intermediate molecule. (k) Constant height d*I*/d*V* map and (l) the corresponding chemical structure. (m) Large-scale STM topography of the surface after annealing at 550 K for 10 min. (n) Close-up view of the final product. (o) Constant height d*I*/d*V* map and (p) the corresponding chemical structure. Measurement parameters: Sample bias voltage $V = 200$ mV and tunneling current $I = 3$ pA in (a). $V = 900$ mV and $I = 100$ pA in (b). $V = 200$ mV and $I = 2$ pA in (e), (f), (j) and (n). $V = 200$ mV and $I = 5$ pA in (i). $V = 100$ mV and $I = 10$ pA in (m).

First of all, **6** was thermally deposited on a clean Au(111) surface kept at 300 K under ultra-high vacuum condition (Figure 3-3a). After annealing the sample at 370 K for 10 min, the changes in the molecular structure were observed from the STM images (Figure 3-3e). As a result of the investigation

of the structure in detail, C-N bonds between pyrazine and phenyl groups as indicated by arrows were formed, and the extra two hydrogen atoms still remained in the molecule due to the low-temperature annealing at 370 K (Figures 3-3g, h). This C-N bond formation is in agreement with the recent study with a similar molecule.[79] Higher temperature annealing induced planarization of the molecules as indicated by red and blue circles in Figure 3-3i. The ratio of each molecule was changed by the annealing temperature. Figure 3-3j shows the close-view of the molecule indicated by a red circle, which more frequently appeared at a lower annealing temperature of 470 K. The d*I*/d*V* map reveals that all nitrogen atoms in pyrazine groups conjugated to the carbon atoms in the adjacent phenyl groups, forming C_5N-six-membered rings as indicated by arrows in Figure 3-3k. Furthermore, the C-N bonds in the pyrazine group at the upper side were cleaved, which results in the ring opening (Figure 3-3l). This cleavage of the C-N bond became significant after higher temperature annealing at 550 K (Figure 3-3m). The molecule has two dips at both sides in the STM topography (dumbbell-like shape, Figure 3-3n), thus, both the pyrazine groups were thermally cleaved (Figure 1p). The statistical analysis indicates a strong temperature-dependence of the reaction yields of **22** as 1% (468 events) at 470 K, 13% (461 events) at 520 K, and 42% (559 events) at 550 K (Figure 3-4).

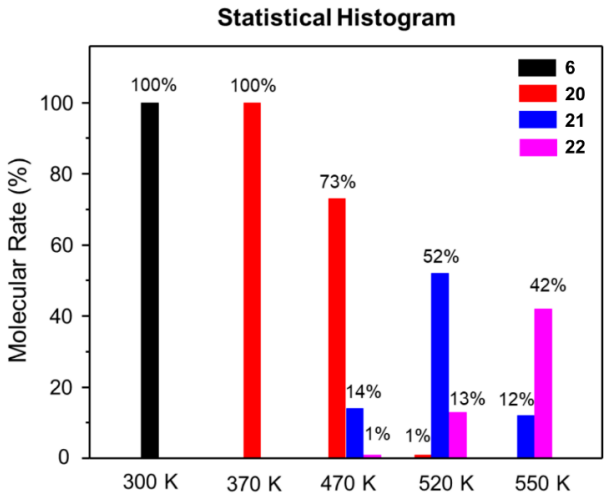

Figure 3-4. Statistical analysis for the transformation from compound **6** to compound **22** at different temperatures.

In order to clarify the generality of the heterocyclic segregation reaction, **2**, **18**, and **19** were similarly annealed to investigate the effect of substituents on the central backbone and on the diarylmethylene unit. In the case of octaphenyl derivative **2**, the creation of **22** was observed as in the case of **6**, which indicated that the reaction proceeds without being affected by the substituents on the central skeleton (Scheme 3-6a). On the other hand, **18** and **19** were also able to be transformed to a tetraphenyl-substituted derivative **23** and a tetrabenzo-fused derivative **24** of **22** under the same reaction condition (Scheme 3-6b).

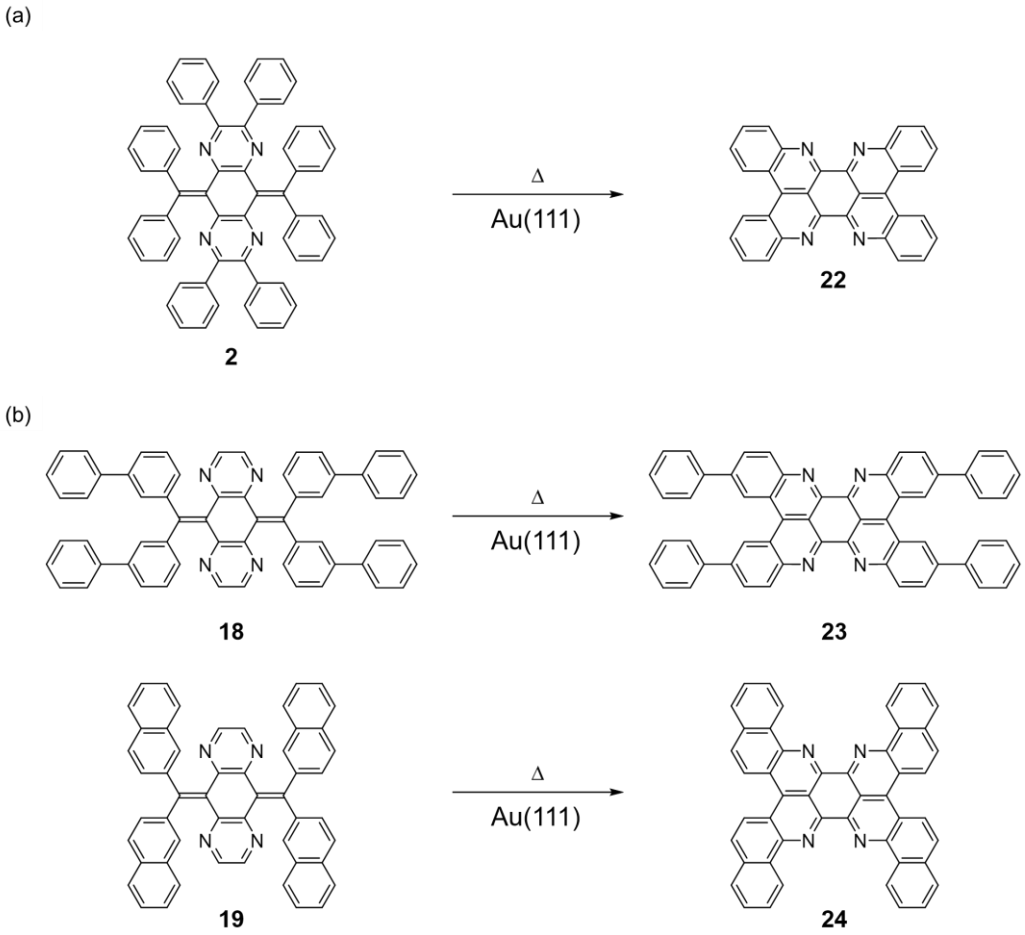

Scheme 6. Heterocyclic segregations of **2**, **18**, and **19** on Au(111).

3-2-4. Mechanism of Heterocyclic Segregation

This transformation is quite unique in the sense that two nitrogen atoms in one aromatic ring are divided into two azaaromatic units, e.g., 2,3-distyrylpyrazine into 2,2'-biquinoline (Scheme 3-7). Such a process of "heterocyclic segregation" is unprecedented and has not been observed in structurally-related compound studied by Fischer,[79] which only exhibits fusing heterocycles by cyclodehydrogenation.

Scheme 3-7. "Heterocyclic segregation" of 2,3-distyrylpyrazine to form 2,2'-biquinoline.

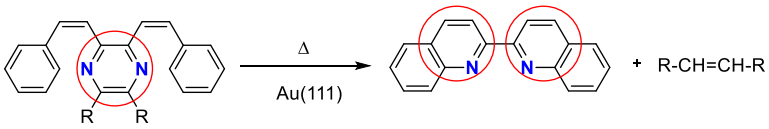

To clarify the mechanism of this unique reaction, DFT calculations were performed in collaboration with Prof. Taketsugu and his co-worker at Hokkaido University. The reaction mechanism was deduced with reference to the compounds observed at each temperature. As a result, the calculations demonstrate that there are two possible reaction pathways for transformation of **6** on Au(111) to the half-reacted intermediate **HR**: the path via H transfer to the Au(111) surface with the formation of the intermediate **INT1a** (path A) and the path via intramolecular H transfer with the formation of the intermediate **INT1b** (path B) as shown in Scheme 3-8 and Figure 3-5. In both pathways, via the common intermediate **INT2**, the ethylene molecule is endothermally eliminated from the **INT2** to form the half-reacted intermediate **HR**. By repeating this sequence on the other side, **6** is converted to **22** (Scheme 3-8).

Scheme 3-8. Mechanism of "heterocyclic segregation" of **6** on Au(111) to form **22**.

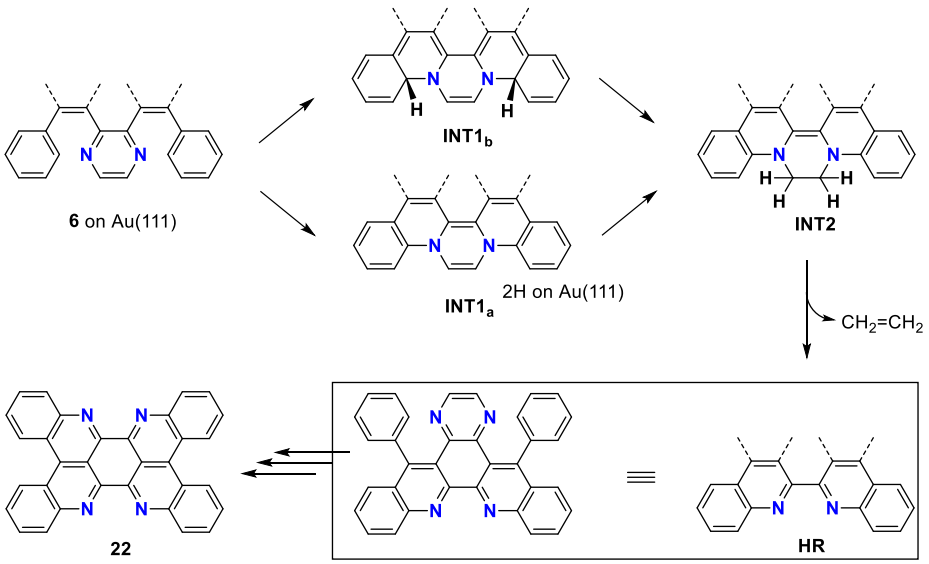

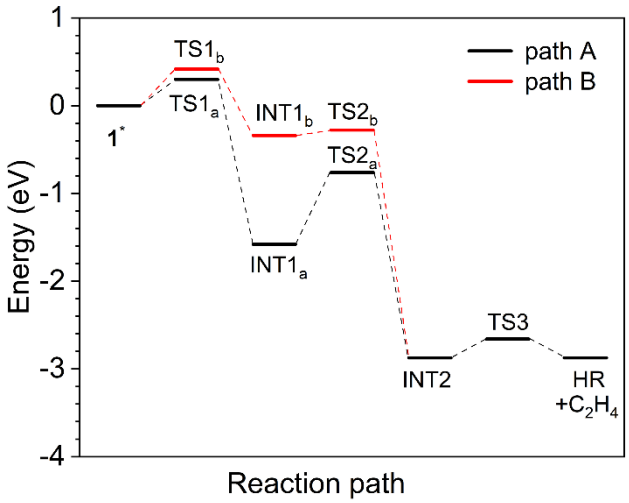

Figure 3-5. Free energy diagram for the transformation of **6** on Au(111) denoted as **6*** to the half-reacted intermediate **HR** and a free C_2H_4 molecule. Path A—transformation via H transfer via Au(111) surface; path B—transformation via intramolecular H transfer. Calculations are performed at T = 638 K, accounting for the entropy of a free C_2H_4 molecule.

3-3. Conclusion

In summary, the author provided the efficient method for the synthesis of tetraazaanthraquinone derivatives, in which any substituents can be introduced into the central skeleton, and these quinone can be used as a precursor to synthesize corresponding tetrabromo and tetraaryl N_4AQD derivatives. In addition, on-surface studies with these quinodimethane derivatives have led to the construction of novel N-doped aromatic hydrocarbons and the evaluation of unprecedented heterocyclic segregation reaction. These findings can promote a deep understanding to the C-N chemistry and may pave the way for the on-surface synthesis of various azaacene-based functional materials with two-dimensional expanded structure.

3-4. Experimental Section

3-4-1. General

STM Measurements. All the experiments were conducted with home-made scanning tunneling microscopy (STM) system, operating at 4.3 K under an ultra-high vacuum environment. Clean Au(111) substrates were prepared by cyclic Ar^+ sputtering for 10 min and annealing at 760 K for 10 min. 11,11,12,12-tetraphenyl-1,4,5,8-tetraazaanthraquinodimethane and its derivative molecules were deposited on clean Au(111) surfaces kept at 300 K. For bond-resolved STM imaging, the apex of the chemically-etched tungsten tip was terminated with a CO molecule by picking up from the surface. The DC sample bias voltage was set close to zero voltage. The modulation amplitude was 7 mV_{rms} and the frequency was 510 Hz.

Theoretical Calculations.

DFT calculations were performed using the Perdew–Burke-Ernzerhof (PBE) exchange-correlation functional[84] coupled with the DFT-D3 dispersion correction method[85] and the projector-augmented wave (PAW) method as implemented in the Vienna Ab initio Simulation Package (VASP).[86] A plane-wave basis set with an energy cutoff of 500 eV was used. All calculations are spin-polarized. The Au fcc lattice was optimized using the Monkhorst-Pack $18 \times 18 \times 18$ k-point mesh for Brillouin zone sampling. The calculated Au lattice parameter, a = 4.099 Å, is in good agreement with its experimental value of 4.08 Å.[87] The optimized lattice of bulk Au was used to construct a four-layer 9×9 slab of Au(111) surface with the lattice parameters of a = 26.0909 Å. The periodically replicated slabs were separated by a vacuum region of ~18 Å. Only the Γ point was used for sampling the Brillouin zone in the case of surface calculations due to the large size of the supercell. The trial structures of **1** with the different orientations and positions have been optimized on Au(111) surface where Au atoms in the bottom two layers of the slab were fixed while the adsorbed species, as well as Au atoms in the two outermost layers of the slab, were fully relaxed until forces were less than 0.01 eV $Å^{-1}$. The nudged elastic band (NEB)[88,89] and the climbing image nudged elastic band (CI-NEB)[90] methods have been used to obtain the transition states. To account the change of entropy along the reaction pathway we make a simple assumption that translational and rotational degrees of freedom give the main contribution to the total entropy of the free or pseudo-free molecules, while these degrees of freedom are frozen for the adsorbed species.

Chemical Synthesis.

All reactions were carried out under an argon atmosphere. All commercially available compounds were used without further purification unless otherwise indicated. Dry toluene was obtained by

distillation from CaH_2 prior to use. Column chromatography was performed on silica gel 60N (KANTO KAGAKU, spherical neutral) of particle size 40-50 μm or Wakogel® 60N (neutral) of particle size 38-100 μm. ^{1}H and ^{13}C NMR spectra were recorded on a BRUKER Ascend^{TM} 400 (^{1}H/400 MHz and ^{13}C/100 MHz) spectrometer. IR spectra were measured on a Shimadzu IRAffinity-1S spectrophotometer using the attenuated total reflection (ATR) mode, and as a KBr pellet on a JEOL JIR-WINSPEC100 FT/IR spectrophotometer. Mass spectra were recorded on a JMS-T100GCV spectrometer in FD mode by Dr. Eri Fukushi and Mr. Yusuke Takata (GC-MS & NMR Laboratory, Research Faculty of Agriculture, Hokkaido University). Melting points were measured on a Stanford Research Systems OptiMelt MPA100 and are uncorrected.

3-4-2. Preparation

2,3,6,7-Tetrabutyl-1,4,5,8-tetraaza-9,10-anthraquinone (16)

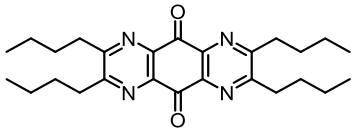

16

A mixture of 2,3,5,6-tetraamino-1,4-benzoquinone **8**[55] (151 mg, 900 μmol) and decane-5,6-dione[91] (1.53 g, 9.00 mmol) in 95% CH_3COOH aq. (32 mL) was stirred at 26 ℃ for 16 h. To the mixture was added 5 M NaOH aq. at 0 ℃ to until pH was adjusted to 4~5, and the whole mixture was extracted with CH_2Cl_2 three times. The combined organic layers were washed with water and brine, and dried over anhydrous $MgSO_4$. After filtration, the solvent was concentrated under reduced pressure. The crude product was purified by column chromatography on silica gel (hexane/EtOAc = 3) to give **16** (327 mg) as a brownish yellow powder in 83% yield.

Mp: 70.0-72.0 ℃; ^{1}H NMR (400 MHz, $CDCl_3$): δ/ppm 3.11 (8H, t, J = 8.0 Hz), 1.87-1.75 (8H, m), 1.50 (8H, sext, J = 7.4 Hz), 0.99 (12H, t, J = 7.4 Hz); ^{13}C NMR (100 MHz, $CDCl_3$): δ/ppm 180.23, 162.65, 142.13, 35.08, 30.99, 22.84, 13.87; IR (ATR): ν/cm^{-1} 2958, 2931, 2868, 1702, 1534, 1460, 1405, 1375, 1333, 1316, 1281, 1233, 1177, 1103, 1064, 1032, 962, 927, 886, 790, 748, 732, 664, 621, 507; LR-MS(FD) m/z (%): 437.23 (36), 436.23 (M^+, bp); HR-MS (FD) Calcd. for $C_{26}H_{36}N_4O_2$: 436.28383; Found: 436.28484.

2,3,6,7-Tetraoctyl-1,4,5,8-tetraaza-9,10-anthraquinone (17)

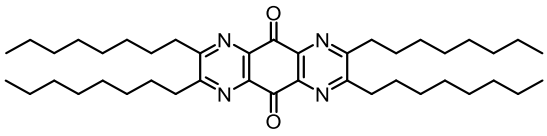

17

A mixture of 2,3,5,6-tetraamino-1,4-benzoquinone **8**[55] (100 mg, 595 μmol) and octadecane-9,10-dione[92] (840 mg, 2.97 mmol) in 95% CH_3COOH aq. (21 mL) was stirred at 24 ℃ for 16 h. To the mixture was added 5 M NaOH aq. at 0 ℃ to until pH was adjusted to 4~5, and the whole mixture was extracted with CH_2Cl_2 three times. The combined organic layers were washed with water and brine, and dried over anhydrous $MgSO_4$. After filtration, the solvent was concentrated under reduced pressure. The crude product was purified by column chromatography on silica gel (hexane/EtOAc = 5) to give **17** (377 mg) as a brownish yellow oil in 96% yield.

^{1}H NMR (400 MHz, $CDCl_3$): δ/ppm 3.10 (8H, t, J = 8.0 Hz), 1.87-1.76 (8H, m), 1.52-1.20 (40H, m), 0.88 (12H, t, J = 6.9 Hz); ^{13}C NMR (100 MHz, $CDCl_3$): δ/ppm 180.22, 162.68, 142.13, 35.38, 31.83, 29.72, 29.38, 29.20, 29.00, 22.66, 14.09; IR (ATR): ν/cm^{-1} 2955, 2921, 2871, 2853, 1700, 1539,

1465, 1457, 1378, 1326, 1238, 1217, 1177, 1166, 1116, 1053, 1034, 910, 727, 668, 627; LR-MS(FD) *m*/*z* (%): 663.50 (12), 662.49 (42), 661.49 (bp), 660.48 (M^+, 99), 659.47 (13), 658.47 (14); HR-MS (FD) Calcd. for $C_{42}H_{68}N_4O_2$: 660.53423; Found: 660.53562.

11,11,12,12-Tetrakis(biphenyl-3-yl)-1,4,5,8-tetraaza-9,10-anthraquinodimethane (18)

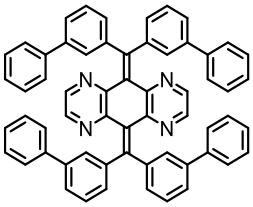

18

A mixture of 11,11,12,12-tetrabromo-1,4,5,8,-tetraaza-9,10-anthraquinodimethane **8**[55] (192 mg, 367 μmol), 2,4,6-tris(biphenyl-3-yl)boroxine (396 mg, 734 μmol), K_2CO_3 (406 mg, 2.93 mmol) and $Pd(PPh_3)_4$ (21.2 mg, 18.3 μmol) in a mixture of toluene (10 mL), EtOH (1.0 mL) and water (1.0 mL) was stirred at 120 °C for 21 h. After cooling to 26 °C, the reaction mixture was extracted with CH_2Cl_2 three times. The combined organic layers were washed with water and brine, and dried over anhydrous $MgSO_4$. After filtration, the solvent was concentrated under reduced pressure. The crude product was purified by column chromatography on silica gel (hexane/EtOAc = 3) to give **18** (55.8 mg) as a white solid in 19% yield.

Mp: 210-220 °C (decomp); ^{1}H NMR (400 MHz, $CDCl_3$): δ/ppm 8.07 (4H, s), 7.65 (4H, t, *J* = 1.4 Hz), 7.48 (4H, dt, *J* = 1.6, 7.0 Hz), 7.43 (8H, dt, *J* = 1.6, 7.0 Hz), 7.34 (8H, dt, *J* = 1.6, 7.0 Hz), 7.31-7.25 (12H. m); ^{13}C NMR (100 MHz, $CDCl_3$): δ/ppm 151.26, 149.30, 141.69, 141.29, 140.90, 140.12, 130.94, 129.70, 129.31, 128.77, 129.08, 127.25, 127.01, 126.29; IR (KBr): *ν*/cm^{-1} 3056, 3031, 2360, 2337, 1946, 1886, 1807, 1738, 1595, 1571, 1526, 1501, 1476, 1450, 1408, 1368, 1357, 1236, 1150, 1108, 1090, 1076, 1031, 1002, 917, 890, 861, 839, 801, 760, 741, 730, 717, 697, 663, 643, 615, 603, 554, 506, 452; LR-MS(FD) *m*/*z* (%): 819.42 (5), 818.41 (24), 817.41 (71), 816.41 (M^+, bp), 408.71 (10), 408.20 (M^{2+}, 14); HR-MS (FD) Calcd. for $C_{60}H_{40}N_4$: 816.32530; Found: 816.32499.

11,11,12,12-Tetrakis(2-naphthyl)-1,4,5,8-tetraaza-9,10-anthraquinodimethane (19)

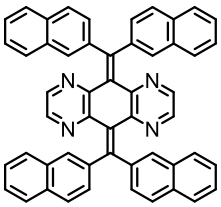

19

A mixture of 11,11,12,12-tetrabromo-1,4,5,8,-tetraaza-9,10-anthraquinodimethane **8**[55] (177 mg,

339 μmol), 2,4,6-tris(2-naphthyl)boroxine (313 mg, 677 μmol), K_2CO_3 (374 mg, 2.71 mmol) and $Pd(PPh_3)_4$ (19.8 mg, 17.1 μmol) in a mixture of toluene (10 mL), EtOH (1.0 mL) and water (1.0 mL) was stirred at 120 °C for 37 h. After cooling to 25 °C, the reaction mixture was extracted with CH_2Cl_2 three times. The combined organic layers were washed with water and brine, and dried over anhydrous $MgSO_4$. After filtration, the solvent was concentrated under reduced pressure. The crude product was purified by column chromatography on silica gel (hexane/EtOAc/$CHCl_3$ = 9/2/6) to give **19** (109 mg) as a yellow powder in 45% yield.

Mp: 250 °C; ^{1}H NMR (400 MHz, $CDCl_3$): δ/ppm 7.93 (4H, brs), 7.90 (4H, s), 7.84-7.75 (8H, m), 7.74 (4H, d, J = 8.3 Hz), 7.52 (4H, dd, J = 1.7, 8.3 Hz), 7.50-7.43 (8H, m); ^{13}C NMR (100 MHz, $CDCl_3$): δ/ppm 151.19, 149.15, 141.26, 139.20, 132.80, 132.70, 131.18, 130.29, 128.83, 128.38, 127.63, 126.84, 126.30, 126.07; IR (KBr): ν/cm^{-1} 3054, 2965, 2921, 2861, 2365, 2294, 1916, 1809, 1626, 1597, 1525, 1501, 1463, 1448, 1433, 1386, 1351, 1305, 1274, 1248, 1193, 1155, 1144, 1129, 1110, 1090, 1066, 1018, 954, 902, 861, 819, 777, 751, 727, 698, 655, 649, 625, 595, 575, 559, 538, 515, 476, 451; LR-MS(FD) m/z (%): 714.35 (20), 713.35 (62), 712.34 (M^+, bp), 357.17 (5), 356.67 (15), 356.17 (M^{2+}, 25); Anal. Calcd. (%) for $C_{52}H_{32}N_4$・water: C 85.46, H 4.69, N 7.67; found: C 85.71, H 4.42, N 7.61.

References

[1] H. M. D. Bandara, S. C. Burdette, *Chem. Soc. Rev.* **2012**, *41*, 1809–1825.

[2] R. Klajn, *Chem. Soc. Rev.* **2014**, *43*, 148–184.

[3] M. Irie, T. Fukaminato, K. Matsuda, S. Kobatake, *Chem. Rev.* **2014**, *114*, 12174–12277.

[4] Y. Ishigaki, K. Sugawara, T. Tadokoro, Y. Hayashi, T. Harimoto, T. Suzuki, *Chem. Commun.* **2021**, *57*, 7201–7214.

[5] S. Kassem, T. Van Leeuwen, A. S. Lubbe, M. R. Wilson, B. L. Feringa, D. A. Leigh, *Chem. Soc. Rev.* **2017**, *46*, 2592–2621.

[6] Y. Sakata, S. Fukushima, S. Akine, J. I. Setsune, *Chem. Commun.* **2016**, *52*, 1278–1281.

[7] P. Lentes, E. Stadler, F. Röhricht, A. Brahms, J. Gröbner, F. D. Sönnichsen, G. Gescheidt, R. Herges, *J. Am. Chem. Soc.* **2019**, *141*, 13592–13600.

[8] L. Bai, P. Bose, Q. Gao, Y. Li, R. Ganguly, Y. Zhao, *J. Am. Chem. Soc.* **2017**, *139*, 436–441.

[9] Y.-Y. Tang, Y.-L. Zeng, R.-G. Xiong, *J. Am. Chem. Soc.* **2022**, *144*, 8633–8640.

[10] M. Raisch, D. Genovese, N. Zaccheroni, S. B. Schmidt, M. L. Focarete, M. Sommer, C. Gualandi, *Adv. Mater.* **2018**, *30*, DOI 10.1002/adma.201802813.

[11] W. Li, Q. Huang, Z. Mao, J. Zhao, H. Wu, J. Chen, Z. Yang, Y. Li, Z. Yang, Y. Zhang, M. P. Aldred, Z. Chi, *Angew. Chem. Int. Ed.* **2020**, *59*, 3739–3745.

[12] T. Suzuki, H. Tamaoki, J. I. Nishida, H. Higuchi, T. Iwai, Y. Ishigaki, K. Hanada, R. Katoono, H. Kawai, K. Fujiwara, T. Fukushima, *Org. Redox Syst. Synth. Prop. Appl.* **2015**, 13–37.

[13] E. Ohta, H. Uehara, Y. Han, K. Wada, H. Noguchi, R. Katoono, Y. Ishigaki, H. Ikeda, K. Uosaki, T. Suzuki, *Chempluschem* **2017**, *82*, 1043–1047.

[14] Y. Ishigaki, Y. Hayashi, T. Suzuki, *J. Am. Chem. Soc.* **2019**, *141*, 18293–18300.

[15] Y. Ishigaki, T. Harimoto, K. Sugawara, T. Suzuki, *J. Am. Chem. Soc.* **2021**, *143*, 3306–3311.

[16] S. Iwashita, E. Ohta, H. Higuchi, H. Kawai, K. Fujiwara, K. Ono, **2004**, 2076–2077.

[17] T. Suzuki, Y. Sakano, T. Iwai, S. Iwashita, Y. Miura, R. Katoono, H. Kawai, K. Fujiwara, Y. Tsuji, T. Fukushima, *Chem. - A Eur. J.* **2013**, *19*, 117–123.

[18] R. J. Mortimer, *Annu. Rev. Mater. Res* **2011**, *41*, 241–68.

[19] D. A. Davis, A. Hamilton, J. Yang, L. D. Cremar, D. Van Gough, S. L. Potisek, M. T. Ong, P. V. Braun, T. J. Martínez, S. R. White, J. S. Moore, N. R. Sottos, *Nature* **2009**, *459*, 68–72.

[20] Y. Matsuo, Y. Wang, H. Ueno, T. Nakagawa, H. Okada, *Angew. Chem. Int. Ed.* **2019**, *58*, 8762–8767.

[21] M. Tanioka, S. Kamino, A. Muranaka, Y. Ooyama, H. Ota, Y. Shirasaki, J. Horigome, M. Ueda, M. Uchiyama, D. Sawada, S. Enomoto, *J. Am. Chem. Soc.* **2015**, *137*, 6436–6439.

[22] H. Ito, T. Saito, N. Oshima, N. Kitamura, S. Ishizaka, Y. Hinatsu, **2008**, *2*, 10044–10045.

[23] Y. Hong, J. W. Y. Lam, B. Z. Tang, *Chem. Soc. Rev.* **2011**, *40*, 5361–5388.

[24] Q. Qi, J. Zhang, B. Xu, B. Li, S. X. A. Zhang, W. Tian, *J. Phys. Chem. C* **2013**, *117*, 24997–25003.

[25] T. Machida, R. Taniguchi, T. Oura, K. Sada, K. Kokado, *Chem. Commun.* **2017**, *53*, 2378–2381.

[26] J. Luo, K. Song, F. L. Gu, Q. Miao, *Chem. Sci.* **2011**, *2*, 2029–2034.

[27] Y. Ishigaki, T. Hashimoto, K. Sugawara, S. Suzuki, T. Suzuki, *Angew. Chem. Int. Ed.* **2020**, *59*, 6581–6584.

[28] Y. Adachi, T. Nomura, S. Tazuhara, H. Naito, J. Ohshita, *Chem. Commun.* **2021**, *57*, 1316–1319.

[29] N. Koumura, R. W. J. Zijlstra, R. A. Van Delden, **1999**, *401*, 1997–2000.

[30] B. L. Feringa, *Acc. Chem. Res.* **2001**, *34*, 504–513.

[31] T. Kudernac, N. Ruangsupapichat, M. Parschau, B. MacIá, N. Katsonis, S. R. Harutyunyan, K. H. Ernst, B. L. Feringa, *Nature* **2011**, *479*, 208–211.

[32] M. Baroncini, S. Silvi, A. Credi, *Chem. Rev.* **2020**, *120*, 200–268.

[33] H. Meyer, *Erste Mitteilung fiber Zweikernchinone* **1908**, *126*, 165–177.

[34] P. U. Biedermann, J. J. Stezowski, I. Agranat, *ChemInform* **2010**, *33*, no-no.

[35] W. R. Browne, M. M. Pollard, B. De Lange, A. Meetsma, B. L. Feringa, *J. Am. Chem. Soc.* **2006**, *128*, 12412–12413.

[36] T. Suzuki, H. Okada, T. Nakagawa, K. Komatsu, C. Fujimoto, H. Kagi, Y. Matsuo, *Chem. Sci.* **2018**, *9*, 475–482.

[37] Y. Hirao, Y. Hamamoto, N. Nagamachi, T. Kubo, *Phys. Chem. Chem. Phys.* **2019**, *21*, 12209–12216.

[38] X. Yin, J. Z. Low, K. J. Fallon, D. W. Paley, L. M. Campos, *Chem. Sci.* **2019**, *10*, 10733–10739.

[39] T. Nishiuchi, S. Aibara, H. Sato, T. Kubo, *J. Am. Chem. Soc.* **2022**, *144*, 7479–7488.

[40] Y. Hirao, Y. Hamamoto, T. Kubo, *Chem. - An Asian J.* **2022**, *17*, DOI 10.1002/asia.202200121.

[41] H. Takezawa, T. Murase, M. Fujita, *J. Am. Chem. Soc.* **2012**, *134*, 17420–17423.

[42] Y. Wang, Y. Ma, K. Ogumi, B. Wang, T. Nakagawa, Y. Fu, Y. Matsuo, *Commun. Chem.* **2020**, *3*, 2–4.

[43] T. Suzuki, T. Fukushima, T. Miyashi, T. Tsuji, *Angew. Chemie Int. Ed. English* **1997**, *36*, 2495–2497.

[44] T. Suzuki, E. Ohta, H. Kawai, K. Fujiwara, T. Fukushima, *Synlett* **2007**, 851–869.

[45] Y. Ishigaki, Y. Hayashi, K. Sugawara, T. Shimajiri, W. Nojo, R. Katoono, T. Suzuki, *Molecules* **2017**, *22*, 2714.

[46] Y. Sakano, R. Katoono, K. Fujiwara, T. Suzuki, *Chem. Lett.* **2014**, *43*, 1143–1145.

[47] R. Neidlein, M. Winter, *Synthesis (Stuttg).* **1998**, 1362–1366.

[48] F. Beaumard, P. Dauban, R. H. Dodd, *Synthesis (Stuttg).* **2010**, 4033–4042.

[49] V. Novakova, M. Miletin, K. Kopecky, P. Zimcik, *Chem. - A Eur. J.* **2011**, *17*, 14273–14282.

[50] T. Suzuki, Y. Ishigaki, T. Iwai, H. Kawai, K. Fujiwara, H. Ikeda, Y. Kano, K. Mizuno, *Chem. - A*

Eur. J. **2009**, *15*, 9434–9441.

[51] J. Paczkowski, Z. Kucybała, *Macromolecules* **1995**, *28*, 269–273.

[52] L. L. Miller, G. D. Nordblom, E. A. Mayeda, *J. Org. Chem.* **1972**, *37*, 916–918.

[53] Y. Ishigaki, K. Sugawara, M. Yoshida, M. Kato, T. Suzuki, *Bull. Chem. Soc. Jpn.* **2019**, *92*, 1211–1217.

[54] C. Hansch, A. Leo, R. W. Taft, *Chem. Rev.* **1991**, *91*, 165–195.

[55] R. Manivannan, S. Ciattini, L. Chelazzi, K. P. Elango, *RSC Adv.* **2015**, *5*, 87341–87351.

[56] T. Suzuki, Y. Ishigaki, K. Sugawara, Y. Umezawa, R. Katoono, A. Shimoyama, Y. Manabe, K. Fukase, T. Fukushima, *Tetrahedron* **2018**, *74*, 2239–2244.

[57] X. Gu, J. Yao, G. Zhang, Y. Yan, C. Zhang, Q. Peng, Q. Liao, Y. Wu, Z. Xu, Y. Zhao, H. Fu, D. Zhang, *Adv. Funct. Mater.* **2012**, *22*, 4862–4872.

[58] T. Nishiuchi, S. Aibara, T. Yamakado, R. Kimura, S. Saito, H. Sato, T. Kubo, *Chem. - A Eur. J.* **2022**, *28*, e202200286.

[59] Y. Chandrasekaran, G. K. Dutta, R. B. Kanth, S. Patil, *Dye. Pigment.* **2009**, *83*, 162–167.

[60] Q. Li, C. Yan, J. Zhang, Z. Guo, W. H. Zhu, *Dye. Pigment.* **2019**, *162*, 802–807.

[61] T. Mutai, H. Shono, Y. Shigemitsu, K. Araki, *CrystEngComm* **2014**, *16*, 3890–3895.

[62] D. Kitagawa, T. Nakahama, K. Mutoh, Y. Kobayashi, J. Abe, H. Sotome, S. Ito, H. Miyasaka, S. Kobatake, *Dye. Pigment.* **2017**, *139*, 233–238.

[63] K. Zheng, F. Ni, Z. Chen, C. Zhong, C. Yang, *Angew. Chem. Int. Ed.* **2020**, *59*, 9972–9976.

[64] M. J. Frisch, G. W. Trucks, H. B. Schlegel, G. E. Scuseria, M. A. Robb, J. R. Cheeseman, G. Scalmani, V. Barone, G. A. Petersson, X. Nakatsuji, H.; Li, M. Caricato, A. V. Marenich, J. Bloino, B. G. Janesko, R. Gomperts, B. Mennucci, H. P. Hratchian, J. V. Ortiz, A. F. Izmaylov, J. L. Sonnenberg, D. Williams-Young, F. Ding, F. Lipparini, F. Egidi, J. Goings, B. Peng, A. Petrone, T. Henderson, D. Ranasinghe, V. G. Zakrzewski, J. Gao, N. Rega, G. Zheng, W. Liang, M. Hada, M. Ehara, K. Toyota, R. Fukuda, J. Hasegawa, M. Ishida, T. Nakajima, Y. Honda, O. Kitao, H. Nakai, T. Vreven, K. Throssell, J. A. J. Montgomery, J. E. Peralta, F. Ogliaro, M. J. Bearpark, J. J. Heyd, E. N. Brothers, K. N. Kudin, V. N. Staroverov, T. A. Keith, R. Kobayashi, J. Normand, K. Raghavachari, A. P. Rendell, J. C. Burant, S. S. Iyengar, J. Tomasi, M. Cossi, J. M. Millam, M. Klene, C. Adamo, R. Cammi, J. W. Ochterski, R. L. Martin, K. Morokuma, O. Farkas, J. B. Foresman, D. J. Fox, *Gaussian 16, Revision A.03*, Gaussian, Inc., Wallingford CT, **2016**.

[65] Y. Yamashita, T. Suzuki, G. Saito, T. Mukai, *Chem. Lett.* **1986**, *15*, 715–718.

[66] S. Pola, C. H. Kuo, W. T. Peng, M. M. Islam, I. Chao, Y. T. Tao, *Chem. Mater.* **2012**, *24*, 2566–2571.

[67] H. Yoo, M. Suh, S. W. Park, *J. Med. Chem.* **1998**, *41*, 4716–4722.

[68] K. Sun, K. Sugawara, A. Lyalin, Y. Ishigaki, K. Uosaki, T. Taketsugu, T. Suzuki, S. Kawai,

Angew. Chem. Int. Ed. **2021**, *60*, 9427–9432.

[69] D. Bailey, J. N. Murphy, V. E. Williams, *Can. J. Chem.* **2006**, *84*, 659–666.

[70] O. V. Dolomanov, L. J. Bourhis, R. J. Gildea, J. A. K. Howard, H. Puschmann, *J. Appl. Crystallogr.* **2009**, *42*, 339–341.

[71] G. M. Sheldrick, *Acta Crystallogr. Sect. A Found. Adv.* **2015**, *71*, 3–8.

[72] G. M. Sheldrick, *Acta Crystallogr. Sect. C Struct. Chem.* **2015**, *71*, 3–8.

[73] A. K. Geim, *Rev. Mod. Phys.* **2011**, *83*, 851–862.

[74] K. S. Novoselov, A. K. Geim, S. V. Morozov, D. Jiang, Y. Zhang, S. V. Dubonos, I. V. Grigorieva, A. A. Firsov, *Science (80-.).* **2004**, *306*, 666–669.

[75] L. Talirz, P. Ruffieux, R. Fasel, *Adv. Mater.* **2016**, *28*, 6222–6231.

[76] J. Cai, P. Ruffieux, R. Jaafar, M. Bieri, T. Braun, S. Blankenburg, M. Muoth, A. P. Seitsonen, M. Saleh, X. Feng, K. Müllen, R. Fasel, *Nature* **2010**, *466*, 470–473.

[77] P. Ruffieux, S. Wang, B. Yang, C. Sanchez-Sanchez, J. Liu, T. Dienel, L. Talirz, P. Shinde, C. A. Pignedoli, D. Passerone, T. Dumslaff, X. Feng, K. Müllen, R. Fasel, *Nature* **2016**, *531*, 489–492.

[78] K. Nakamura, Q. Q. Li, O. Krejčí, A. S. Foster, K. Sun, S. Kawai, S. Ito, *J. Am. Chem. Soc.* **2020**, *142*, 11363–11369.

[79] I. Piskun, R. Blackwell, J. Jornet-Somoza, F. Zhao, A. Rubio, S. G. Louie, F. R. Fischer, *J. Am. Chem. Soc.* **2020**, *142*, 3696–3700.

[80] A. Sánchez-Grande, B. de la Torre, J. Santos, B. Cirera, K. Lauwaet, T. Chutora, S. Edalatmanesh, P. Mutombo, J. Rosen, R. Zbořil, R. Miranda, J. Björk, P. Jelínek, N. Martín, D. Écija, *Angew. Chem. Int. Ed.* **2019**, *58*, 6559–6563.

[81] B. de la Torre, A. Matěj, A. Sánchez-Grande, B. Cirera, B. Mallada, E. Rodríguez-Sánchez, J. Santos, J. I. Mendieta-Moreno, S. Edalatmanesh, K. Lauwaet, M. Otyepka, M. Medveď, Á. Buendía, R. Miranda, N. Martín, P. Jelínek, D. Écija, *Nat. Commun.* **2020**, *11*, 1–8.

[82] H. Bock, P. Dickmann, H.-F. Herrmann, *Zeitschrift für Naturforsch. B* **1991**, *46*, 326–338.

[83] T. W. Morris, I. J. Huerfano, M. Wang, D. L. Wisman, A. C. Cabelof, N. U. Din, C. D. Tempas, D. Le, A. V. Polezhaev, T. S. Rahman, K. G. Caulton, S. L. Tait, *Chem. - A Eur. J.* **2019**, *25*, 5565–5573.

[84] J. P. Perdew, K. Burke, M. Ernzerhof, *Phys. Rev. Lett.* **1996**, *77*, 3865–3868.

[85] S. Grimme, J. Antony, S. Ehrlich, H. Krieg, *J. Chem. Phys.* **2010**, *132*, 154104.

[86] G. Kresse, J. Furthmüller, *Phys. Rev. B - Condens. Matter Mater. Phys.* **1996**, *54*, 11169–11186.

[87] R. W. G. Wyckoff, *Crystal Structures - Volume 1.*, John Wiley & Sons: New York, **1963**.

[88] G. Mills, H. Jónsson, G. K. Schenter, *Surf. Sci.* **1995**, *324*, 305–337.

[89] H. JÓNSSON, G. MILLS, K. W. JACOBSEN, in *Class. Quantum Dyn. Condens. Phase Simulations*, WORLD SCIENTIFIC, **1998**, pp. 385–404.

[90] G. Henkelman, B. P. Uberuaga, H. Jónsson, *J. Chem. Phys.* **2000**, *113*, 9901–9904.

[91] U. T. Mueller-Westerhoff, M. Zhou, *J. Org. Chem.* **1994**, *59*, 4988–4992.

[92] D. D. Kenning, K. A. Mitchell, T. R. Calhoun, M. R. Funfar, D. J. Sattler, S. C. Rasmussen, **2002**, 9073–9076.

Acknowledgements

This study described in this dissertation was carried out under the direction of Associate Professor Dr. Yusuke Ishigaki (Department of Chemistry, Faculty of Science, Hokkaido University). The author would like to express his sincere gratitude to Associate Professor Ishigaki for his consistent guidance, suggestion. valuable discussions, encouragement, and so much help throughout the course of this work. From the bottom of the author's heart, he is deeply glad Associate Professor Ishigaki was his supervision.

The author would like to express his deepest grateful to Professor Dr. Takanori Suzuki (Department of Chemistry, Faculty of Science, Hokkaido University) for his kind guidance, suggestion, valuable discussion, encouragement, and so much help throughout the course of this work. In particular, the author cannot thank Professor Suzuki enough for his tremendous help during the author's stay in Canada.

The author would like to be really thankful to Assistant Professor Dr. Takuya Shimajiri (Department of Chemistry, Faculty of Science, Hokkaido University) for his helpful guidance, suggestion, valuable discussion, encouragement, and so much help throughout the course of this work. The author has always had the goal and admiration for Assistant Professor Shimajiri.

The author deeply grateful to Assistant Professor Dr. Ryo Katoono (Department of Chemistry, Faculty of Science, Hokkaido University) for his helpful guidance, suggestion, encouragement and so much help throughout the course of this work.

The author would like to thank Professor Dr. Masaya Sawamura, Professor Dr. Aiichiro Nagaki, and Associate Professor Dr. Hisanori Senboku for their valuable suggestions and discussions.

The author expresses deeply grateful to Professor Dr. Masako Kato and Assistant Professor Dr. Masaki Yoshida (Department of Chemistry, Faculty of Science, Hokkaido University) for giving him the opportunity to make experiments for the contents of Chapter 1.

The author expresses sincere thanks to Associate Professor Dr. Toshikazu Ono and Dr. Yoshio Yano (Department of Chemistry and Biochemistry, Graduate School of Engineering, Kyusyu University) for giving him the opportunity to make experiments for the contents of Chapter 2.

The author expresses deeply grateful to Professor Dr. Shigeki Kawai (Research Center for Advanced Measurement and Characterization National Institute for Materials Science) and Professor Dr. Tetsuya Taketsugu (Department of Chemistry, Faculty of Science, Hokkaido University) for giving him the opportunity to make experiments for the contents of Chapter 3.

The author is really thankful to Dr. Eri Fukushi, and Mr. Yusuke Takada (GC-MS & NMR Laboratory, Graduate School of Agriculture, Hokkaido University) for the measurements of mass.

The author is deeply grateful to Professor Dr. Graham J. Bodwell and his laboratory members (Department of Chemistry, Memorial University of Newfoundland) for their heartfelt guidance, suggestion, valuable discussions, and so much encouragement during my stay in Canada.

The author gives special thanks to Dr. Wataru Nojo, Mr. Keisuke Sugimoto, Mr. Yuki Hayashi, Mr. Masataka Saito, and Mr. Hironori Aoki and other members in Suzuki Laboratory for their valuable discussion and giving his invaluable time.

The author is in acknowledgement of Research Fellowship of the Japan Society for the Promotion of Science (JSPS) for Young Scientists for Financial Support.

Finally, the author would like to express his deep and sincere gratitude to his parents, Toshihiko Sugawara and Chiaki Sugawara, for their continuous financial help and encouragement.

Kazuma Sugawara